UNIVERSIDADE ESTADUAL DE CAMPINAS
Instituto de Física "Gleb Wataghin"

RICARDO JAVIER PEÑA ROMAN

Morphological and optical characterization of the 2D materials WSe_2, WS_2 and h-BN.

Caracterização morfológica e óptica dos materiais 2D WSe_2, WS_2 e h-BN.

CAMPINAS
2018

RICARDO JAVIER PEÑA ROMAN

Morphological and optical characterization of the 2D materials WSe_2, WS_2 and h-BN.

Caracterização morfológica e óptica dos materiais 2D WSe_2, WS_2 e h-BN.

Dissertation presented to the Institute of Physics "Gleb Wataghin" of the University of Campinas in partial fulfillment of the requirements for the degree of Master, in the area of Applied Physics.

Dissertação apresentada ao Instituto de Física "Gleb Wataghin" da Universidade Estadual de Campinas como parte dos requisitos exigidos para a obtenção do título de Mestre em Física, na Área de Física Aplicada.

Advisor/Orientador: Prof. Dr. Luiz Fernando Zagonel

Este trabalho corresponde à versão final da dissertação defendida pelo aluno Ricardo Javier Peña Roman, e orientada pelo Prof. Dr. Luiz Fernando Zagonel.

CAMPINAS
2018

Agência(s) de fomento e nº(s) de processo(s): CNPq, 130022/2017-9; CAPES, 1642782/2016

Ficha catalográfica
Universidade Estadual de Campinas
Biblioteca do Instituto de Física Gleb Wataghin
Lucimeire de Oliveira Silva da Rocha - CRB 8/9174

P37m

Peña Roman, Ricardo Javier, 1990-
Morphological and optical characterization of the 2D materials WSe2, WS2 and h-BN / Ricardo Javier Peña Roman. – Campinas, SP : [s.n.], 2018.

Orientador: Luiz Fernando Zagonel.
Dissertação (mestrado) – Universidade Estadual de Campinas, Instituto de Física Gleb Wataghin.

1. Materiais bidimensionais. 2. Dicalcogenetos de metais de transição. 3. Nitreto de boro hexagonal. 4. Microscopia de tunelamento de elétrons. 5. Microscopia de força atômica. 6. Espectroscopia Raman. 7. Fotoluminescência. I. Zagonel, Luiz Fernando, 1979-. II. Universidade Estadual de Campinas. Instituto de Física Gleb Wataghin. III. Título.

Informações para Biblioteca Digital

Título em outro idioma: Caracterização morfológica e óptica dos materiais 2D WSe2, WS2 e h-BN
Palavras-chave em inglês:
Two-dimensional materials
Transition metal dichalcogenides
Hexagonal boron nitride
Scanning tunneling microscopy
Atomic force microscopy
Raman spectroscopy
Photoluminescence
Área de concentração: Física Aplicada
Titulação: Mestre em Física
Banca examinadora:
Luiz Fernando Zagonel [Orientador]
Roberto Magalhães Paniago
Pierre-Louis de Assis
Data de defesa: 12-09-2018
Programa de Pós-Graduação: Física

MEMBROS DA COMISSÃO JULGADORA DA DISSERTAÇÃO DE MESTRADO DE **RICARDO JAVIER PEÑA ROMAN – RA 190934** APRESENTADA E APROVADA AO INSTITUTO DE FÍSICA "GLEB WATAGHIN", DA UNIVERSIDADE ESTADUAL DE CAMPINAS, EM 12 / 09 / 2018.

COMISSÃO JULGADORA:

- Prof. Dr. Luiz Fernando Zagonel – Orientador – IFGW/UNICAMP
- Prof. Dr. Roberto Magalhães Paniago – DF/UFMG
- Prof. Dr. Pierre-Louis de Assis – IFGW/UNICAMP

OBS.: Informo que as assinaturas dos respectivos professores membros da banca constam na ata de defesa já juntada no processo vida acadêmica do aluno.

CAMPINAS
2018

A Olga, Nataly e Isabella.

Acknowledgements

Ao Prof. Dr. Luiz Fernando Zagonel pela oportunidade e confiança para trabalhar no seu grupo. Por sua paciência, conselhos, ensinamentos e amizade.

Al Prof. Dr. Fernando Alvarez, por su amistad, por la recepción en su laboratório, y por todas las cosas aprendidas durantes las discuciones sobre física en las reuniones de grupo.

Ao Dr. Luiz Tizei pelo fornecimento de algumas amostras. Aos Professores Dr. Fernando Iikawa e Dr. Odilon D. D. Couto Jr. pela colaboração para fazer algumas medidas de fotoluminescência. À Dra. Vanessa Orsi Gordo pela ajuda nos experimentos de fotoluminescência.

A Rafael Merlo e Piacienti, pelo suporte técnico para o desenvovimento do projeto.

A Nataly Herrea por su apoyo incondicional y por su compromiso en esta lucha para salir adelante.

A todos os meus amigos: Vinicius Antunes, Yves Maia Auad, Diego Scoca, Silvia Cucatti, Murilo Moreira e Mawin Martinez. Todos gente boas e belas pessoas.

This study was financed in part by the Coordenação de Aperfeiçoamento de Pessoal de Nível Superior - Brasil (CAPES)-Código de Financiamento 001.

Ao Consejo Nacional de Desarrollo Científico y Tecnológico (CNPq) pelo financiamento parcial do mestrado. Nº de processo 130022/2017-9.

À Fapesp pelo financiamento dos projetos 2014/23399-9 e 2012/10127-5.

À Universidade Estadual de Campinas e à pós-graduação do Instituto de Física "Gleb Wataghin" pelas oportunidades oferecidas e pela formação de qualidade.

Abstract

In this work the morphological, structural, electronic and optical properties of the two-dimensional (2D) materials tungsten diselenide (WSe_2), tungsten disulphide (WS_2) and hexagonal boron nitride (h-BN) were investigated by atomic force microscopy, scanning tunneling microscopy, Raman and photoluminescence spectroscopy. The WSe_2 samples were prepared from bulk material by the mechanical exfoliation method while the WS_2 and h-BN samples were prepared from flakes in solution using drop-casting and spin-coating methods. In order to observe the light emission related to point defects, some samples were subjected to thermal annealing treatments.

Monolayers of WSe_2 on SiO_2/Si 300 nm were located by optical microscopy. The monolayers were confirmed by AFM, Raman and photoluminescence measurements. The Raman results showed the typical Raman signature of monolayer which consists in the observation of the in-plane E^1_{2g} and out-plane A_{1g} Raman modes separated by 11 cm^{-1} around 250 cm^{-1}. In few-layer these Raman modes are degenerate at 250 cm^{-1} and the interlayer vibrational B^1_{2g} Raman mode is observed at 306 cm^{-1}. The B^1_{2g} Raman mode disappears in monolayer due to the absence of the interlayer coupling. From STM images with atomic resolution, it was obtained the lattice parameter $a = (3.2 \pm 0.1)$ Å. The transition from few-layer to monolayer is accompanied by an indirect-to-direct band-gap crossover that leads to observe a strong photoluminescence emission in monolayer, which is twenty times more intense than in few-layer. The light emission in monolayer is dominated by the recombination of A excitons at 1.65 eV at room temperature. The A trions recombination was observed at 1.62 eV and their contribution to the total light emission depends on the excitation power and temperature. The A trions binding energy was estimated as being of 30 meV. The emission associated to the B exciton recombination was observed around 2.0 eV at room temperature and the spin-splitting of the valence band at the K point of the Brillouin zone was determined as being approximately of 370 meV. At low temperature dark exciton states become populated, therefore when the temperature is decreased from 300K to 10K, the photoluminescence intensity falls by about six times. All the properties described here agree with reported results for defect-free monolayers.

The optical activity of commercial WS_2 nanoflakes solution was investigated by absorbance spectroscopy at room temperature, observing the absorption due to A and B exciton at 2.0 and 2.4 eV, respectively. In this case, the spin-splitting of the valence band is about 400 meV. The AFM results showed that most of nanoflakes are few-layer. A STM image of an individual WS_2 nanoflake on p-doped silicon substrate was obtained, but it was not possible to obtain images with atomic resolution in this sample likely due to impurities of the solution on the nanoflake surface. In the case of h-BN samples, the light emission from point defects was observed at room temperature in samples with bulk microflakes subjected to thermal annealing. The light emission related to point defects consist in a narrow emission peak at 2.06 eV associated to zero phonon line transitions, and a phonon replica at 1.90 eV, being the phonon energy 160 meV.

Resumo

Neste trabalho as propriedades morfológicas, estruturais, eletrônicas e ópticas dos materiais bidimensionais (2D) diseleneto de tungstênio (WSe_2), disulfeto de tungstênio (WS_2) e o nitreto de boro hexagonal (h-BN) foram investigadas por microscopia de força atômica, microscopia de varredura de tunelamento, espectroscopia Raman e fotoluminescência. As amostras de WSe_2 foram preparadas a partir do *bulk* pelo método de exfoliação mecânica enquanto que as amostras de WS_2 e h-BN foram preparadas a partir de flakes suspensos em solução usando os métodos de drop-casting e de spin-coating. Para observar a emissão de luz relacionada a defeitos pontuais, algumas amostras foram submetidas a tratamentos térmicos.

Monocamadas de WSe_2 sobre SiO_2/Si 300 nm foram localizadas através de microscopia óptica. As monocamadas foram confirmadas por medidas de AFM, Raman e fotoluminescência. Os resultados Raman mostraram a assignatura Raman típica de monocamadas que consiste na observação dos modos Raman in-plane E^1_{2g} e out-plane A_{1g} separados por 11 cm^{-1} em torno de 250 cm^{-1}. Em flakes com poucas camadas, esses modos Raman têm degenerescência em 250 cm^{-1} e o modo Raman B^1_{2g} correspondente à vibração intercamadas é observado em 306 cm^{-1}. O modo B^1_{2g} desaparece em monocada devido à ausência do acoplamento entre monocamadas. A partir de imagens de STM com resolução atômica foi determinado o parâmetro de rede $a = (3.2 \pm 0.1)$ Å. A transição de poucas camadas a monocamadas é acompanhada por uma mudança de gap no material de indireto para direto, o qual leva a observar uma emissão fotoluminescente que em monocamada é vinte vezes mais forte em comparação à emissão em amostras com poucas camadas. A emissão em monocamadas é dominada pela recombinação de éxcitons A em 1.65 eV a temperatura ambiente. A recombinação de tríons foi observada em 1.62 eV com uma contribuição à emissão total de luz que depende da potência de excitação e da temperatura. A energia de ligação dos tríons foi estimada como sendo de 30 meV. A emissão associada à recombinação de éxcitons B foi observada em torno de 2.0 eV a temperatura ambiente e o splitting da banda de valência no ponto K da zona de Brillouin devido à interação spin-órbita foi determinada como sendo de aproximadamente 370 meV. Em baixas temperaturas os estados de *dark excitons* são populados, portanto quando a temperatura é diminuída de 300K para 10K, o máximo na intensidade da fotoluminescência cai de aproximadamente seis vezes. Todas as propriedades descritas aqui correspondem à propriedades reportadas na literatura para monocamadas sem defeitos.

A atividade óptica de nanoflakes suspensos em solução comercial foi investigada por espectroscopia de absorbância a temperatura ambiente, observando as absorções devida a excitons A e B em 2.0 e 2.4 eV, respectivamente. Neste caso, o splitting na banda de valência por interação spin-órbita é aproximadamente 400 meV. Os resultados de AFM mostraram que a maioria dos nanoflakes têm com poucas camadas de WS_2. Uma imagem de STM de um nanoflake de WS_2 depositado sobre silício dopado tipo-p foi obtida, mas não foi possível obter imagens com resolução atômica provavelmente devido a impurezas da solução na superfície do nanoflake. No caso das amostras de h-BN, a emissão de luz de defeitos pontuais foi observada em temperatura ambiente em amostras com microflakes submetidos a tratamento térmico. A emissão de luz associada a defeitos pontuais consiste

em um pico bem estreito em 2.06 eV associado a transições *zero phonon line* e uma *phonon* réplica em 1.90 eV, sendo 160 meV a energia do fônon.

Contents

1 Introduction

Atomically thin materials are commonly known as two-dimensional (2D) materials. For example, graphene is a 2D material composed by carbon atoms arreanged in a hexagonal lattice (honeycomb structure). It is known that graphene is a monolayer of graphite, and it was mechanically isolated from graphite for the first time by A. Geim and K. Novoselov in 2004 [1]. Consequently, the discovery of its facinating chemical, mechanical and electronic properties [2, 3, 4] gave rise to a growing interest in the last year for exploring the properties and applications of other 2D materials such as Hexagonal Boron nitride (h-BN), Transition Metal Dichalcogenides (MoS_2, WSe_2, etc.), Black Phosphorus (BP), Silicene, Germanene, Metal Chacolgenides (GaSe, SnS, ect.), Transition Metal Oxides (MoO3), and Topological Insulators (Bi_2Te_3, Sb_2Se_3, etc.) [5].

Despite the wonderful electronic properties of graphene, the absence of band gap limits its applications in light emitting devices. Unlike graphite, group-VI transition metal dichalcogenides (TMDs) in their bulk form are indirect band-gap semiconductors [6], but when the thickness is reduced until to obtain a monolayer, the indirect band-gap becomes direct and new electronic and optical properties appear [7, 8]. This property of indirect-to-direct band-gap transition is accompanied by a strong photoluminescence and large exciton binding energy which give to TMDs monolayers great light-emitting properties that makes them promising candidates for opto-electronic and nanophotonic applications [9, 10]. Another important 2D material is the hexagonal boron nitride (h-BN), which is a wide band-gap material ($\sim$6.0 eV) typically used for ultraviolet optical applications [11], but it also is a great dielectric material, and can be incorporated into various heterostructures for the electrostatic gating of other 2D materials [9].

From figure 1.1, it can be observed that the light emission in 2D materials can cover a very wide range of the electromagnetic spectrum due to their diverse electronic properties. Particularly, in the case of TMDs and h-BN, the light emission occurs in the ultraviolet, visible or near infrared region. Some applications according with the spectral range are shown in the top part of the figure. Additionally, these type of materials have the characteristic property that their surface is naturally passivated without any dangling bonds, which makes easy the integration of different layered materials to construct vertical heterostructures without the conventional lattice mismatch issue, because layers with

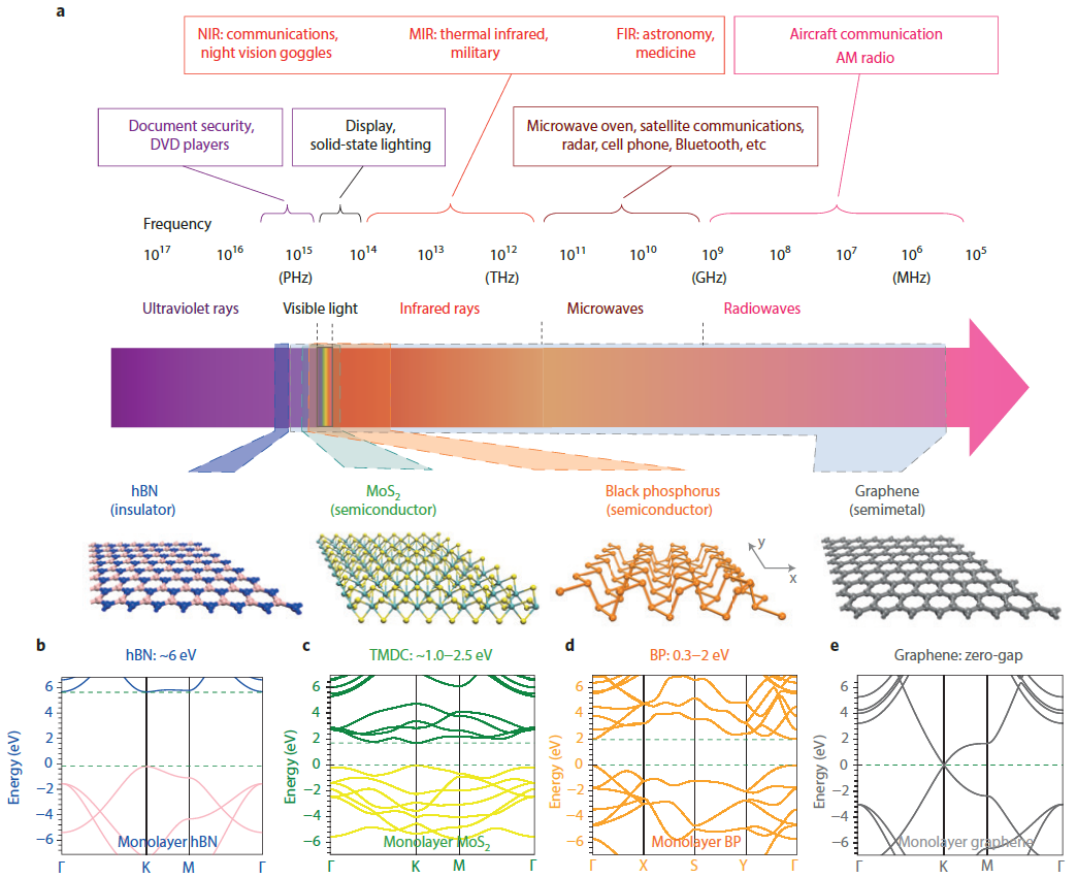

Figure 1.1: (a) Electromagnetic spectrum. Applications that utilize the different spectral ranges are presented in the top portion of the panel. NIR, MIR and FIR indicate near-, mid- and far-infrared, respectively. The atomic structures of h-BN, MoS_2, BP and graphene are shown in the bottom of the panel, left to right. The crystalline directions (x and y) of anisotropic BP are indicated. The possible spectral ranges covered by different materials are indicated using coloured polygons. (b)–(e), Band structures of single-layer h-BN (b), MoS_2 (c), BP (d) and graphene (e). Taken form [9].

different lattice constant in heterostructures are weakly bonded by Van der Waals forces [9]. These materials also can be deposited on flexible substrates and survive to stress and strain compliance of flexible supports, this property opens the door to the fabrication of flexible devices [10].

The properties of TMDs and h-BN described above are normally observed in high crystal quality materials, i.e., materials without structural defects. Undesired structural point defects created during the growth process or during post-preparation treatments may in principle deteriorate their properties. However, if the nature and consequence of defects are well understood, and if their density can be controlled, then they can eventually even be used to tailor the material properties for enhancing them or for achieving new functionalities which may be useful in some applications [12]. Several works have reported that the optical activity and the quantum efficiency in semiconducting TMDs and h-BN can be enhancement and controled by defect engineering, and in some cases, the emission

related to point defects in these type of materials can behavior as single photon emission sources, which are an important element for quantum optics and quantum information [13, 14, 15]. For all these reasons, the band structure/defects engineering based on the structural, electronic and optical properties correlation is one of the most relevant research topic in nanophysics of 2D materials [16].

The direct correlation between a specific type of point defects and their roll in the electronic and optical properties of TMDs and h-BN is still in debate and this is due to the fact that the study of individual point defects in layered material requires the use of experimental techniques with the selectively and sensibility necessary to be able to describe and understand the correlation between the structural, electronic and optical properties at the relevant scale. Microscopy experimental techniques with high spatial resolution, such as transmission electron microscopy (TEM) or scanning tunneling microscopy (STM), have been employed to investigate the morphology and electronic properties of point defects but without any type of information about the optical properties [12, 17]. If TEM or STM microscopes are coupled to light detection optical systems, the optical properties of materials at the nanometer or atomic scale can be explored by luminescence spectroscopy [18, 19]. In our laboratory, a light detection system is being coupled to a commercial low-temperature ultra-high vacuum STM to carry out STM-induced luminesce (STML) experiments and study the optical properties of nanoestructured materials making use of the atomic resolution of STM. Our purpose is to use the high spatial resolution of STM together with scanning tunneling spectroscopy measurements to characterize structural and electronically individual point defects in 2D materials, and additionally to obtain the light emission spectrum by STML.

In this work, the morphological and optical characterization of the 2D materials WSe_2, WS_2, and h-BN is presented. The main aim of this master dissertation is the study of the morphological, structural, electronic and optical properties of some layered materials, as well as, the light emission from point defects. It is expected to find poind defects in samples prepared by the mechanical exfoliation method and in samples subjected to thermal treatment. We decided to study the WSe_2, WS_2, and h-BN materials because they have been reported as being stable in ambient conditions, showing optical emission with high quantum efficiency and quantum emission related to point defects. The morphological and structural properties of these materials will be studied by atomic force microscopy and Raman spectroscopy. The use of Raman and photoluminescence spectroscopy will allow us to know if the sample under investigation is monolayer, multilayer or bulk, and the atomic structure will be explored by scanning tunneling microscopy. These studies will allow us to get insights about the physical properties of this new generation of materials, and from this way know-how to investigate them by STML experiments posteriorly.

This dissertation is constituted by five chapters and three appendixes. The chapter one is the present introduction. In chapter two, the structural, electronic and optical properties of semiconducting TMDs and h-BN are described. In chapter three, the physical principles of the experimental techniques used in this work are briefly discussed. Although the samples were not studied by STML, in this chapter are discussed some important aspects of this technique and how to use STML to characterize individual

point defects in 2D materials. In chapter four are shown and discussed the experimental results, and in chapter five the conclusions are given. In appendices, information about the STM room specifications, sample substrate and STM tips preparation can be found.

2 Physical properties of TMDs and h-BN

Two-dimensional graphene-like materials have been studied extensively in the last years due to their great and tunable electronic and optical properties in monolayers, which are drastically different of that observed in their bulk form. Unlike graphene, some of these materials are semiconductors such as the transitions metal dichalcogenides (TMDs) or insulators such as hexagonal boron nitride (h-BN). The optical properties of these materials are dominated by excitonic effects and can be modulated by defect engineering. In this chapter, it will be discussed the structural, vibrational, electronic and optical properties of semiconducting TMDs and h-BN, as well as, the roll of point defects in the optical properties in these materials.

2.1 Crystal structure

Transition metal dichalcogenides (TMDs) are layered materials with chemical composition MX_2, where M is a transition metal of group 4-10 and X is a chalcogen such as S, Se and Te. There are around 40 TMDs that have been studied experimentally or predicted to be stable theoretically. Depending on the combination of the transition metal and the chalcogen atoms, some of them are metallic, and others are semiconducting or insolating [6, 7]. Our interest in this work is to investigate the structural and optical properties of semiconducting TMDs, particulary group 6 TMDs such MoS_2, WS_2, and WSe_2. The most stable crystal structure of these TMDs is shown in figure 2.1(a), this structure is known as 2H-MX_2 because it consists of two layers of MX_2 within an hexagonal unit cell [20, 21]. The space group of this structure is $P6_3/mmc$ (D^4_{6h}), with M and X atoms in the Wyckoff positions 2c (2/3,1/3,1/4) and 4f (2/3,1/3,z) [21]. The lattice parameter for MoS_2 are $a = 3.160$ Å, $c = 12.295$ Å [22], for WS_2 $a = 3.153$ Å, $c = 12.353$ Å , and for WSe_2 $a = 3.267$ Å and $c = 12.982$ Å [23]. These crystallographic parameters were used to simulate the crystal structure of TMDs shown in figure 2.1 with the *Diamond-Crystal Impact* software [24], where to observe the layered structure more atoms were added to the unit cell. In the figure, $c' = c/2$ represents the distance between MX_2 layers, which are maintained together into the unit cell by Van der Waals interaction following an AbA/BaB order. The capital and lower case latter denote chalcogen and

metal atoms, respectively [6]. From figure 2.1(b) can be seen that an individual monolayer of MX_2 contains three layers of atoms in the sequence X-M-X, i.e., one layer of metal atoms sandwiched between two layers of chalcogen atoms where the M-X bonds are covalent. In the M-X bonds, each metal atom is surrounded by six chalcogen atoms forming the trigonal prismatic coordination. Figure 2.1 (c) shows a top view of a MX_2 monolayer, due to the stacking sequence characteristic of the 2H structure the top view of a single layer looks as a honeycomb structure similar to graphene, with the difference that M and X atoms are not in the same atomic plane. Typically the thickness reported for one monolayer is roughly of 0.7 nm [6].

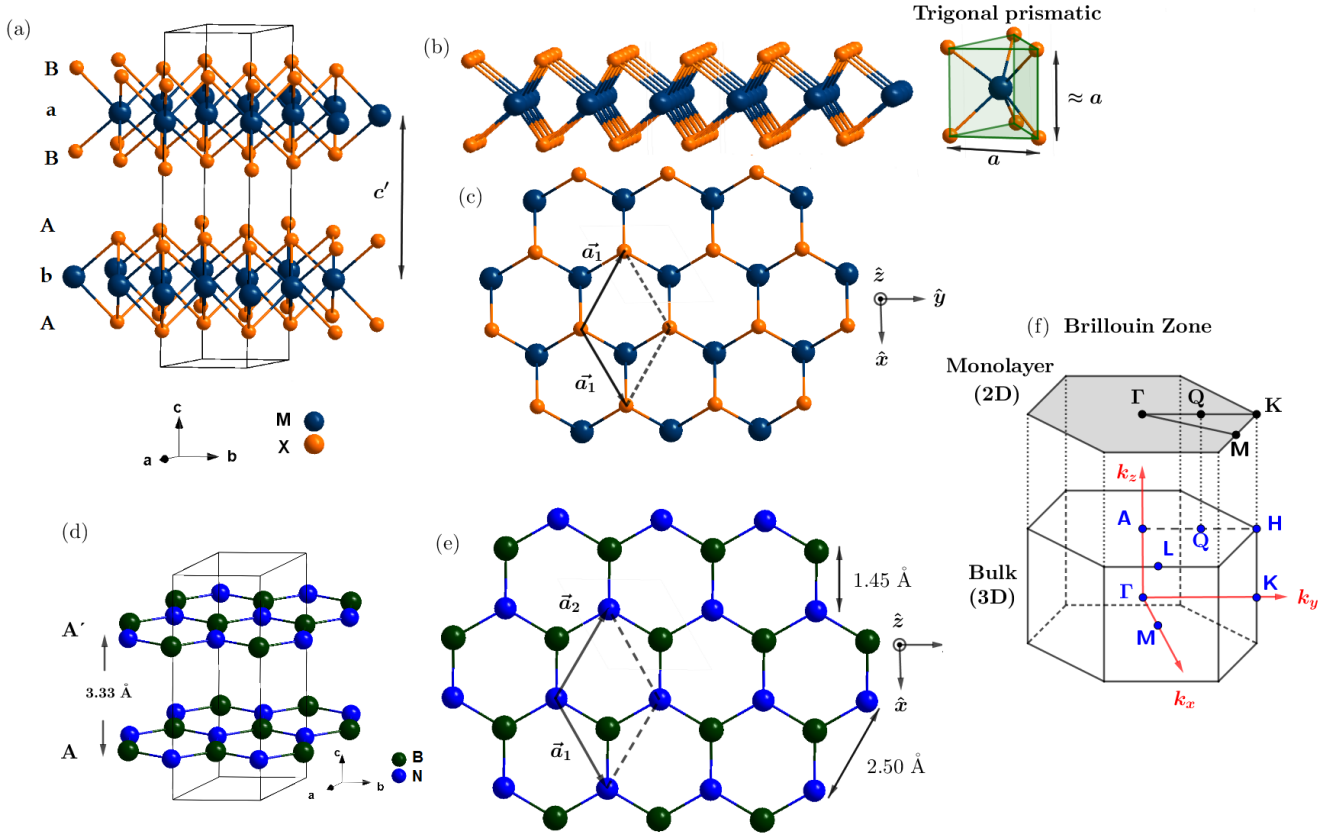

Figure 2.1: (A) unit cell of 2H-MX_2 structure, (b) side view of the MX_2 monolayer and the trigonal prismatic coordination, (c) top view of the MX_2 monolayer, (d) unit cell of h-BN, (e) atomic structure of two-dimensional h-BN, (f) hexagonal first Brillouin zone for both bulk and monolayer.

Hexagonal boron nitride (h-BN) is a layered compound that is isostructural with graphite. Figure 2.1(d) shows the hexagonal unit cell of h-BN with lattice parameters of $a = 2.50$ Å and $c = 6.66$ Å [25, 26, 27], space group $P6_3/mmc$, and boron (B) and nitrogen (N) atoms occupying the Wyckoff positions 2c (2/3,1/3,3/4) and 4d (1/3,2/3,3/4), respectively [28]. In the same way that TMDs structures, more atoms were added to the unit cell to observe the sequence of h-BN layers which are separated by a distance of 3.33 Å [25], following an AA' stacking order where the position of B and N atoms are alternating in each successive layer. These layers are weakly bounded one to another by Van der Waals interaction, which make possible the separation of h-BN in monolayer. In one monolayer of h-BN,

such as occur in graphene, the sp^2 hybridization leads to the formation of in-plane σ bonds (covalent bonds) between B and N atoms that are separated by 1.45 Å [25, 27] in a honeycomb structure such as is shown in figure 2.1(e). The thickness of one monolayer has been found by AFM measurements as being of ~ 0.4 nm [29, 30].

The hexagonal structure of group 6 TMDs and h-BN is described by the lattice vectors:

$$\vec{a}_1 = \frac{a}{2}(\sqrt{3}\hat{x} + \hat{y}), \qquad \vec{a}_2 = \frac{a}{2}(-\sqrt{3}\hat{x} + \hat{y}), \qquad \vec{a}_3 = c\hat{z}. \tag{2.1}$$

These vectors define a hexagonal reciprocal lattice described by:

$$\vec{a}_1^* = \frac{4\pi}{\sqrt{3}a}(\hat{x} + \sqrt{3}\hat{y}), \qquad \vec{a}_2^* = \frac{4\pi}{\sqrt{3}a}(-\hat{x} + \sqrt{3}\hat{y}), \qquad \vec{a}_3^* = \frac{2\pi}{c}\hat{z}. \tag{2.2}$$

which establish a hexagonal shape of the first Brillouin zone such as is shown in figure 2.1(f).

2.2 Vibrational properties and Raman modes

From the crystal vibration theory it is known that for a three dimensional crystal with z atoms per primitive unit cell and three freedom of movement per atoms, there are $3z$ vibrational normal modes, where 3 are acoustic modes and $3(z-1)$ are optical modes [31]. In the case of the 2H-MX_2 bulk structure of TMDs, there are six atoms per primitive unit cell (see figure 2.2(a)) and a total of 18 vibrational modes which are conformed by 3 acoustic modes, 7 Raman modes, 3 infrared modes, and 5 inactive modes [32]. Due the fact that the 2H-MX_2 structure has D_{6h} point group symmetry, group theory shows that these vibrational modes in the center of the Brillouin zone (Γ point) can be expressed as [32, 33]:

$$\Gamma_{\text{2H-MX}_2} = \text{A}_{1\text{g}} + 2\text{A}_{2\text{u}} + 2\text{B}_{2\text{g}} + \text{B}_{1\text{u}} + \text{E}_{1\text{g}} + 2\text{E}_{1\text{u}} + 2\text{E}_{2\text{g}} + \text{E}_{2\text{u}}. \tag{2.3}$$

where A and B modes involve out-of-plane atomic displacement and are non-degenerate while the E modes correspond to in-plate atomic displacement and are doubly degenerate which means that the atomic displacement can be observed in longitudinal and transversal directions. In eq. (2.3) one A_{2u} and one E_{1u} are acoustical modes, (A_{1g}, E_{1g}, E_{2g}) are the active Raman modes, another A_{2u} and E_{1u} are the infrared active modes, and (B_{2g}, B_{1u}, E_{2u}) are optically inactive [32, 33]. Figure 2.2 shows the atomic displacement for the active Raman modes A_{1g}, E_{1g}, E^1_{2g}, and E^2_{2g}. The A_{1g} and E_{1g} are out-of-plane and in-plane vibration modes of the chalcogen atoms, respectively; being the last mode forbidden in the back-scattering Raman configuration [34, 35]. The E^1_{2g} mode involve in-plane atomic displacement of both metal and chalcogen atoms in opposite directions. E^2_{2g} is a shear mode in which two layers are vibrating one against another, this mode is observed at very low frequency ($50< \text{cm}^{-1}$) and disappear in monolayer [32, 35].

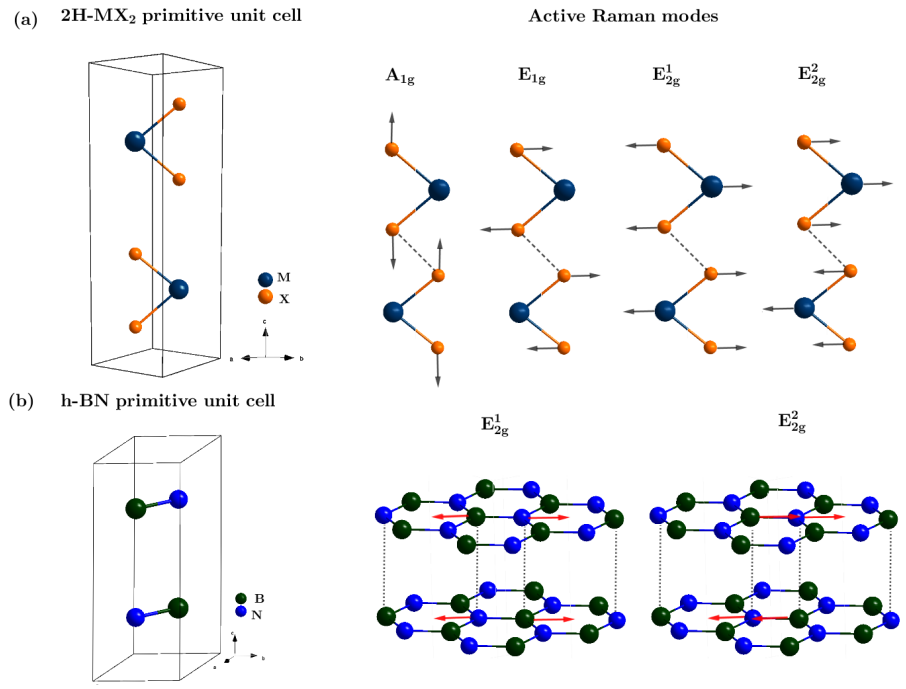

Figure 2.2: Primitive unit cell and active Raman modes for (a)the 2H-MX_2 structure of TMDs, and (b) h-BN strucrure.

In the crystal structure section was discussed that h-BN has a layer-structure similar to that of graphite with four atoms per primitive unit cell such is shown in figure 2.2(b). The irreducible representation for the 12 vibrational modes of h-BN at the Γ point of the Brillouin zone is [36]:

$$\Gamma_{\text{h-BN}} = 2A_{2u} + 2E_{1u} + 2E_{2g} + 2B_{1g}. \tag{2.4}$$

where one A_{2u} and one E_{1u} are acoustical modes, another A_{2u} and E_{1u} are active infrared modes, B_{1g} are inactive optical modes, and E_{2g} are active Raman modes [36]. Therefore, for h-BN there are 3 acoustic modes, 3 active infrared modes, 2 inactive modes and 4 active Raman modes. From figure 2.2(b) can be seen the Raman modes E_{2g}, where in the same way that vibrations in TMDs, the E modes are vibrations with in-plane atomic displacement. The E^1_{2g} mode corresponds to the intralayer vibration where B and N atoms are vibrating in opposite directions, and the E^2_{2g} is the interlayer shear mode. The E^1_{2g} modes have been reported at 1367.5 cm^{-1} (FWHM= 18.2 cm^{-1}), 1366.6 cm^{-1} (FWHM= 15.2 cm^{-1}), and 1365.1 cm^{-1} (FWHM= 10.3 cm^{-1}) for monolayer, multilayers and bulk samples, respectively [13]. The E^2_{2g} mode is found at low frequency [37] and have been reported at 52.5 cm^{-1} in bulk with a shift down to 38.0 cm^{-1} for bilayer [38].

2.3 Electronic and optical properties of TMDs

2.3.1 Band structure

All the semiconducting TMDs with 2H-MX_2 structure have an indirect band-gap in their bulk form. By decreasing the number of layers of the bulk crystal, the band-gap energy starts to increase and, in the limit of a single monolayer, there is a transition from indirect to direct band-gap [8, 39]. In order to discuss the electronic properties of group 6 TMDs let's consider MoS_2 as an example. Figure 2.3(a) shows the electronic band structure of MoS_2 calculated by Density Functional Theory (DFT), where it can be seen that in the bulk form MoS_2 is a indirect band-gap semiconductor with transitions between the valence band (VB) maximum at the center Γ point of the hexagonal Brillouin zone (Γ_V) and the conduction band (CB) minimum positioned between the Γ and K point (Λ_C). When the number of layers is reduced from bulk to monolayer, the band extremes are moved to the K point and the band-gap becomes direct [8, 12, 39].

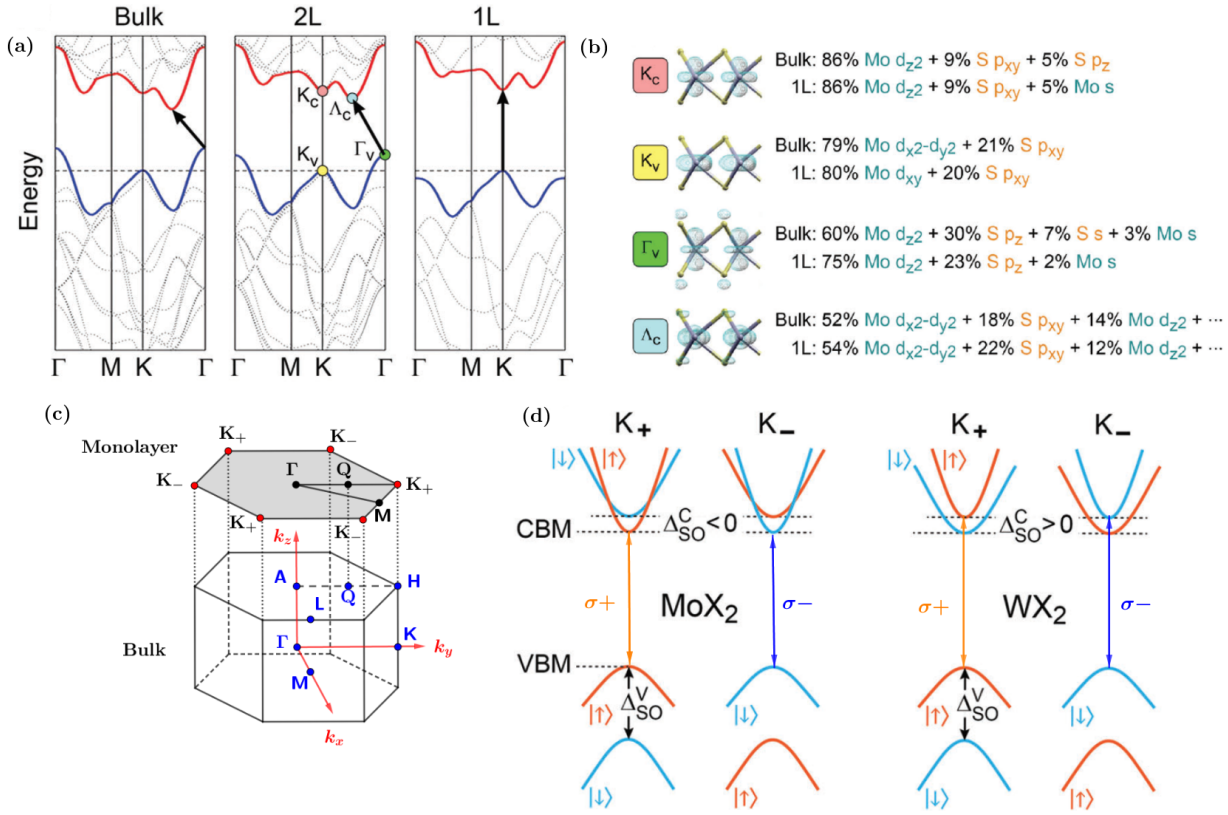

Figure 2.3: Electronic properties of Group 6 semiconducting TMDs. (a) Electronic band structure calculated by DFT for MoS_2. (b) Orbital composition in the electronic band structure of MoS_2. (c) Hexagonal Brillouin zone. (d) Schematic illustration of the valence and conduction bands at the $K_\pm$ valleys in molybdenum (MoX_2) and tungsten (WX_2) dichalcogenides. Adapted form [12].

The effect of the number of layers on the electronic structure of TMDs can be explained considering the atomic orbital contribution to the band structure such as is shown in figure 2.3(b). The electronic states at the Λ_C and Γ_V point contain a very important contribution from the p_z orbitals of the chalcogen atoms and the d_z orbitals of the transition metal atoms which lead to have a dependence of the electronic levels on the interlayer coupling due to the overlap of the wave function in z directions (c-axis of the crystal). Since the chalcogen atoms are the responsible by the interlayer interaction, the band structure modification at Γ with the number of layers is defined by the p_z orbital contribution. Therefore, when the number of layers decreasess, the p_z orbital contribution at Γ decreases too and the indirect band-gap becomes larger until achieve the monolayer configuration where the band-gap transition is observed. In the K point, the most important orbital contribution at the edge of the VB and CB is given by the $d_{x^2} + d_{x^2}$, d_{xy}, d_{z^2} and p_{xy} orbitals, this means that the electronic states are localized into the monolayer and do not depend on the number of layers [39, 40, 41].

The energy states at the edges of the Brillouin zone are referred as K_+ and K_- valleys, depending on the band spin-state, and the term valley is used to designate band extremum in momentum space [12, 42]. Figure 2.3(c) and (d) show that 2H-MX_2 monolayers are direct band-gap semiconductors with optical transitions at the corner of the Brillouin zone. The presence of direct-band gap is important for potential applications involving efficient light emission process. Additionally, the direct optical transitions are valley selective, i.e., σ_+ and σ_- circularly polarized light can excited electronic transitions only at the K_+ and K_- valleys, respectively. On the other hand, the spin-orbit interaction produce a spin-orbit-split of several hundred of meV in the VB and a few of tens of meV in the CB. The spin-orbit splitting in the CB has different signs for molybdenum (MoX_2) and tungsten (WX_2) dichalcogenides, which give rise to novel features such as dark and bright excitons [7, 42, 43]. Excitons can be bright or dark, depending on the spin orientation of the charge carries. In bright excitons, the electron and the hole have parallel spins and can recombine with the emission of a photon. In dark excitons the electon an hole have antiparallel spins, then due to the spin conservation, the recombination with photon emission cannot occurs.

2.3.2 Optical properties and excitonic effects

By shining materials with light and analysing their optical properties one can in turn acquire information about their electronic structure. The optical response in semiconducting TMDs monolayer is dominated by excitonic effects [7, 43]. After the absorption of a photon, an electron from a filled state in the VB is promoted to an empty state in the CB; the empty electron state leaved in the VB is referred to a "hole". The electrostatic interaction between electron and hole involved in the electronic transition leads to the formation of a bound electron-hole pair known as *exciton*. An exciton (X^0) is a quasiparticle electrically neutral; however, this can capture an extra electron or hole to form an exciton negatively charged (X^-) or positively charged (X^+) called *trion* [42].

In bulk semiconductors (3D structures), excitons can be described as a hydrogen-like system in which the binding energy of the electron-hole pair is given by [44, 45]:

$$E_{X^0}^{3D} = -\frac{13.6\mu}{m_e\varepsilon^2}\frac{1}{n^2}eV, \tag{2.5}$$

where $n = 1, 2,...$ is the principal quantum number for the exciton levels, $\mu = m_e m_h/(m_e + m_h)$ is the effective reduced mass of exciton, being m_e and m_h the effective masses of electron and hole, respectively; and ε is the effective dielectric constant of the medium. In the case of 2D system with quantum confinement such as semiconducting quantum wells, the hydrogen model shows that the exciton levels are given by [45]:

$$E_{X^0}^{2D} = -\frac{13.6\mu}{m_e\varepsilon^2}\frac{1}{(n-1/2)^2}eV, \tag{2.6}$$

where $E_X^0(n)$ varies as $1/(n-1/2)^2$ rather $1/n^2$, which implies that the binding energy of the exciton ground-state ($n = 1$) is four times larger in 2D than in 3D structures. Its important to know that the exciton levels are allowed electronic levels localized into the band-gap (see figure 2.4) and electronic transitions with energies $E_g - E_X^0(n)$ are typically observed in absorption or luminescence spectra [44, 45]. In general, the exciton binding energy in some usual semiconductors like GaP or GaAs is $E_{X^0}^{3D}(n = 1) < 30$ meV [45], so the excitonic effects only can be observed at low-temperature where the thermal energy ($k_B T$) is not enough to dissociate the formed excitons. Since $E_{X^0}^{2D} = 4E_{X^0}^{3D}$, excitons in 2D system can be observed easily even at room temperature where $k_B T \sim 25$ meV.

Table 2.1: Values of some electronic parameters in semiconducting TMDs [12].

Property	**Symbol**	**$MoSe_2$**	**MoS_2**	**WSe_2**	**WS_2**
Electronic band-gap (eV)	E_g (bulk)	1.09	1.29	1.20	1.35
	Eg (monolayer)	2.2	2.5	2.1	2.7
Optical gap (eV)	E_{opt}	1.58	1.90	1.65	2.00
Exciton binding energy (eV)	E_b (monolayer)	0.6	0.6	0.5	0.7
CB spin-orbit splitting (meV)	Δ_{SO}^C	-21	-3	36	29
VB spin-orbit splitting (meV)	Δ_{SO}^V	180	160	430	380
PL peak position (eV)	A (monolayer)	1.58	1.92	1.65	2.02
	B (monolayer)	1.76	2.08	2.08	2.40
UV-Vis absorption peak position (nm)	A	810	673	750	628
	B	708	612	595	525

The reason for which the optical response in TMDs monolayer is dominated by excitonic effects is that the quantum confinement in these atomically thin 2D system produce a strong interaction between electrons and holes that impose an exciton binding energies in the range of few hundreds of meV, see table 2.1. The main properties of the exciton levels in TMDs monolayer are represented in figure 2.4. The figure 2.4(a) shows that in monolayer there is a strong confinement of excitons and the dielectric screening is reduced due to changes in the dielectric environment [42, 46]. The dielectric screening is reduced because the electric field lines that keep the electron and hole together begin to

extend outside of the sample yielding an enhancement of the Coulomb interaction. Figure 2.4(b) shows the exciton levels localized into the band-gap and the optical transitions that may be observed by optical absorption. The figure also clarifies the difference between the electronic band-gap E_g and the optical gap E_{opt}, the first one corresponds to the necessary energy to produce an electronic transition form the VB to the CB, and the second one is the energy for an electronic transition between the VB and the exciton ground-state. On the other hand, the exciton binding energy is obtained by $E_b = E_g - E_{X^0}(n=1)$. Hence, to know the exciton binding energy in monolayers, the energy band-gap and the exciton transition energy $E_{X^0}(n=1)$ must be obtained first. The latter can be obtained easily by means of optical spectroscopy (absorption, photoluminescence, reflectance, etc.) [41], but the precise determination of E_g is a challenging problem because the large exciton binding energy and the strong optical exciton resonance may mask the band-to-band transition. One way to obtain E_g is carry out Scanning Tunneling Spectroscopy (STS) measurements where the local density of states of the sample can be measured [42].

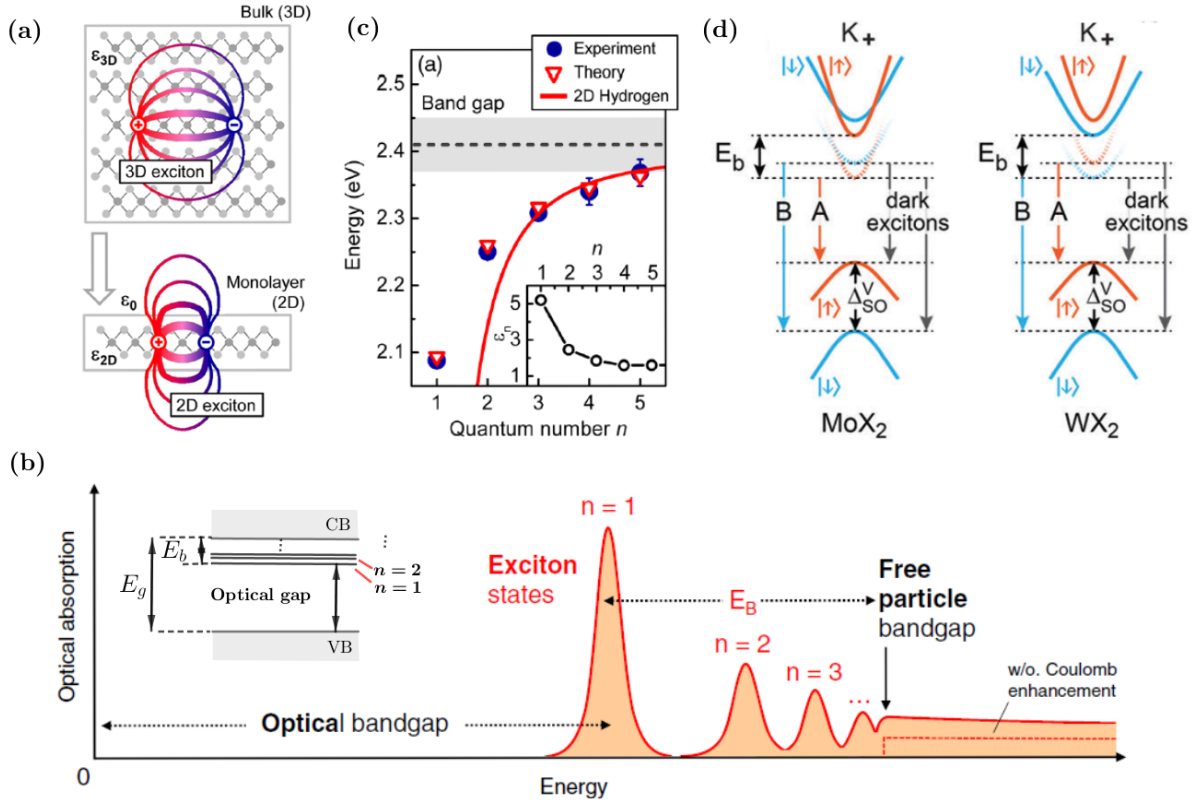

Figure 2.4: (a) Representation of excitons in TMDs bulk and monolayer [46]. (b) schematic illustration of the optical absorption in 2D semiconductor including the series of exciton transitions into the band-gap. Adapted from [42]. (c) Experimental and theoretical transition energies for the exciton states as a function of the quantum number n, the corresponding effective dielectric constants are shown in the inset figure [46]. (d) Energy diagram for the exciton ground-state in the K_+ valley for MX_2 and WX_2 compounds [12].

From Figure 2.4(c) it can be see that the exciton state levels cannot be described by the conventional hydrogen model because the modification of the dielectric screening associated with the inhomogeneous dielectric environment of TMD monolayers have not been taken into account. The nonhydrogenic behavior of the exciton states can be explained considering that the screened electron-hole interaction is given by the potential [42, 46, 47]:

$$V_{eh}(r) = -\frac{\pi e^2}{(\varepsilon_1 + \varepsilon_2) r_0}\left[H_0\left(\frac{r}{r_0}\right) - Y_0\left(\frac{r}{r_0}\right)\right], \tag{2.7}$$

where H_0 and Y_0 are the Struve and Bessel functions, r is the relative electron-hole coordinate, r_0 is the effective screening length, ε_1 and ε_2 are the dielectric constants for the surround environment of the monolayer (vacuum and substrate). The theoretical exciton levels obtained using eq. (2.7) are represented as red triangles in figure 2.4(c) which are in agreement with the experimental points.

In figure 2.4(d), a schematic diagram of the K_+ valley band-structure is shown to illustrate the position of the exciton ground-state into the band-gap. The absorption and luminescence spectra of TMD monolayers are characterized by the presence of two excitonic peak called A and B, that arise from direct electronic transitions at K from the spin-orbit splitting in the VB to the spin-orbit splitting of the exciton ground-state near to the CB. The values for A and B transitions, exciton binding energy, VB spin splitting (Δ^V_{SO}), and CB spin splitting (Δ^C_{SO}) for some semiconfucting TMDs are listed in table 2.1. The difference in sings of Δ^C_{SO} for molybdenum and tungsten dichalcogenides compounds leads to two type of optical response in monolayers: (i) optically bright monolayer with the aligned spins in the upper VB and the lowest CB subbands ($\Delta^C_{SO} > 0$), and thus optically active ground-state transition (bright exciton), and (ii) optically darkish monolayers with antiparallel spins in the upper VB and the lowest CB subbands ($\Delta^C_{SO} < 0$), thus the ground state transition is optically inactive (dark exciton). The bight or darkish character of monolayer give rise to different temperature-dependent photoluminescence in MoX_2 and WX_2 compounds. The values shown in table 2.1 indicate that the ground state of $MoSe_2$ and MoS_2 monolayers should be bright, while for WSe_2 and for WS_2 it is likely to be dark [12, 42, 43].

The electronic transitions and the exciton recombination in TMDs lead to light emission from the visible to near-infrared range of the electromagnetic spectrum. Some of the typical electronic transitions observed by optical spectroscopy in TMDs are summarized in figure 2.5. The excitonic transitions A and B are shown pictorially in figure 2.5(a) where it can be seen the fine structure of the excitonic features which consists in a splitting between peaks attributed to the formation of trions labelled as A^- and B^-, with binding energy E_{A^-} and E_{B^-}, respectively; and E_A is the A exciton binding energy [47]. Figure 2.5(b) shows that the fine structure for A exciton in $MoSe_2$ monolayer can be resolved by photoluminescence spectroscopy (PL) at low temperature (20 K), where X^0 is the neutral exciton peak and X^- is the trion peak, being the trion binding energy of 30 meV [48]. On the other hand, figure 2.5(c) shows a PL spectrum of MoS_2 monolayer taken at room temperature, the peaks related to A and B excitons are observed at ~ 1.9 and 2.0 eV , respectively. Additionally, the figure also shows that the PL peak corresponding

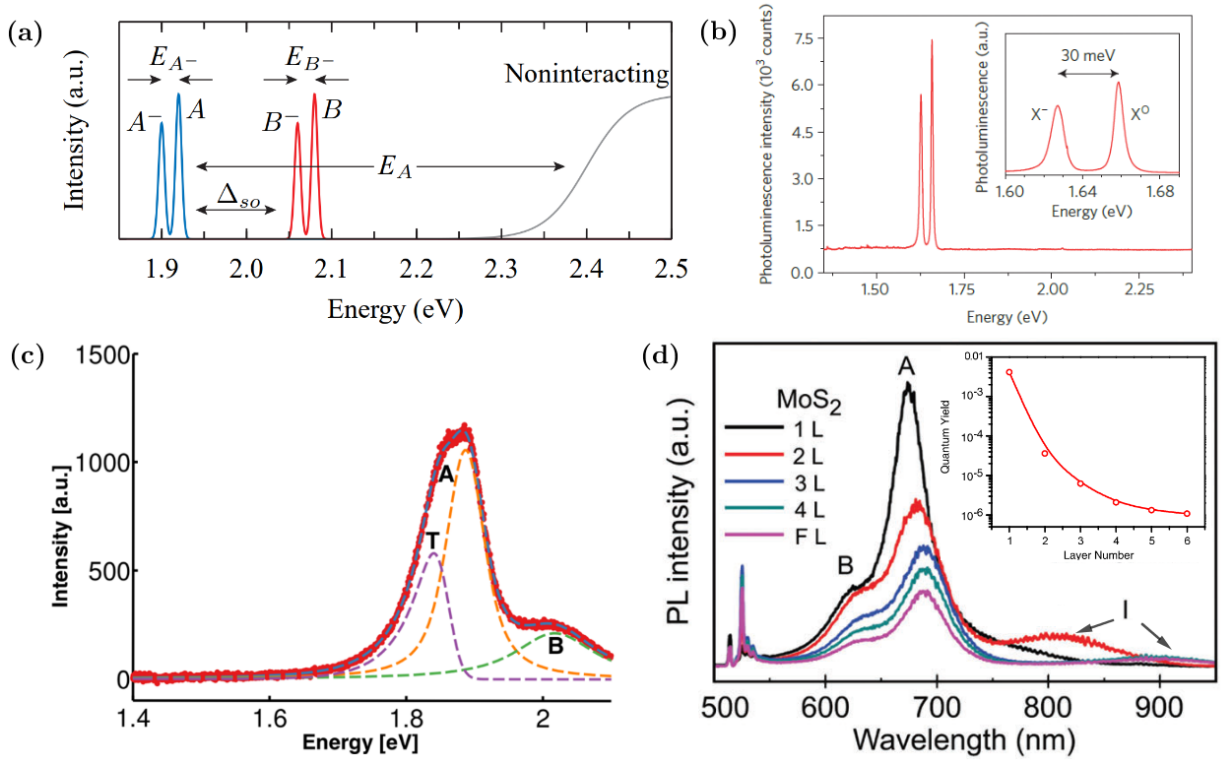

Figure 2.5: (a) Schematic absorption spectrum [47]. (b) PL spectrum of $MoSe_2$ at 20 K. Inset: detailed view showing both exciton X^0 and trion X^- peaks [48]. (c) PL spectrum of MoS_2 at room temperature. A and B denote excitons, and T denote trions [49]. (d) PL spectra of MoS_2 with different thicknesses, ranging from monolayer(1L) to few-layer (FL) [50]. The inset shows the PL quantum yield of MoS_2 as function of the number of layers [8].

to A excitons is a superposition given by the recombination of neutral excitons and trions (T) [49]. In general, the proportional share of excitons and trions contribution in peak A depends on the sample doping and the substrate [12]. The PL intensity dependence on de number of monolayer of MoS_2 is shown in figure 2.5(d). The direct band-gap of MoS_2 monolayer produces the strongest PL intensity, but by increasing the number of layers the PL intensity decrease due to the direct-to-indirect band-gap transition. All the emission spectra present two peak associated to A and B excitons. From bilayer to few-layer, a third PL peak I is observed and it is attributed to indirect transitions through the indirect-band gap between the VB and CB [50]. The inset figure shows the luminescence quantum efficiency for MoS_2 as function of the number of layers. Monolayer exhibits strong photoluminescence emission, their PL quantum yield (number of emitted PL photons to number of incident photons) decrease several order of magnitude in bilayer and few-layer samples. Mak, *et al.*, have reported that freestanding MoS_2 monolayer exhibits an increase in luminescence quantum efficiency by more than a factor of 10^4 compared with the bulk material [8].

2.3.3 Point defects in TMDs

Semiconducting TMDs without structural defects have great physicochemical properties, but undesired structural defects created during growth process or during post-preparation treatments may in principle deteriorate their properties. However, if the nature and consequence of defects are well understood, and if their density can be controlled, then they can eventually even be used to tailor the properties of TMDs for enhancing them or for achieving new functionalities which may be useful in some applications [12, 16]. Apart of unintentional native defects, the type and concentration of defects can be controlled *in situ* by tuning the synthesis parameters [51, 52] or modified *ex situ* by thermal annealing [53, 54], plasma treatment [54, 55] or electron (ion) beam irradiation [53, 56]. The type of defects in 2D materials can be classified according with the defect's dimensionality in: point defect (0D), line defect (1D) and planar defect (2D). The point defects can be divided in: *vacancies*, *antisites*, *substitucionals*, *interstitials*, *adatoms*, and *topological defects* [57]. Such as is shown in figure 2.6(a), individual point defects in TMDs can be imaged by aberration-corrected high-resolution transmission electron microscopy (AC-HRTEM) and by aberration-corrected annular dark-field scanning transmission electron microscopy (ADF-STEM). ADF-STEM has an additional advantage of contrast sensitivity to the square of the atomic number (Z) of the atoms being scanned and thus provides valuable information on chemical composition, atom-by-atom [12, 16].

The optical properties of TMDs can be modulated by defects engineering. For example, several works have reported that weak PL emission of monolayer MoS_2 is mostly due to the formation of negative trions in n-doped sample [58, 59]. However, strong enhancement of PL can be realized through thermal treatment [59] or oxygen plasma irradiation [54], see figure 2.6(b) and (c). The proposed physical mechanism behind PL enhancement is the formation of Mo-O bonds that introduce p-doping in the sample, which give rise to the conversion of trions in exciton whose recombination is radioatively more efficient [58, 59, 60]. On the other hand, point defects in TMD monolayer can localize excitons, these are excitons trapped in potential wells crated by atomic defects or impurities in the crystal lattice. Defect-bound excitons can act as sources of single photon emission [61, 62]. The energy of single photon emission is 20-100 meV lower than that of excitons, and the emission shows sharp line width of 58-500 μeV [63, 64]. Single photon emitters are important elements for quantum information processes [61, 65]. Figure 2.6(d) shows the observation of single photon emitter in monolayer WSe_2 . In figure 2.6(d)-(i) is shown the typical PL spectrum of a monolayer (ML) taken at 10 K in the center of the flake shown in figure 2.6(d)-(ii) and (iii), where the emission due to A neutral exciton (X^0) and trions ($X^{\pm}$) are observed at 1.75 and 1.72 eV, respectively; and a strong emission attributed to defect-bound excitons is observed between 1.6 and 1.7 eV. This spectrum shows small variations in the integrated PL intensity image across most part of the monolayer. However, at some locations close to the edge of the monolayer, the characteristics of the emission change drastically. The PL spectrum in that region is shown in figure 2.6(d)-(iv) and it exhibits several sharp spectral lines, with the strongest one at 1.70 eV. The temporal second-order correlation function shown in figure 2.6(d)-(v) demonstrate that the emission center at 1.70 eV is a single-photon emission source[66].

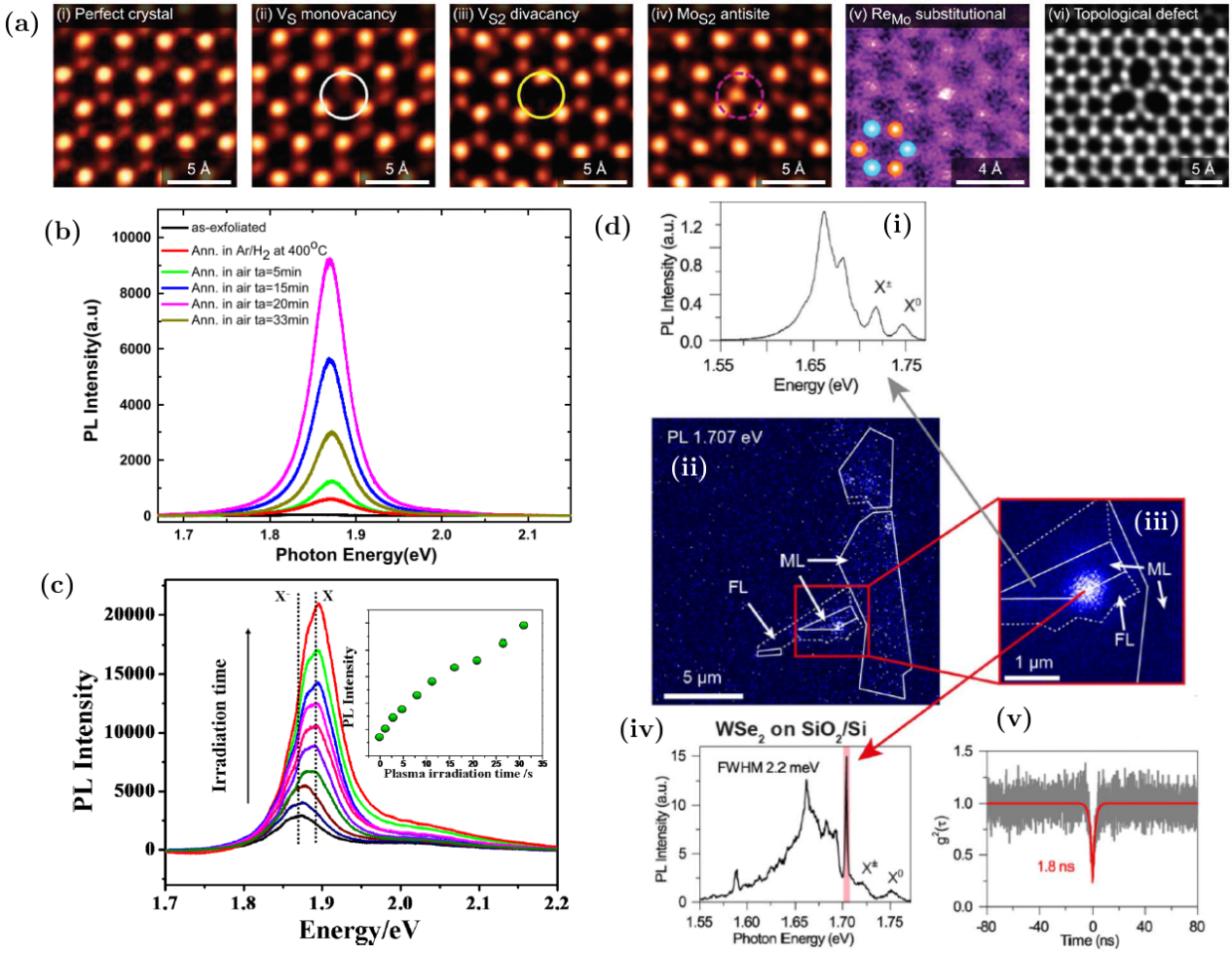

Figure 2.6: (a) Typical point defects observed in 2H-MX_2 TMDs. Figures (i)-(v) are image of MoS_2 and (vi) is an image of WSe_2 [12]. (b) PL spectra of the samples: as-exfoliated, annealed in the protecting gas Ar(95)/H2(5) at 400 ^{o}C, and the samples annealed in air at 300 ^{o}C for different time (ta) [59]. (c) PL spectra of MoS_2 monolayer after oxygen plasma irradiation with different durations [54]. (d) Single photon emission from localized excions in monolayer WSe_2: (i) PL spectrum at 10 K, (ii) PL image at a photon energy of 1.707 eV, (iii) PL image with a single photon emission center, (iv) PL spectrum of a single photon emission center, and (v) second-order correlation function of the single emitter, adapted form ref [66].

2.4 Electronic and optical properties of h-BN

2.4.1 Band structure

h-BN is a large band-gap material of about 6 eV [67, 15]. The indirect or direct character, as well as, the real value of the band-gap is still in debate in the literature [11]. Cassanois *et al.* reported that h-BN is a indirect band-gap material [68], and Watanabe *et al.* reported that it has a direct band-gap [69]. Theoretical calculation of the h-BN band structure predict a direct band-gap using the tight binding theory [70], while the DFT calculation predicts an indirect band gap [71]. The most accurate determination of the

h-BN band structure have been reported by Arnaud *et al.* [72] and Wirtz *et al.* [73] who have used the GW method to determine the electronic band structure, see figure 2.7(a). Arnaud *et al.*, predicted an indirect band-gap of 5.95 eV and direct band-gap of 6.47 eV at H point of the Brillouin zone, while Wirtz *et al.* predicted and indirect band-gap between 5.53 and 5.99 eV and a direct band-gap between 6.03 and 6.48 eV. More recently Roldán *et al.* [74] used DFT calculation and reported that h-BN in monolayer has a direct band-gap of $\sim$ 4.5 eV at the K point of the Brillouin zone, such as is shown in figure 2.7(b).

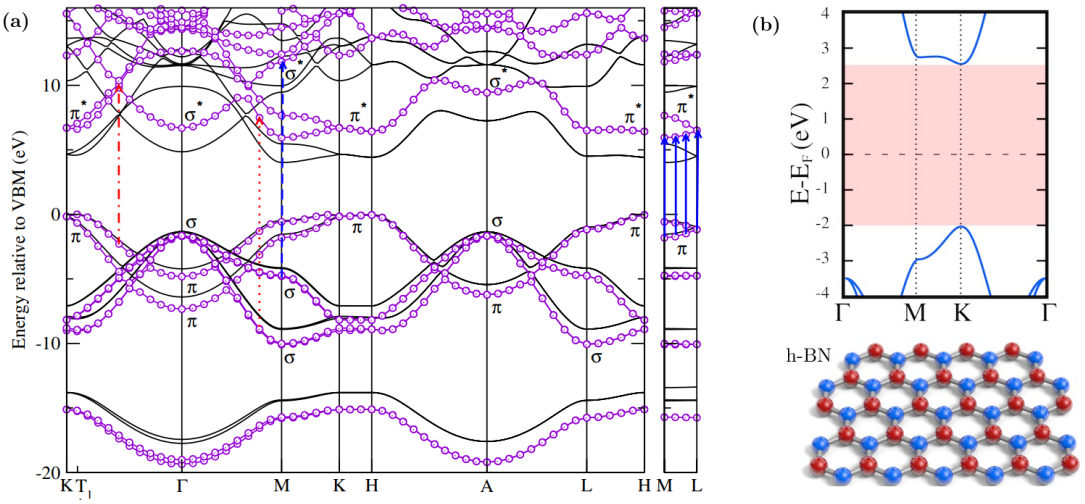

Figure 2.7: (a) Electronic band structure of h-BN [73]. (b) Band structure of h-BN monolayer [74].

2.4.2 Optical properties and point defects

In the last years, h-BN has emerged as a candidate for optoelectronic applications in the far ultraviolet (UV) region [75, 76]. The luminescence properties of h-BN are dominated by excitonic effects, specifically by Frenkel type excitons [11, 76] which are tightly bond excitons localized in the atomic sites. Frenkel excitons have a radius comparable to the size of the unit cell and have binding energies of the order of 0.1-1.0 eV [45]. The study of the electronic and optical properties of h-BN use to be difficult due to the fact that it is necessary to work in the far UV range; however, the emission properties can be explored by cathodoluminescence spectroscopy [15, 11]. Figure 2.8 shows cathodoluminescence spectra of h-BN taken at room temperature. The emission spectrum in figure 2.8(a) was taken in a high quality h-BN crystal, where a single emission peak associated with the recombination of Frenkel excitons is observed at 5.9 eV (210 nm) [69]. In common h-BN samples, the emission signatures are more like spectrum in figure 2.8(b), where a more complex emission is observed [11]. The spectral features shown in figured 2.8(b) indicate that defects have an important roll in the optical behavior of h-BN. Particularly, the effects of point defects in h-BN have been extensively studied in the last years due the fact that the electronic levels that defects place into the band-gap lead to light emission in the near-UV to visible range, and similar to TMDs, the emission related to defects behave

as single photon emission sources [61, 11, 77]. Point defects in h-BN can be created by thermal treatment [13, 78, 79], e-beam irradiation [79], plasma treatment [80] and ion implantation [14].

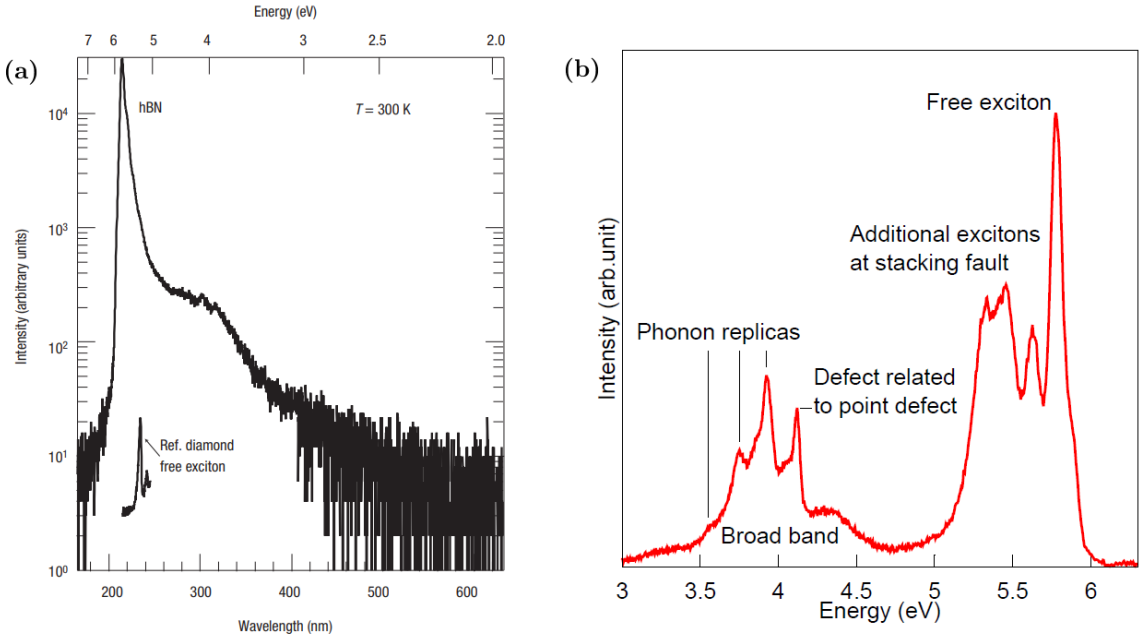

Figure 2.8: (a) Cathodoluminescence spectrum of high quality h-BN crystal [69]. (b) Cathodoluminescence spectrum of a thin h-BN flake [11].

The light emission in the visible and near-infrared ranges associate to point defects in h-BN has been explored recently by Tran, *et al.*, in bulk [78], few-layer [79] and monolayer [13] samples. In figure 2.9(a), a photoluminescence map of bulk h-BN crystal is shown which was obtained using a 532 nm excitation laser at room temperature. The PL map shows several isolated emission centers and assembles of these centers. The PL spectrum of the emission center in the red circle is shown in figure 2.9(b), which reveals two sharp peak at 618 and 629 nm. Both peak are associated to zero-phonon line (ZPLs) transitions of deep point defects in the crystal. The background spectrum taken from a region adjacent of the emission center shows two Raman peak at 575 and 583 nm. The second-order correlation function shown in figure 2.9(c) probe that the emission peaks observed in the PL spectrum correspond to isolated defect that emits single photons [78]. On the other hand, figure 2.9(d) shows a PL map of h-BN nanoflakes multilayer taken at room temperature using a 532 nm laser. From the PL spectra in figure 2.9(e) it can be seen that point defects in multilayer can emit over a broad range. The emission centers have narrow ZPLs at energies in the range of 1.6-2.2 eV (∼565-775 nm) and are classified into two groups based on their ZPL energy and phonon side band (PSB) spectral shapes. The group 1 consists of emitters with ZPL at 1.90, 1.96, 2.06, 2.13, and 2.15 eV; the emission exhibit a broad and asymmetric ZPL shape with pronounced double PSBs. In group 2 the emission centers have ZPL at low energies, centered at 1.63, 1.74, 1.78, and 1.82 eV. The ZPLs are narrower and more symmetric than the observed in group 1, being the PSB weaker. The second-order correlation function shown in figure 2.9(f) prove

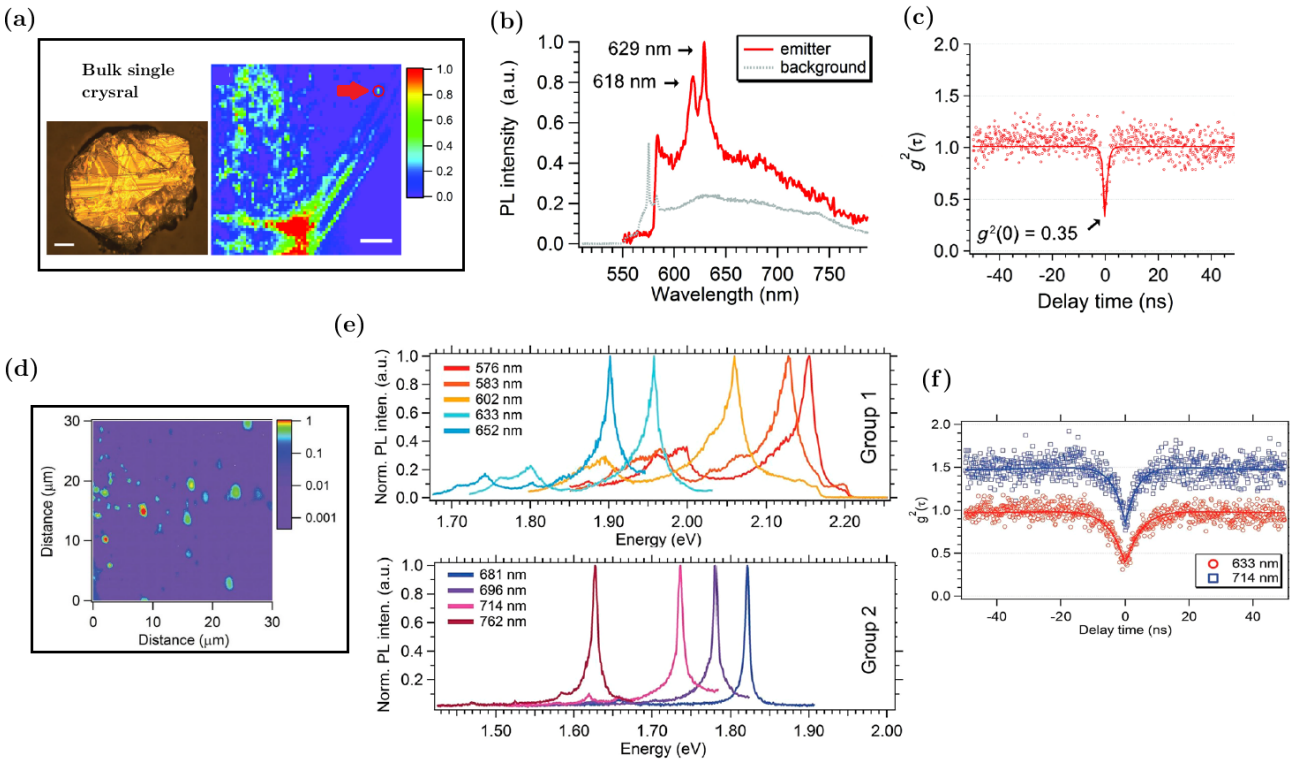

Figure 2.9: (a) Optical microscope image of bulk h-BN crystal, the scale bar indicates 100 μm, and PL map of bulk h-BN where the scale bar indicates 10 μm. (b) PL spectrum at room temperature of the isolated center in the red circle, and (c) second-order autocorrelation function recorded from the defect center. Adapted from [78]. (d) PL map of h-BN multilayer, (e) PL spectra of single photon emitter in h-BN multilayer, and (f) second order autocorrelation function, the blue curve has been shifted intensionally in the vertical axis until 1.5 in order to observe the anti-bunching behavior at zero delay time . Adapted from [79].

that defects in the h-BN multilayer are point defects and act as single photon emitters. Based on theoretical models, Tran, *et al.* have reported that the supposed point defects responsible by the single photon emission is of the type N_BV_N in which one N atom is vacant and an adjacent B atom is substituted with N [13, 79]. However this affirmation is still in debate, as well as, that the variation in ZPL position is due to local strain effects [79].

3 Experimental techniques

In this chapter, the experimental techniques used to study the morphological and optical properties of the samples are described. STM was used to obtain image with atomic resolution and study the atomic structure of the samples, and AFM was used to obtain topographic information of the samples and correlates the morphological characteristic with the optical properties observed by Raman and PL spectroscopies. Although the luminescence properties of the samples were not investigated using STML, an introduction to the basic concepts of this technique is given.

3.1 Scanning tunneling microscopy (STM)

The STM was invented in 1981 by G. Binnig and H. Rohrer (IBM researchers) [81], who received the Nobel prize in physics in 1986 for this invention. The most striking property of this kind of microscope is that it provides topographic and electronic structure information of conducting or semiconducting surface with atomic resolution in real space. From figure 3.1, it can seen that the working principle of STM is based on the quantum mechanical tunneling effect, and the measure process consists in placing a metallic tip, which is mounted on a piezoelectric scanner, extremely close (few Å) to the sample surface. Due the fact that the tip-sample distance is very small, the wave function of the charge carriers in the tip and the sample overlap, thus if one applies a bias voltage between the tip and sample, a current flows through the gap. This occurs because the bias voltage shifts the Fermi levels one with respect to the other and electrons can tunnel trough the vacuum barrier [82, 83].

The tunneling junction (tip-gap-sample) can be treated in different approximations in order to calculate the tunneling current. The most used method consist in starting with a tunneling formalism proposed by Bardeen [84] for the study of superconducting tunneling junction, where the tip and sample are treated as separated systems but with a overlap of the wave functions within the separate barrier, and the first order perturbation theory is used to calculate the tunneling current using the Fermi's golden rule [89]. Tersoff and Hamann applied the Bardeen's formalism and showed that the tunneling current

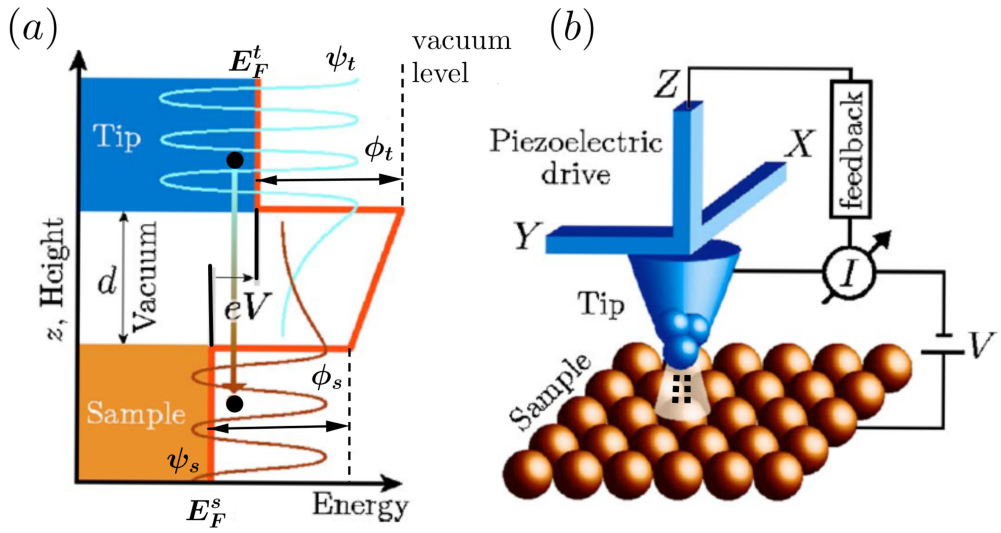

Figure 3.1: The working principle of STM. (a) Tunneling process between the tip and the sample across a barrier of width d and height ϕ (work function). The electron wave functions decay exponentially into vacuum with a small overlap, allowing electrons to tunnel from one electrode to the other. With a positive bias voltage V applied to the sample, electrons tunnel from the tip into unoccupied sample states. (b) Schematic illustration of the STM [83].

produced by electronic transitions from filled sample states into empty tip states or from filled tip states into empty sample states when a bias voltage V is applied between the tip and the sample, is given by [86, 87]:

$$I(V) = \frac{4\pi e}{\hbar} \sum_{n,m} [f(E_n^t - E_F^t) - f(E_m^s - E_F^s)] \, |M_{nm}|^2 \, \delta(E_n^t - E_m^s - eV), \tag{3.1}$$

where $f(E)$ is the Fermi-Dirac distribution, and M_{nm} is the tunneling matrix element (Bardeen's matrix element) that describes the transition probability between tip states ψ_n and sample states ψ_m, with energies E_n^t and E_m^s, respectively. The δ-function shows that only transition between states with the same energy value are allowed (elastic tunneling). Replacing the summation over discrete states in eq. (3.1) by an integration over the density of states (DOS), $\rho(E)$, this can be written as [82, 87]:

$$I(V) = \frac{4\pi e}{\hbar} \int_{-\infty}^{\infty} [f(E_F^s - eV + E) - f(E_F^t + E)] \rho^t(E_F^t - eV + E) \rho^s(E_F^s + E) \, |M|^2 \, dE, \tag{3.2}$$

This is the general equation for the tunneling current, which links the tunneling current to the electronic properties of the tip and the sample described by the DOS. In order to simplify eq. (3.2), a few of standard approximations are used. The first one, is the low-temperature approximation, in which the Fermi-Dirac distribution becomes in a step function and eq. (3.2) yields [82, 87]:

$$I(V) = \frac{4\pi e}{\hbar} \int_0^{eV} \rho^t(E_F^t - eV + E)\rho^s(E_F^s + E)\,|M|^2\,dE, \tag{3.3}$$

On the other hand, the matrix element can be obtained by solving the time-independent Schrödinger equation in the Wentzel-Kramers-Brillouin (WKB) approximation for a trapezoidal potential barrier, such as is shown in the tunneling junction of figure 3.1(a). Thus, the tunneling matrix element $|M|^2$ is replaced by the transmission coefficient, which gives the probability of electrons tunneling through the potential barrier [82, 87, 88]:

$$\mid M \mid^2 \rightarrow T(E,V,z) = \exp\left[-2z\sqrt{\frac{m_e}{\hbar^2}\left(\frac{\phi_t + \phi_s}{2} + \frac{eV}{2} - E\right)}\right], \tag{3.4}$$

For small bias voltage ($eV \ll \phi_s, \phi_t$), the transmission coefficient can be simplified by [82, 87]:

$$T(z) = \exp\left[-2z\sqrt{\frac{m_e}{\hbar^2}\left(\frac{\phi_t + \phi_s}{2}\right)}\right], \tag{3.5}$$

and the tunneling current can be written as:

$$I(V,x,y,z) = \frac{4\pi e^2 V}{\hbar} T(z) \int_0^{eV} \rho^t(E_F^t - eV + E)\rho^s(E_F^s + E, x, y)dE. \tag{3.6}$$

In eq. (3.6) the first factor shows the exponential dependence of the tunneling current on the tip-sample distance, which define the vertical resolution that can be achieved in STM, and the second one shows the dependence on the local density of state (LDOS) of the sample $\rho^s(E_F^s + E, x, y)$ and the DOS of the tip $\rho^t(E_F^t - eV + E)$. The lateral resolution mainly depends on the tip apex geometry and electric orbitals of the scanning tip [89], which confine the tunneling electrons into a narrow channel, offering the unique opportunity to perform real-space imaging down to atomic length scales. Topographic image of a surface can be obtained in STM in two ways [83]:

1. Constant-current mode: in this mode the tip is scanned over the sample surface and a feedback system is used to adjusts the tip height by approaching or retracting the tip to a tip-sample distance at which the tunneling current remains constant (see figure 3.2(a)). A topographic image of the sample surface is formed recording the tip height as a function of the lateral position (x, y).

2. Constant-height mode: in this mode the tip is scanned over the sample surface keeping the tip-sample distance constant (see figure 3.2(b)). The tunneling current as function the lateral position (x, y) is recorded to form the topographic image of the surface. This mode allows fast scanning but is restricted to flat surfaces to avoid collisions between the tip and the sample.

(a) Constant current image **(b) Constant height image**

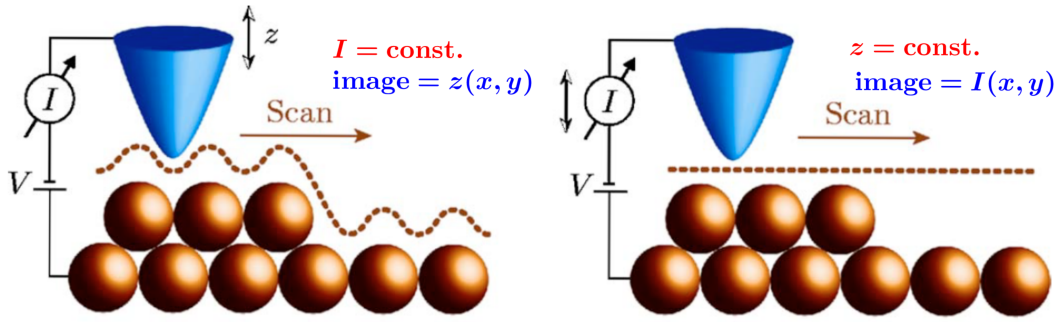

Figure 3.2: STM operating modes [83].

3.1.1 Scanning tunneling spectroscopy (STS)

In STS the dependence of the tunneling current on the LDOS, such as is shown in eq. (3.6), together with the high spatial resolution of STM are used to study the local electronic structure of the sample surface with atomic resolution. If the tunneling current given by eq. (3.6) is differentiated with respect the bias voltage V, the following expression is obtained:

$$\begin{aligned}\frac{dI}{dV} &= \frac{4\pi e^2}{\hbar} T(z) \int_0^{eV} \rho^t(E_F^t - eV + E)\rho^s(E_F^s + E, x, y)dE \\ &+ \frac{4\pi e^2 V}{\hbar} \int_0^{eV} \frac{d\rho^t(E_F^t - eV + E)}{dV} \rho^s(E_F^s + E, x, y)dE,\end{aligned} \tag{3.7}$$

Considering the DOS of the tip at the Fermi level where it can be assumed as a constant, the second term is zero and the equation above becomes:

$$\frac{dI}{dV} \propto T(z)\rho^t(0)\rho^s(eV, x, y). \tag{3.8}$$

For a predefined position (x, y), the tunneling current is a function of the bias voltage V and the tip-sample separation z. In STS, the relation between two of these three parameters is measured while the remanding one is kept constant. Typically, the tunneling current is measured as a function of the bias voltage for a constant tip-sample separation. This allow us to obtain characteristic $I - V$ curves which can be numerically deviated in order to find dI/dV and obtain the LDOS of the sample at the energy eV relative to the Fermi energy of the sample such as is shown by eq. (3.8). The quantity dI/dV is called as *differential conductance*, and it also can be measured directly by using a lock-in amplifier to modulated V. More details about the dI/dV measurements using the lock-in technique can be found in [82, 87].

Due the spatial localization of the tunneling current, STS makes possible the characterization of the electronic properties of individual atoms and molecules in relation

to their structure, bonding and local environment. In tunneling spectroscopy, it is also possible to study both the occupied and the unoccupied states of the sample when the polarity of the bias voltage is changed. On the other hand, STS does not provide chemical information and tip artifacts can strongly influence the spectroscopic data [90, 91].

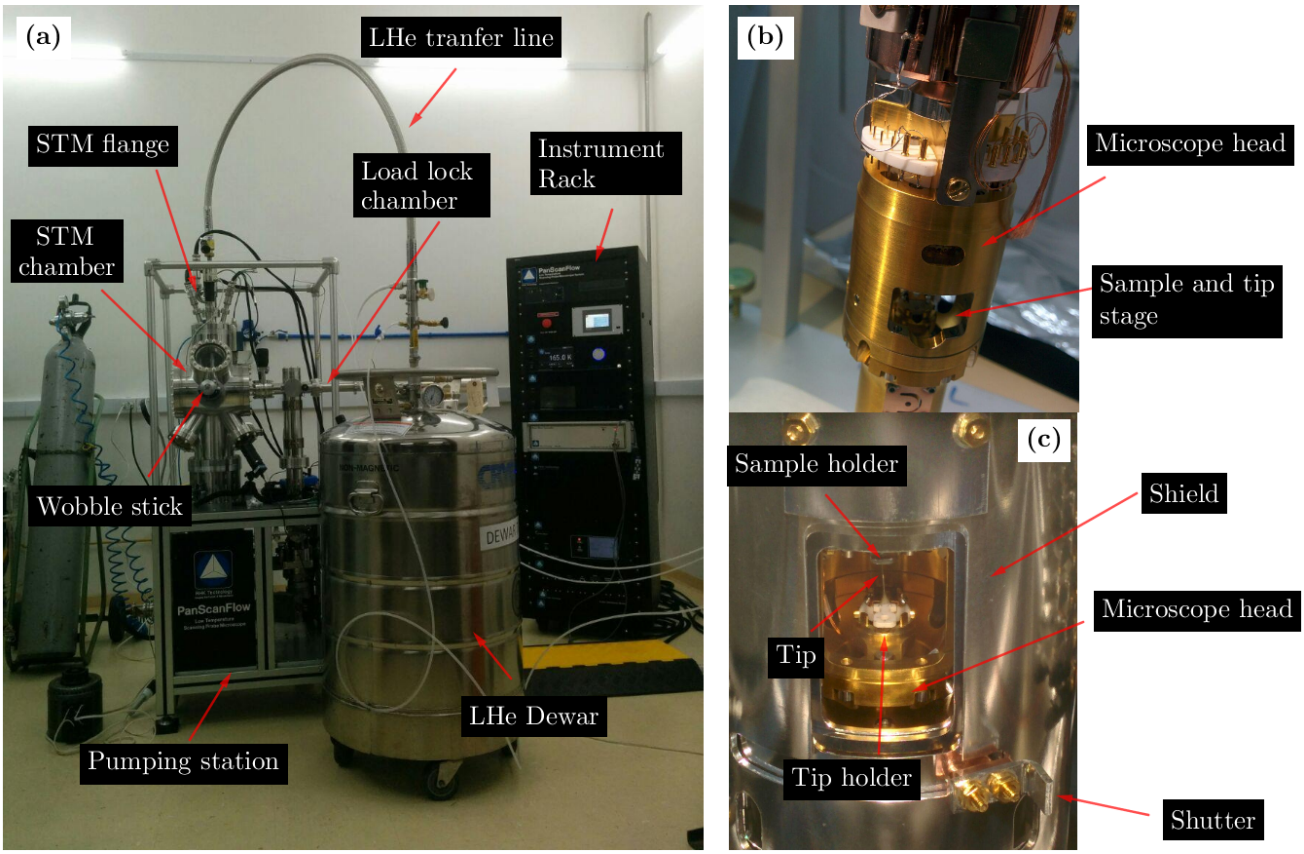

Figure 3.3: (a) Overview of the UHV-LT-STM system. (b) Microscope head. (c) Sample and tip stage.

The STM measurement presented in this work have been obtained using a RHK microscope that works in UHV and low temperature (UHV-LT-STM), see figure 3.3. This STM was installed in our laboratory about four months ago, part of my work was to study the mechanical vibration conditions of the STM laboratory. In appendix A are shown the results of the mechanical vibrations study, which demonstrated that our laboratory meets the NIST vibration isolation criteria for laboratory for nanotechnology [92].

3.2 Atomic force microscopy (AFM)

Five years after of the STM invention, G. Binnig, C. F. Quate, and Ch. Gerbe created the atomic force microscope (AFM) [93], in which the tunneling tip is replaced by a force sensor, making it possible the analysis of conducting and nonconducting samples, like insulators, polymers and biological systems. Such as its name says, the technique uses

the interaction force between a sharp tip and the sample to form an image. The type of image that can be obtained depends on the type of interaction (e.g. electrostatic, magnetic, Van der Waals, etc.) that is measured by the probe.

The working principle of AFM is shown in figure 3.4 and consists in measure the interaction force between the probe and the sample surface using an elastic cantilever with a sharp tip in the end as force sensor. The tip-sample interaction leads to an attraction or repulsion of the tip depending on the tip-sample distance, which results in a deflection of the cantilever. This cantilever deflection is measured by using a laser beam that is directed on the cantilever and reflected to a photodiode. The tip-sample interaction can be explained qualitatively considering the curve force shown in figure 3.5, where three regimes are distinguished: (i) if the tip is far away from the sample surface the force between tip and sample is negligible, (ii) for closer distance an attractive force between tip and sample occurs, and (iii) for very small distance a strong repulsive force between tip and sample occurs [82, 94, 95]. These regimes in the tip-sample force allow to define, in general, two AFM operation modes:

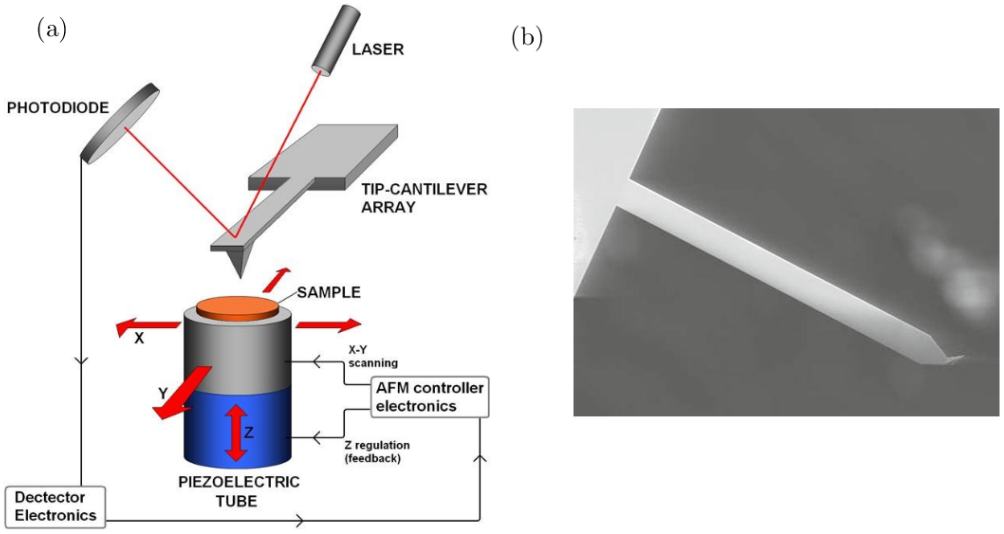

Figure 3.4: Working principle of AFM. (a) The sample is mounted on the piezoelectric scanner and the force between the tip and the sample surface is monitoried by measuring the cantilever deflection by means an optical system constituted by a laser and photodiode, figure taken from [94]. (b) SEM image of a silicon cantilever used in AFM with a length of 450 μm [82].

1. Static (contact) mode: in this mode the cantilever acts as a spring and its deflection is proportional to the tip-sample force, $s = F/k$, where k is the cantilever spring constant. The feedback system keeps the cantilever deflection constant (tip-sample force constant) by adjusting the tip-sample distance through the piezoelectric scanner. By scanning the tip across the sample surface and monitoring the z-movement of the piezoelectric, a topographic image of the sample surface is obtained. This operating mode is performed in the repulsive regimen (see figure 3.5) and usually the tip is in contact with the sample, then the main problem of this mode is that the sample can be damaged by the tip.

2. Dynamic (non-contact) mode: in this case, the AFM is operated in the attractive part of the tip-sample interaction and the cantilever is forced to oscillate close to its free

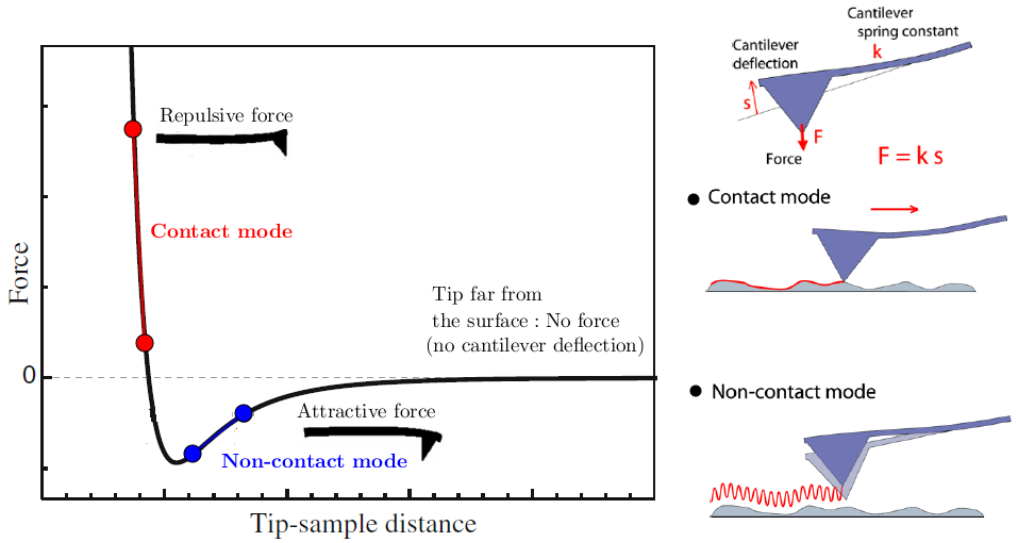

Figure 3.5: Qualitative behavior of the force between tip and sample and the AFM operation modes. Adapted from [82, 95].

resonance frequency. When the AFM tip approaches the surface, the interaction between tip and sample changes the resonance frequency of the cantilever and the amplitude oscillation or the frequency oscillation can be used as feedback signal to generate the sample image. Hence, the dynamic AFM mode can be performed in two ways: the amplitude modulated AFM (AM-AFM), and the frequency modulated AFM (FM-AFM). In AM-AFM, the amplitude oscillation of the cantilever is fixed, while frequency shift induced by the tip-sample force is measured. Alternatively, in FM-AFM, the frequency oscillation of the cantilever is kept constant and changes in the amplitude are measured [82, 96].

All the AFM images shown in this work were taken using the Nanosurf EasyScan2 Flex AFM microscope of LAMULT (Laboratório Multiusuários do IFGW), operated in the amplitude modulated mode.

3.3 Raman spectroscopy

When light interacts with matter different optical process can occur, among them the light scattering. When the light is elastically scattered by the medium the process is known as *Rayleigh scattering*. In Raman spectroscopy, the light is inelastically scattered by the sample and the difference in frequency between incident light and scattered light is associated with the excitation of the optical modes of lattice vibrations in the sample. Raman spectroscopy is an experimental technique widely used for the study and the characterization of semiconductor materials because give us information about the crystal quality, lattice dynamics, and the composition of the samples in a nondestructive and contactless way. In the following, a simple introduction to the basic concepts of Raman spectroscopy is given, a more detailed description of the technique can be found in [44, 97, 98].

3.3.1 Raman scattering

In the Raman process, an incident photon with energy $E_i = \hbar\omega_i = E_{\text{laser}}$ and momentum $\vec{k}_i = \vec{k}_{\text{laser}}$ reaches the sample and is scattered, resulting in a photon with a different energy $E_s = \hbar\omega_s$ and momentum $\vec{k}_s$. The energy and momentum conservation says that:

$$E_s = E_i \pm E_q, \text{ and } \quad \vec{k}_s = \vec{k}_i \pm \vec{q}, \tag{3.9}$$

where $E_q = \hbar\Omega_q$ and $\vec{q}$ are the energy and the momentum of the phonon that is created or annihilated during the inelastic scattering event. The vibrational modes (phonons) excited in Raman scattering are called normal modes and are related to the chemical and structural properties of materials. Since every material has a unique characteristic set of normal modes, Raman spectroscopy is used to probe material properties in detail and to provide an accurate characterization of certain Raman active modes in specific materials [97].

Light scattering can be described using the classical electrodynamic theory. For this, it must be considered the fact that in a dielectric medium with electric susceptibility $\overleftrightarrow{\chi}$, an external electromagnetic wave with electric field vector $\vec{E}(\vec{r},t) = \vec{E}(\vec{k}_i,\omega_i)\cos(\vec{k}_i\cdot\vec{r}-\omega_i t)$, will induce a polarization $\vec{P}(\vec{r},t)$ given by [44]:

$$\vec{P}(\vec{r},t) = \overleftrightarrow{\chi}(\vec{k}_i,\omega_i)\vec{E}(\vec{k}_i,\omega_i)\cos(\vec{k}_i\cdot\vec{r}-\omega_i t) = \vec{P}(\vec{k}_i,\omega_i)\cos(\vec{k}_i\cdot\vec{r}-\omega_i t), \tag{3.10}$$

On the other hand, it is known that if the medium is at a finite temperature, some atomic vibrations are thermally excited. The atomic displacement for the normal modes of the atomic vibrations in a solid (phonons) can be written as:

$$\vec{Q}(\vec{r},t) = \vec{Q}(\vec{q},\Omega_q)\cos(\vec{q}\cdot\vec{r}-\Omega_q t), \tag{3.11}$$

These atomic vibrations change with the time, therefore $\overleftrightarrow{\chi}$ will be modified. Assuming that the amplitude of the atomic vibrations at room temperature are smaller than the lattice constant, the dependence of $\overleftrightarrow{\chi}$ on the atomic vibrations can be found by expanding $\overleftrightarrow{\chi}$ as a Taylor series in $\vec{Q}(\vec{r},t)$, this is:

$$\overleftrightarrow{\chi}(\vec{k}_i,\omega_i,\vec{Q}) = \overleftrightarrow{\chi}_0(\vec{k}_i,\omega_i) + \left[\frac{\partial\overleftrightarrow{\chi}}{\partial\vec{Q}}\right]_0 \vec{Q}(\vec{r},t) + \cdots \tag{3.12}$$

where χ_0 is the electric susceptibility of the medium without fluctuations, and the second term represents an oscillating susceptibility induced by the effect of the lattice wave vector $\vec{Q}(\vec{r},t)$. Now, the polarization induced in the medium can be written in the first order approximation as:

$$\begin{aligned}\vec{P}(\vec{r},t,\vec{Q}) &= \left\{\overleftrightarrow{\chi}_0(\vec{k}_i,\omega_i) + \left[\frac{\partial\overleftrightarrow{\chi}}{\partial\vec{Q}}\right]_0 \vec{Q}(\vec{r},t)\right\}\vec{E}(\vec{k}_i,\omega_i)\cos(\vec{k}_i\cdot\vec{r}-\omega_i t) \\ &= \vec{P}_{\text{Rayleigh}}(\vec{r},t) + \vec{P}_{\text{Raman}}(\vec{r},t,\vec{Q}),\end{aligned} \tag{3.13}$$

where

$$\vec{P}_{\text{Rayleigh}}(\vec{r},t) = \overleftrightarrow{\chi}_0(\vec{k}_i,\omega_i)\vec{E}(\vec{k}_i,\omega_i)\cos(\vec{k}_i\cdot\vec{r}-\omega_i t), \tag{3.14}$$

and

$$\begin{aligned}\vec{P}_{\text{Raman}}(\vec{r},t,\vec{Q}) &= \left[\frac{\partial\overleftrightarrow{\chi}}{\partial\vec{Q}}\right]_0 \vec{Q}(\vec{r},t)\vec{E}(\vec{k}_i,\omega_i)\cos(\vec{k}_i\cdot\vec{r}-\omega_i t)\\ &= \left[\frac{\partial\overleftrightarrow{\chi}}{\partial\vec{Q}}\right]_0 \vec{Q}(\vec{q},\Omega_q)\cos(\vec{q}\cdot\vec{r}-\Omega_q t)\vec{E}(\vec{k}_i,\omega_i)\cos(\vec{k}_i\cdot\vec{r}-\omega_i t)\\ &= \frac{1}{2}\left[\frac{\partial\overleftrightarrow{\chi}}{\partial\vec{Q}}\right]_0 \vec{Q}(\vec{q},\Omega_q)\vec{E}(\vec{k}_i,\omega_i)\times\\ &\{\cos[(\vec{k}_i+\vec{q})\cdot\vec{r}-(\omega_i+\Omega_q)t]+\cos[(\vec{k}_i-\vec{q})\cdot\vec{r}-(\omega_i-\Omega_q)t]\}.\end{aligned} \tag{3.15}$$

From eq. (3.13) can be seen that the polarization induced in the medium by the electric field of the incident electromagnetic radiation has Rayleigh and Raman contributions. The Rayleigh contribution given by eq. (3.14) is the part of the polarization that vibrates with the same frequency ω_i of the incident radiation, producing the elastic light scattering known as Rayleigh scattering. From the Raman contribution given by eq. (3.15), it can be seen that the polarization is modified by the lattice atomic vibration (phonons) and the light suffers inelastic scattering. Eq. (3.15) also shows that there are two components in the Raman polarization. The *Stokes* shifted component with wavevector $k_{\text{stoke}} = (\vec{k_i}-\vec{q})$ and frequency $\omega_{\text{stokes}} = (\omega_i-\Omega_q)$, and the *Anti-Stokes* shifted component with wavevector $k_{\text{Anti-Stoke}} = (\vec{k_i}+\vec{q})$ and frequency $\omega_{\text{Anti-Stokes}} = (\omega_i+\Omega_q)$. The radiation produced by these two polarization components in the Raman polarization are known as Stokes scattered and Anti-Stokes scattered light, respectively. Since the frequency of the phonon involved in the Raman process corresponds to the difference between the incident photon frequency and the scattered photon frequency, this value is called as Raman shift. Figure 3.6 shows a typical Raman spectrum which consist in a plot of the intensity of the Raman radiation versus the Raman shift.

It is important to notice that both frequency and wavevector are conserved in the above scattering processes. As a consequence of the wavevector conservation, the wavevector $|\vec{q}|$ of phonons studied by one-phonon Raman scattering must be smaller than twice the photon wavevector [1]. Assuming that visible wavelength is used to carry out Raman measurements, $|\vec{q}|$ is of the order of 10^8 m^{-1}, this value is 100 times smaller than the size of the Brillouin zone ($\sim 10^{10}$ m^{-1}). Hence, one-phonon Raman scattering is only able to probe phonons at the center of the Brillouin zone ($|\vec{q}| \to 0$).

The intensity of the scattering radiation can be calculated from the time-average power radiated by the induced polarization $\vec{P}_{\text{Raman}}(\vec{r},t,\vec{Q})$ into unit solid angle. Since the Stokes and Anti-Stokes polarization components differ only in their frequencies and wavevectors, only Stokes scattering will be considered. The intensity depends on the polarization of

[1] The maximum phonon frequency in a typical crystal is about 10^{12}-10^{13} Hz. This is almost two order of magnitude smaller that the frequency of a photon in the visible range. Eq. (3.9) shows that the maximum frequency shift for the photon will be around 1%. In this case the following aprroximation can be made: $|\vec{k}_s| \approx |\vec{k}_i| = (n\omega)/c$, where n is the refractive index, c the light velocity, and ω the light frequency. The maximum value of $|\vec{q}|$ occur for back-scattering geometry, for which $|\vec{q}| \approx |\vec{k}_s - (-\vec{k}_i)| \approx (2n\omega)/c$ [45].

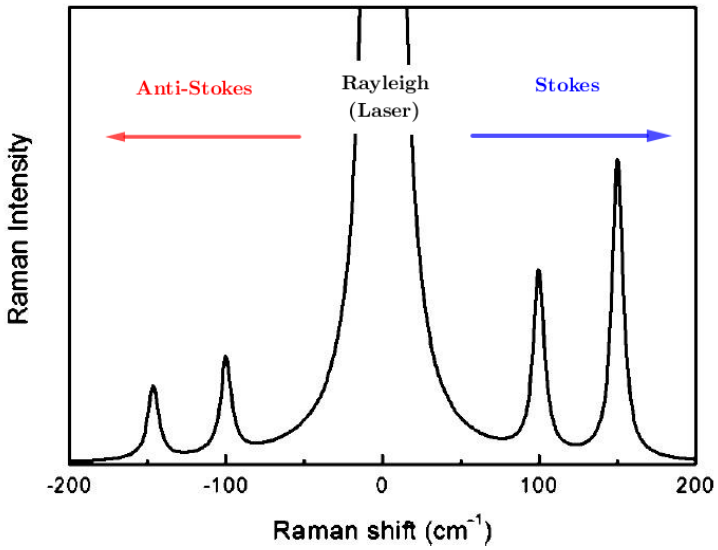

Figure 3.6: Schematic Raman spectrum showing the Rayleigh peak at 0 cm^{-1}, and the Raman Stokes and Anti-Stokes peaks. Adapted form [97].

the scattered radiation. If this polarization is given by the vector $\hat{e}_s$, the intensity can by expressed as:

$$I_s \propto \mid \vec{P}_{\text{Raman}} \cdot \hat{e}_s \mid^2 = \left| \left[\frac{\partial \overleftrightarrow{\chi}}{\partial \vec{Q}} \right]_0 \vec{Q}(\vec{r},t)\vec{E}(\vec{k}_i,\omega_i) \cdot \hat{e}_s \right|^2, \tag{3.16}$$

If the polarization of the incident radiation is given by $\hat{e}_i$, the intensity of the scattered radiation can be written as:

$$I_s \propto \left| \left[\frac{\partial \overleftrightarrow{\chi}}{\partial \vec{Q}} \right]_0 \vec{Q}(\vec{r},t)\hat{e}_i \cdot \hat{e}_s \right|^2 = \mid \hat{e}_i \cdot \overleftrightarrow{R}\, \hat{e}_s \mid^2, \tag{3.17}$$

where

$$\overleftrightarrow{R} = \left[\frac{\partial \overleftrightarrow{\chi}}{\partial \vec{Q}} \right]_0 \vec{Q}(\vec{r},t). \tag{3.18}$$

$\overleftrightarrow{R}$ is known as the *Raman tensor*. Eq. (3.17) says us that the minimum condition to observe Stokes scattering by one phonon is that at least one component of $\overleftrightarrow{R}$ must be different of zero. Measurements of the dependence of the scattering intensity on the incident and scattered polarizations give information about the elements of the Raman tensor, and the symmetry of the vibrational modes can by investigated.

The classical description of the light scattering allows to know the frequencies and the selections rules of Raman scattering. However, according with this treatment the Raman intensity of the Stokes and Anti-Stokes components are equals, which is not correct. For a more appropriate description of the Raman intensities, a quantum mechanical treatment must be adopted, in which the electron-photon and electron-phonon interaction are taken into account to describe the scattering process [44].

The Raman measurements of this work were obtained using Raman microscopy, for which a Raman spectrometer is integrated with an optical microscopy. This allows us to acquire Raman spectra of microscopic samples or microscopic areas of larger samples. Some Raman measurements were taken using the Micro Raman XploRA Horiba spectrometer of LAMULT, and other measurements were taken using the home built micro-Raman setup of the "Group of Optical Properties" (GPO) of the IFGW. A schematic diagram of the micro-Raman setup of GPO is shown in figure 3.7, in which a set of lens, mirrors (M) and beam splitting (BS) are used to excite the sample with a laser of 488 nm through a 50x objective lens with numerical aperture NA=0.55. The laser spot-size which the sample is excited is about 1 μm in diameter. The light emitted by the sample is collected by mean of the objective lens again and directed towards an optical fiber that carries the light to a spectrometer coupled to a cooled CCD detector. A white light lamp is used to shine the sample and to obtain an image using a CCD camera so that regions of interest can be found. The sample is mounted on a motorized stage that is computer controller. To measure at low temperature, a helium cryostat is used.

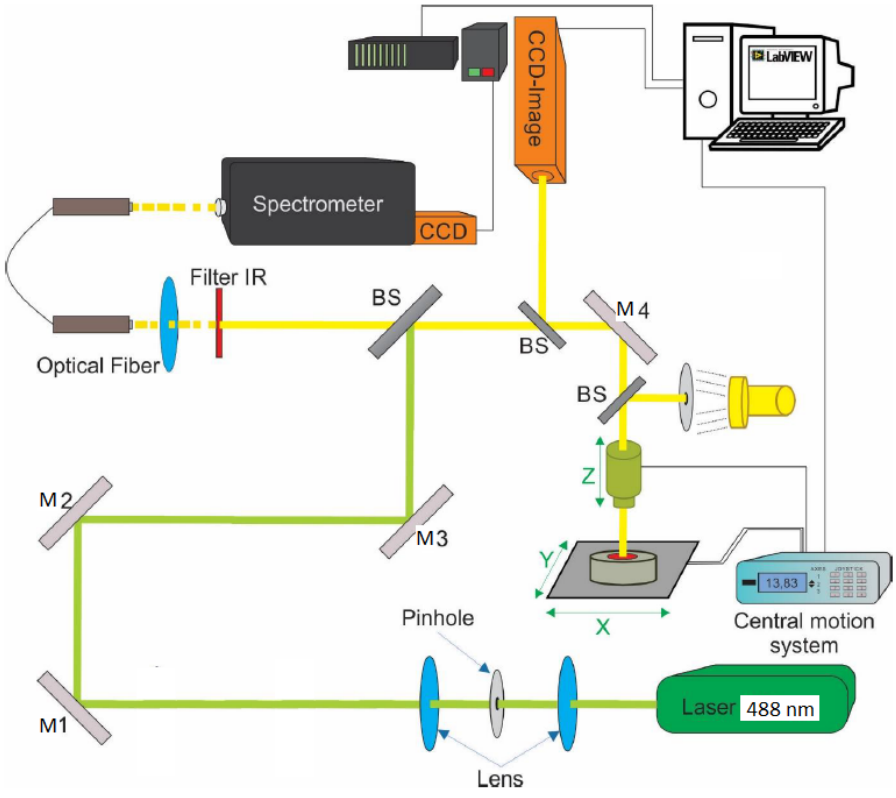

Figure 3.7: Schematic diagram of the micro-Raman/PL setup. Adapted from [99].

3.4 Photoluminescence spectroscopy (PL)

Photoluminescence is a powerful technique that allows to investigate the optical and electronic properties of materials. The technique consists in excite the sample by light exposure and analyse the light emitted by the sample after the excitation process.

In semiconductors, electrons in the valence band (VB) are excited to the conduction band (CB) by the absorption of the incident photon energy, the subsequent radiative recombination of electron-hole pairs and the resulting luminescence spectrum provide information about the band gap energy, impurity, excitonic and defect states. The recombination processes more frequently observed in a PL spectrum of semiconductors are shown in figure 3.8[100].

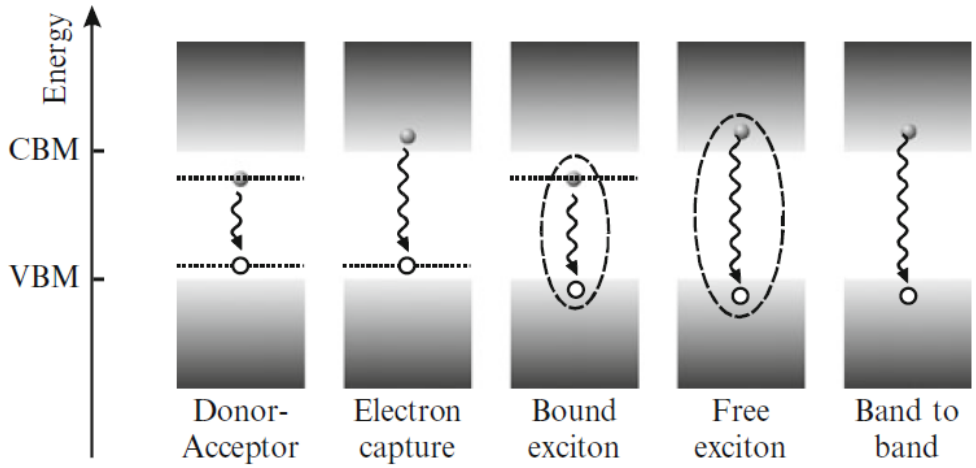

Figure 3.8: Main recombination process observe in PL. The shaded areas indicate valence and conduction band, the horizontal dotted lines mark the energy position of impurity or defect states. Electron (holes) are indicated by dark-shaded (hollow) dots. Undulated arrows indicate radiative recombination. Dashed curves highlight the coulomb interaction [100].

In an ideal semiconductor, with no energy levels inside the forbidden gap, electrons form the bottom of the CB recombine with holes on the top of the VB. The energy of the photon emitted during this *band-to-band* transition corresponds to the band gap energy of the material. In some materials, the Coulomb interaction between electrons and holes involved in the transition leads to the formation of bound electron-hole pairs called *excitons*. In this case, the dominant features in the PL spectrum is associated with the recombination of *free excitons*, and the energy of the photon emitted is that of the excitonic ground state, which corresponds to the energy band gap minus the exciton binding energy. Beside these intrinsic transitions, a PL spectrum can show features related to the presence of *impurities* or *defects*, whose incorporation in the crystal structure is associated with energy levels within the forbidden gap, such as is shown in figure 3.9 [100].

All the micro-PL measurements shown in this work were taken in part using the Micro Raman XploRA Horiba spectrometer of LAMULT (Laboratório Multiusuários do IFGW), and in part using the micro-PL setup of the "Group of Optical Properties" (GPO) of the IFGW.

3.5 STM-induced luminescence (STML) and point defects in 2D materials

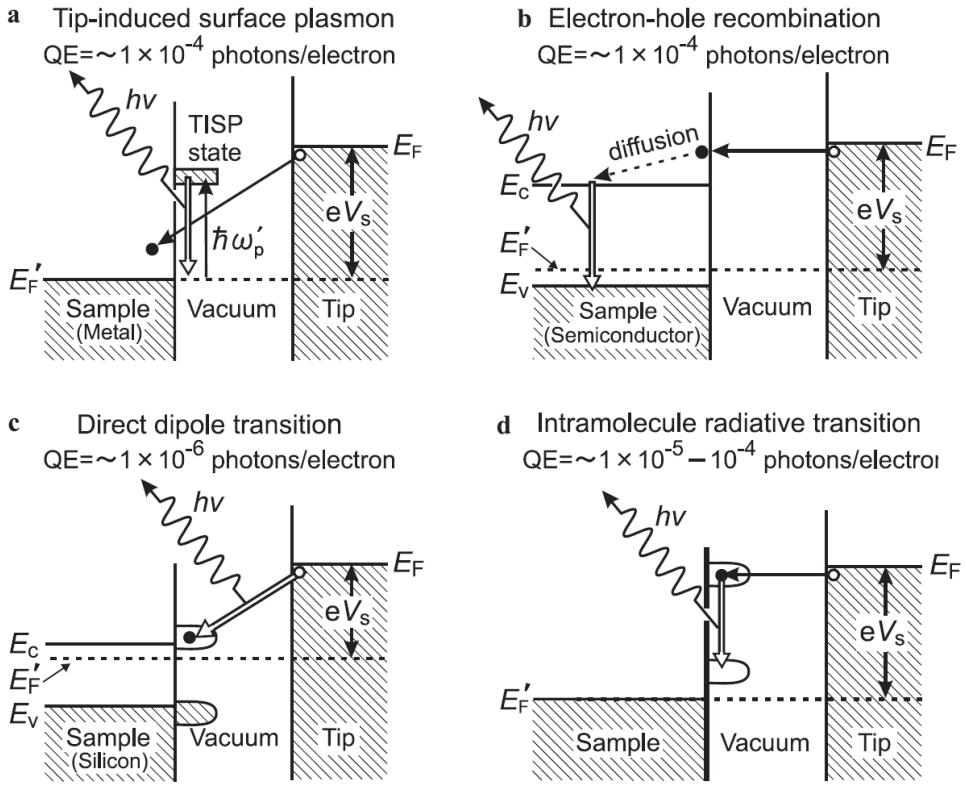

Figure 3.9: Schematic illustration of mechanisms of STML for (a) noble-metal surface, (b) III-V semiconductors, (c) Si(001) surface, (d) organic molecules absorbed on sample surface. Adapted from [107].

The light emission from a tunneling junction in STM was first reported by Gimzewski, *et al.* in samples of polycrystalline tantalum and Si(111)7×7 [101]. This lead to the development of a new experimental technique commonly known as STM-induced luminescence (STML) [19] or scanning tunneling luminescence (STL) [102] in which the STM tip is used to inject low-energy charge carries in the sample an to excite local photon emission, allowing to study the optical properties with the spatial resolution of STM and overcomes the diffraction limit imposed in conventional optical spectroscopy techniques [19, 102]. The resolution in STML is mainly limited by the diffusion length of the charge carriers [102]. Along the last decades, STML has been employed to investigate a broad variety of system like semiconductors and semiconductor nanostructures [96, 103], molecules [96, 104], metallic surfaces and metallic nanoparticles [105, 106]. All the experimental results reported so far are explained in terms of the light emission mechanisms illustrated in figure 3.9. The mechanism in figure 3.9(a) shows that the inelastic tunneling from a metallic tip into a metallic surface can lead to the radiative decay of a tip-induced surface plasmons (TISP). These are localized charges oscillation waves between the tip and sample caused by the close proximity of the tip to the sample which generates a strong electric field in the tunneling cavity by applying a bias voltage.

TISP decay radiatively with a quantum efficiency (QE) of 1×10^{-4} photons/electron and their optical spectra show characteristic peaks in the energy corresponding to the resonance energy of plasmon in the visible spectra range [107]. In the case of semiconducting samples, the photon emission is observed as a consequence of the radiative recombination of the minority carriers from the tip and the majority carriers form the sample, such is illustrated in figure 3.9(b). This has been intensively employed to investigated the local optical properties of III-V semiconductors where a QE of the order of 10^{-4} photons/electron has been observed [107]. Figure 3.9(c) shows the STML mechanism observed in Si(001), which is an indirect band-gap semiconductor where the electron-hole recombination is forbidden and the photon emission is due to radiative direct transitions between surface state of the tip and surface state of the sample (dangling bond). In this system a QE of 1×10^{-6} photons/electron has been found and the energy of the light emitted by the sample correspond to the energy difference of the two energy levels [107]. The photon emission process from individual organic molecules is shown in figure 3.9(d), where it can be seen that electrons tunneling from the tip can induce the radiative direct transitions between two orbital of the molecule with a QE of the order of $\times10^{-4} - \times10^{-5}$ photons/electron [107]. In this type of system the luminescence is observed if the molecule is decoupled from the metallic substrate by a thin insulator, which still allows tunneling, to reduce the molecule-metal interaction and to avoid the excitation of surface plasmons. The insulating layer can be a thin NaCl layer or an oxide film [96, 104, 107].

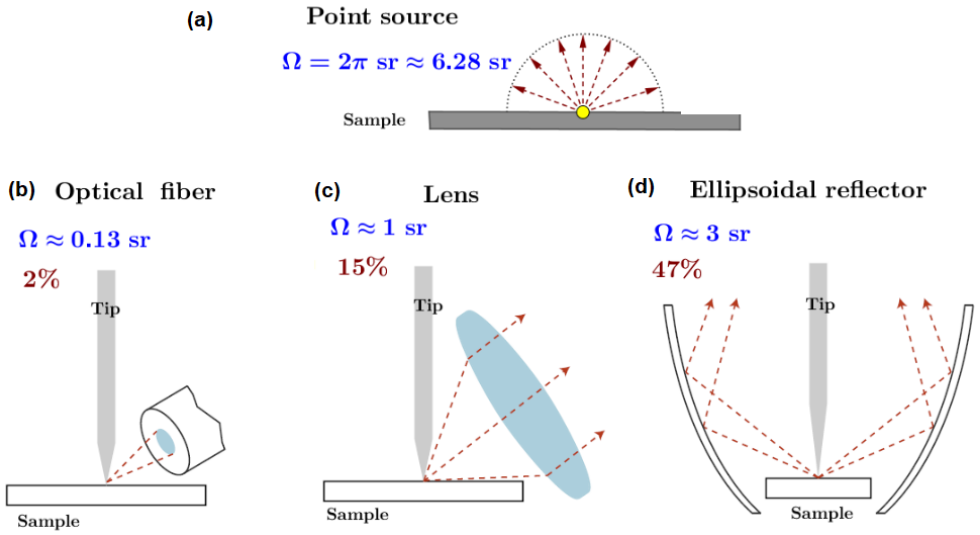

Figure 3.10: Different approach for collecting photons emitted from the STM tunneling junction. (a) Optical fiber, (b) lens, and (d) parabolic reflector. Adapted from [108].

To carry out STML experiments, a scanning tunneling microscope must be coupled to light detection system. Figure 3.10 shows some configurations to light detection typically used in STML setups. As the light emitted in the tunneling junction can be considered to originated from a point source emitting photons into the hemisphere above the sample, such is shown in figure 3.10(a), a large collection solid angled would be ideal to ensure efficient photon detection. Figure 3.10(b) shows an approach used in experiments under ambient conditions, which consists in placing an optical fiber close to the tunneling

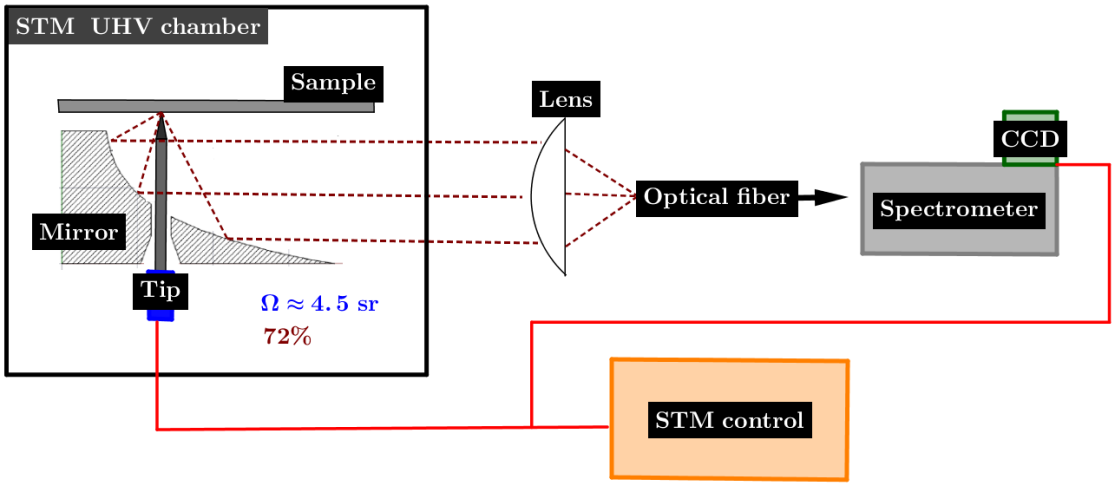

Figure 3.11: Schematic diagram of our STML experimental setup. Our LT-UHV-STM will be coupled to an efficient light detection system based on the used of a parabolic reflector.

junctions where about 2% of the light emitted from the sample is collected. In UHV, lens, see figure 3.10(c), or ellipsoidal reflector, see figure 3.10(d), have been used closed to the tunneling junction to focus the emitted light to a detector or to a optical fiber outside the vacuum chamber. In this way, detection efficiency of 15% and 47% has been achieved for lens and ellipsoidal reflector, respectively [108]. The approach adopted for our STML setup is schematically illustrated in figure 3.11, which consists in a parabolic mirror to collect the light emitted by the sample and a lens to focus the light into an optical fiber outside the STM UHV chamber. The optical fiber carries the light until a spectrometer with a CCD detector where the luminescent spectrum is acquired. This experimental system is based on patented solution for high collection efficiency in cathodoluminescence experiment with transmission electron microscope (TEM), where the use of a parabolic reflector allows to increase the detection efficiency up to 72% [18, 109, 110].

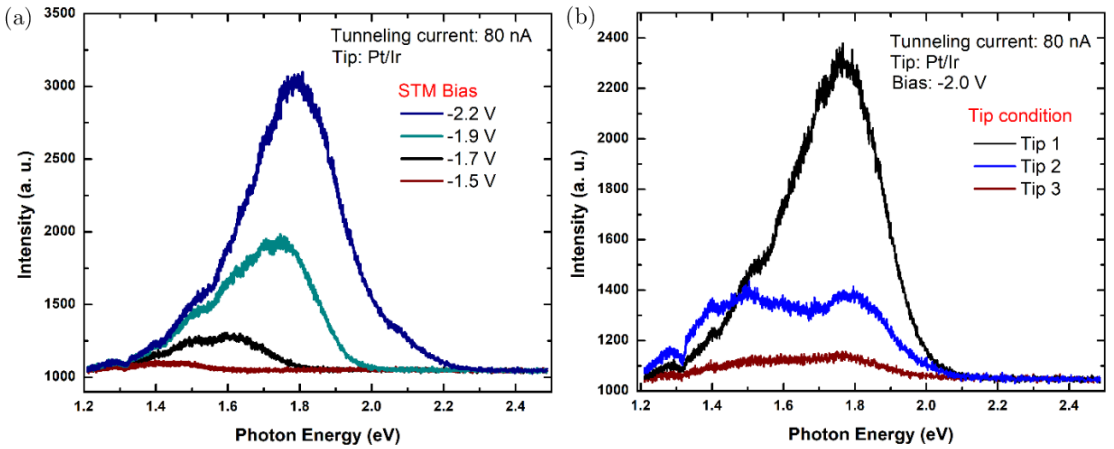

Figure 3.12: First STML results obtained in a Silver nanoparticles sample at room temperature. (a) STML spectrum taken at different tunneling bias. (b) STML spectrum for three different STM tip conditions.

Our STML setup already has been used to observe the TIPS emission in a silver nanoparticles sample. Part of our firts results are shown in figure 3.12. These STML spectra were acquired using a Pt-Ir tip in an fixed position on the sample and with a constant tunneling current of 80 nA. In figure 3.12(a) it can be seen STML spectra taken with different bias, observing that exist a threshold energy for which luminescence occurs and this depends on the applied bias voltage. TISPs are coupled tip-sample surface plasmons, so the shape of the STML spectrum depends strongly on STM tip conditions. It is know that the STM tip conditions can change during measurements, this leads to observe different STML spectrum even using the same tunneling parameters, such as is shown in figure 3.12(b).

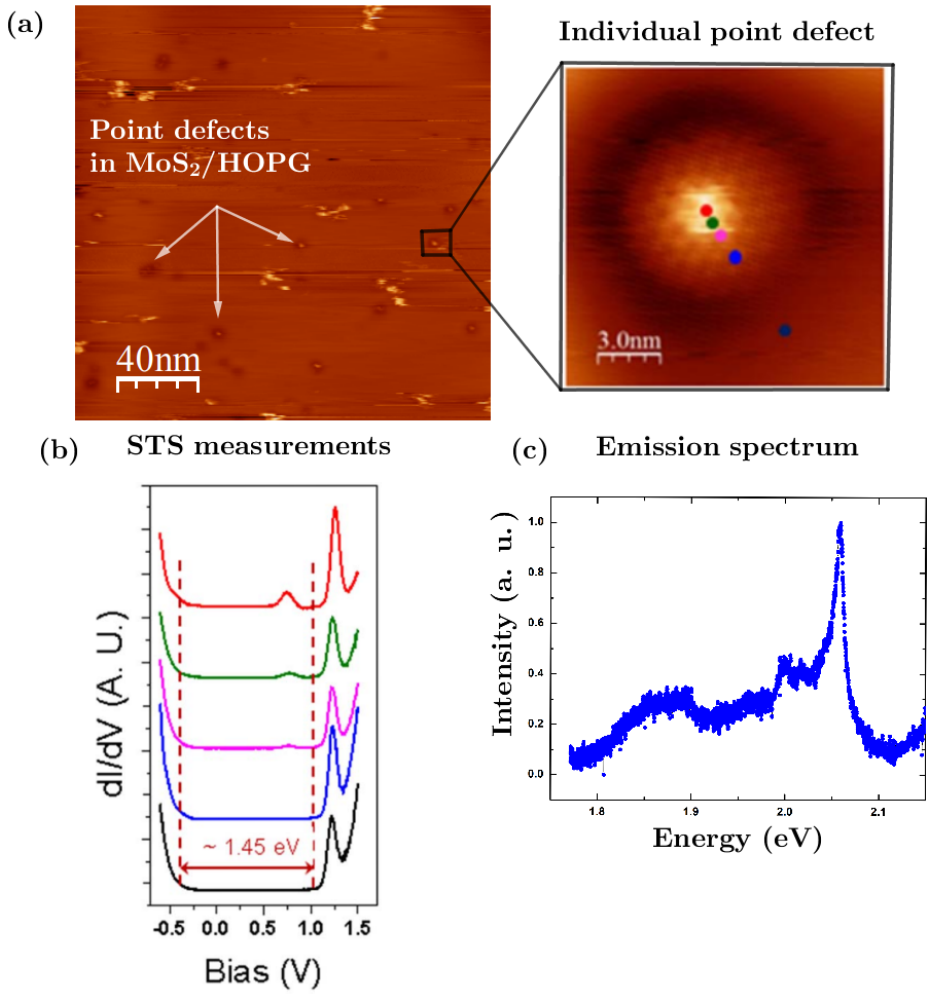

Figure 3.13: Illustration of the STML measurements of point defects in 2D materials. (a) STM image of MoS_2 mechanically exfoliated on HOPG and the observation of point defects, and STM image of an individual point defects. (b) Investigation of the point defect electronic levels by STS measurements. (c) Example of an emission spectrum expected to be observed by STML. (The (a) and (b) image where taken from [111]).

Figure 3.13 shows an example of the type of measurements that are being planed in our laboratory to investigate the structural, electronic and optical properties of individual

point defects in 2D materials like TMDs and h-BN. The STM will be used to obtain images of individual point defects such as shown in figure 3.13(a). The defects electronic levels will be studied locally by STS measurements. Figure 3.13(b) show STS spectra taken in different positions around the individual point defects shown figure 3.13(a), where it can be seen that the STS curve taken in the center of the defect, shows an additional peak within the band-gap close to the valence band which is an indication that this point defects might be caused by p-type impurities in the sample [111]. Making use of the STML system described in figure 3.12, it would be also possible to obtain the emission spectrum related to the point defect. By doing such combined experiments (STM, STS, and STML), a direct correlation could be established among structural, electronic and optical properties.

4 Results and discussion

4.1 Preparation and characterization of WSe_2 monolayer

In the beginning of this work, flakes of WSe_2 mechanically exfoliated by the adhesive tape method were deposited on silicon (Si) substrate with native oxide. Figure 4.1 shows an optical image of that sample where it can be seen that due to the poor optical contrast, it is not possible to identify in an easy way flakes thinner enough like few-layer or monolayer. However, the flakes labeled as 1, 2, and 3, seem to be thinner than bulk flake, so to explore the morphology and thickness of these flakes, AFM topographic images were taken. Figure 4.2 shows that the bulk flake was used as a reference to found the region to be scanned and figure 4.3 shows the AFM image and height profile of each individual flake. All the AFM image were processed using the *Gwyddion* software [112]. From the height profiles in figure 4.3 the thickness of each flake can be estimated, being of approximately 4.4 nm, 7.0 nm, and 10.0 nm for flake 1, 2 and 3, respectively. Taking into account that one monolayer of WSe_2 has a thickness of 0.7-0.9 nm [53, 113], the AFM results say us that the flake 1 is conformed by 5 layers, flake 2 by 8 layers, and flake 3 by 11 layers of WSe_2, which means that these flakes can be considered as few-layer of WSe_2. Our interest is study the properties of monolayer, for this, it is obvious that the substrate must be modified or changed in order to get the best optical contrast in the image to observe monolayer and continue with the sample characterization employing optical spectroscopy techniques. In the literature, it was found that the most appropriated substrate for our purpose is silicon dioxide (SiO_2/Si) with 300 nm of thickness [114], with this in mind, a Si wafer was oxidized by the thermal wet oxidation method which is described in appendix B. To the sample preparation, substrates of SiO_2/Si of 300 nm with dimensions of 5mm×5mm were cut from the wafer and washed by processes of ultrasonic cleaner in acetone, isopropanol, and deionized water for 15 minutes in each one. Nitrogen gas was used to dry the substrates and avoid the formation spots due to the evaporation of water.

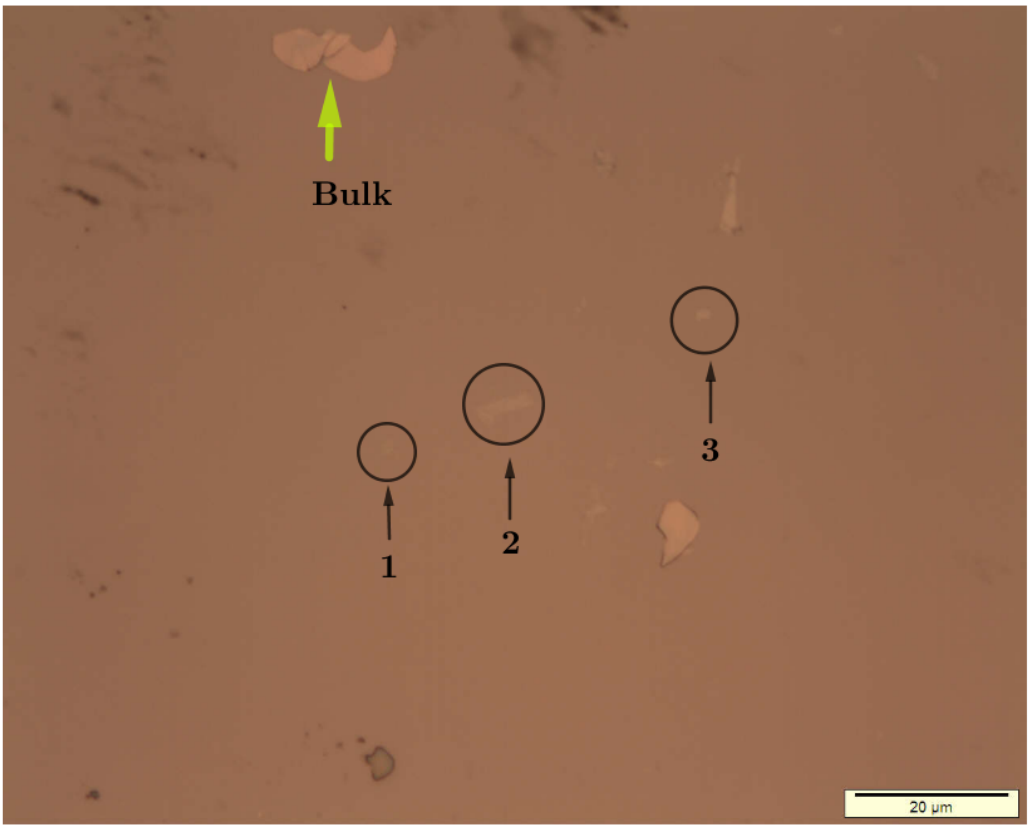

Figure 4.1: Optical image of WSe_2 on Si substrate with native oxide.

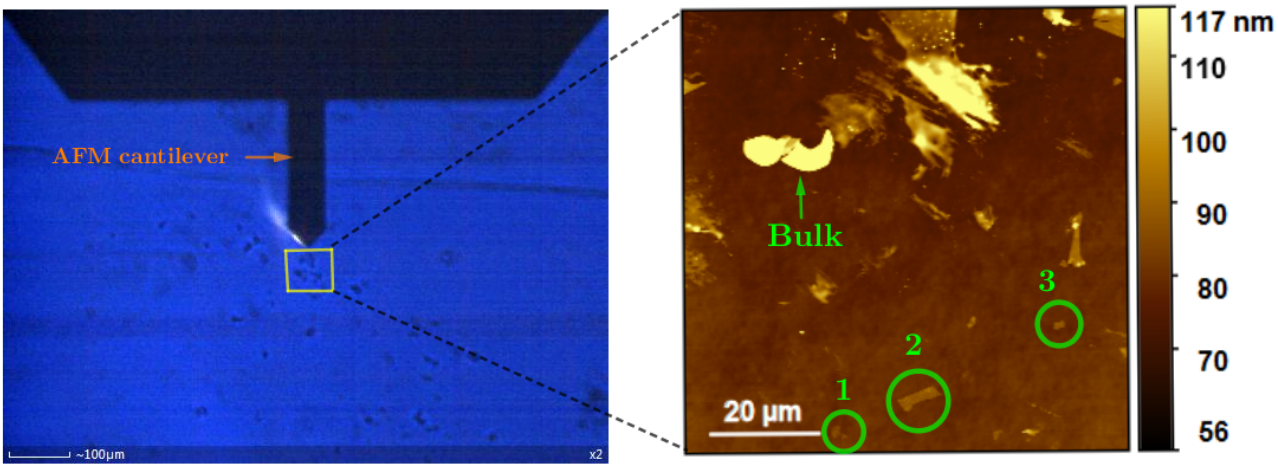

Figure 4.2: AFM image of WSe_2 flakes on Si.

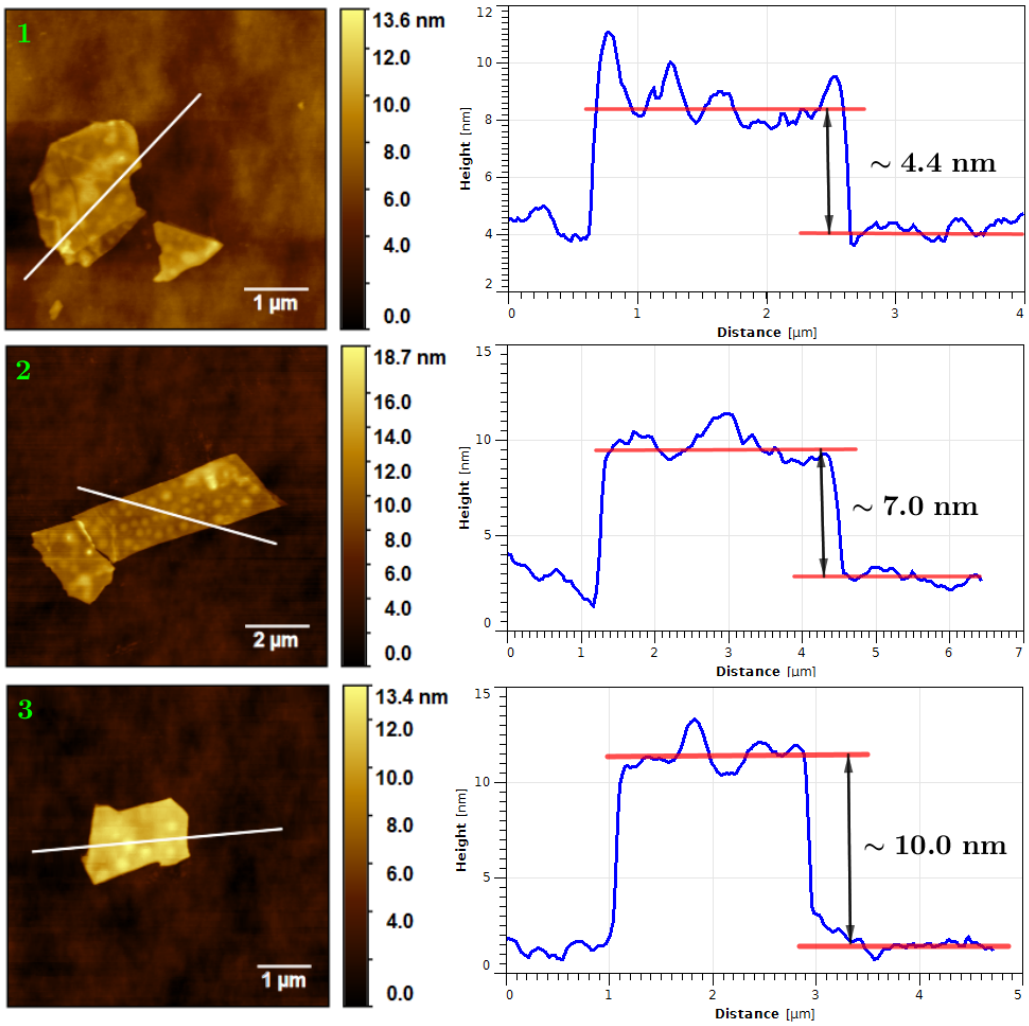

Figure 4.3: AFM image and height profile of individual WSe_2 flakes.

In figure 4.4 are shown optical images of WSe_2 flakes mechanically exfoliated on SiO_2/Si 300 nm. It can be noted that the optical contrast was improved significatively due to the interference effects of multiple reflections of light in the interfaces air/sample/SiO_2/Si, which make possible the identification of WSe_2 monolayer by optical microscopy such as is shown in figure 4.4(a) and (b). A big flake of about 60 μm of size is shown in figure 4.4(a), and at the edge of this flake a region with few-layer and monolayer was found. On the other hand, in figure 4.4(b) is shown an isolated monolayer of about 8 μm. The heterogeneity of the first sample results so interesting because allow us to study and compare the optical behavior of few-layer and monolayer. In figure 4.5 are shown some results of the morphological characterization of this sample. Figure 4.5(a)-(b) show the AFM image of the region with few-layer and monolayer. From the height profiles was obtained that the monolayer has about 0.9 nm of thickness, which is in agrement with the reported in the literature, and the few-layer region has around 10.0 nm of thickness, which implies that in these region there are about 11 single layers of WSe_2. The next step is to start with the structural and optical characterization by Raman and photoluminescence spectroscopy.

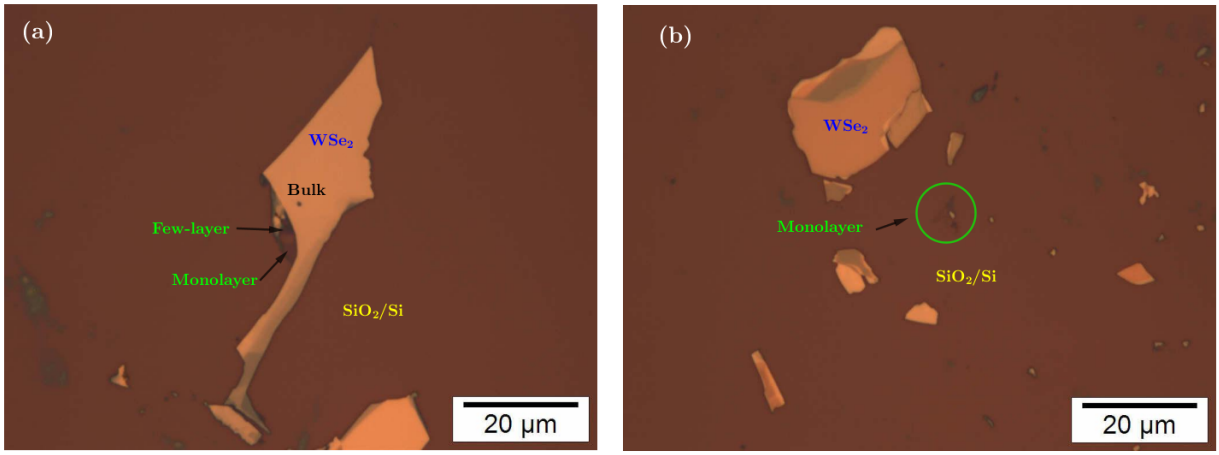

Figure 4.4: WSe_2 flakes on SiO_2/Si 300 nm. (a) monolayer at the edge of the flake. (b) isolated monolayer.

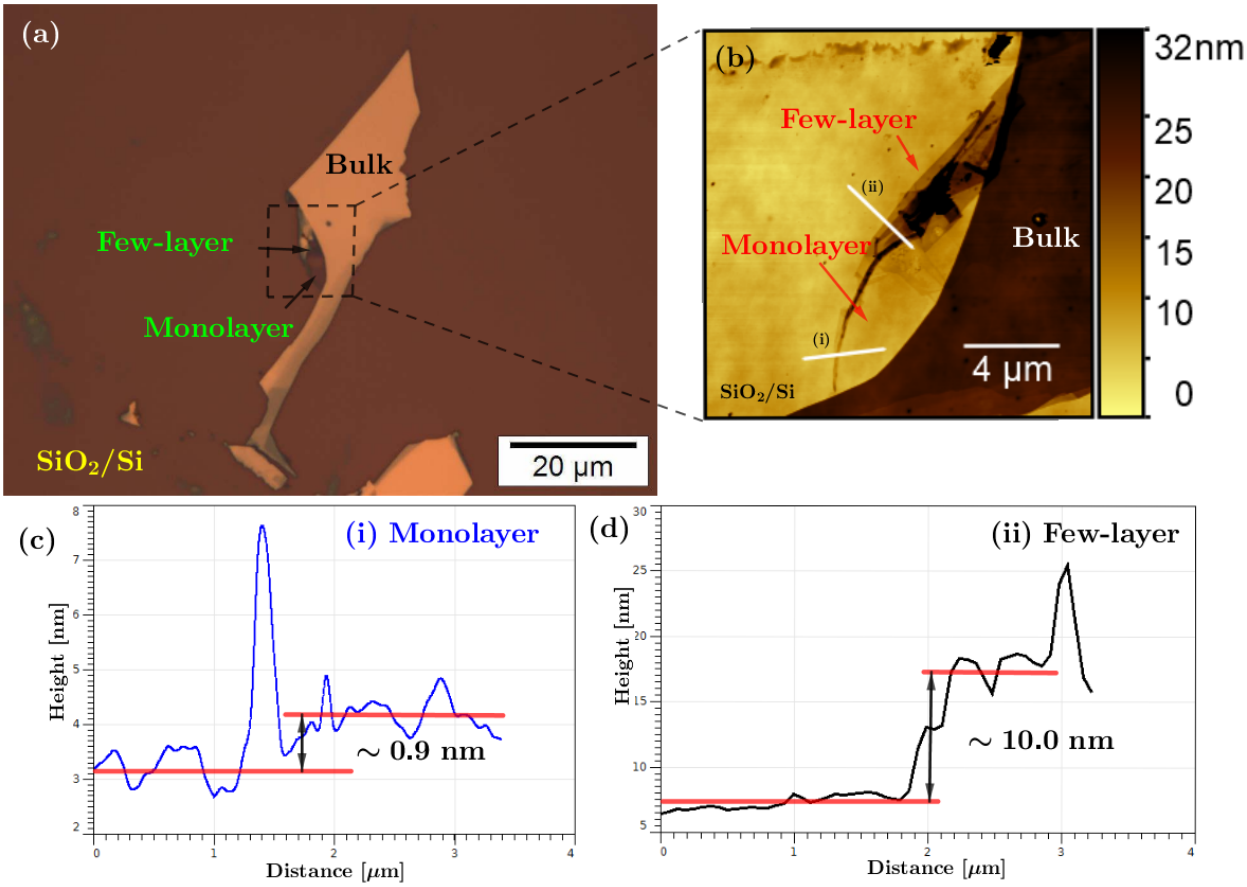

Figure 4.5: Morphological characterization of WSe_2 monolayer on SiO_2/Si 300 nm. (a) Optical image of the flake with few-layer and monolayer. (b) AFM image. (c), and (d) Height profile of the monolayer and few-layer region, respectively.

The Raman measurements were carried out using the XploRA Horiba micro-Raman of LAMULT, the system consists in an optical microscope coupled to a spectrometer with a

Si-CCD detector. The samples can be excited by using lasers with wavelength of 532 nm (green) or 638 nm (red). The spatial resolution is given by the laser spot-size, which is of about 2 μm for a objective lens of 100x and NA=0.90. Before to start the measurements, the system was calibrated for each laser using a silicon sample. The spectrum of Si obtained in the calibration of the micro-Raman spectrometer with the laser of 532 nm at room temperature is shown in figure 4.6, where as expected, the first order Raman peak is observed at 520 cm^{-1} and the second order Raman peak between 910-1000. After the calibration, the Raman spectrum of our samples was measured.

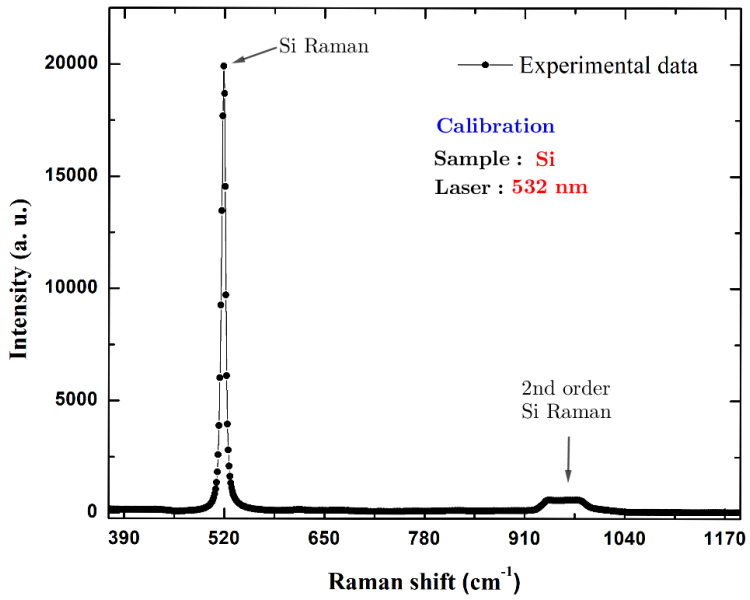

Figure 4.6: Silicon Raman spectrum obtained during the calibration of the micro-Raman spectrometer.

Figure 4.7 shows the Raman spectrum taken in the region with few-layer and monolayer of the flake described in figure 4.5. The sample was excited with the laser of 532 nm trough an objective lens of 100x at room temperature, the spectra were acquired using a 2400 gr/mm grating. In the spectra of figure 4.7(a) the strongest peak is observed around 250 cm^{-1} and corresponds to the activation of the Raman modes E^1_{2g} and A_{1g}, which are illustrated in figure 4.7(c). The unit cell for the 2H-WSe_2 crystal structure is shown in figure 4.7(b). From the figure, it can be seen that the Raman modes at 250 cm^{-1} are degenerate in few-layer but in the case of monolayer this degeneracy is broken and the Raman peaks corresponding to the vibrational mode E^1_{2g} (248 cm^{-1}) and A_{1g} (259 cm^{-1}) are separated by 11 cm^{-1} in agrement with the reported by Tongay, *et al.*, [53]. The Raman peak at 306 cm^{-1} corresponds to the interlayer vibrational mode B^1_{2g} that is optically active from bilayer to bulk and disappear in monolayer. The peaks between 350-400 cm^{-1} have been reported by Corro, *et al.* as second order Raman modes for WSe_2 [115]. Finally, the peak observed at 520 cm^{-1} comes from the substrate and corresponds to the silicon first order Raman peak. It is important to know that the sample remained stable in uncontrolled ambient conditions for about five months and no degradation was observed by Raman spectroscopy.

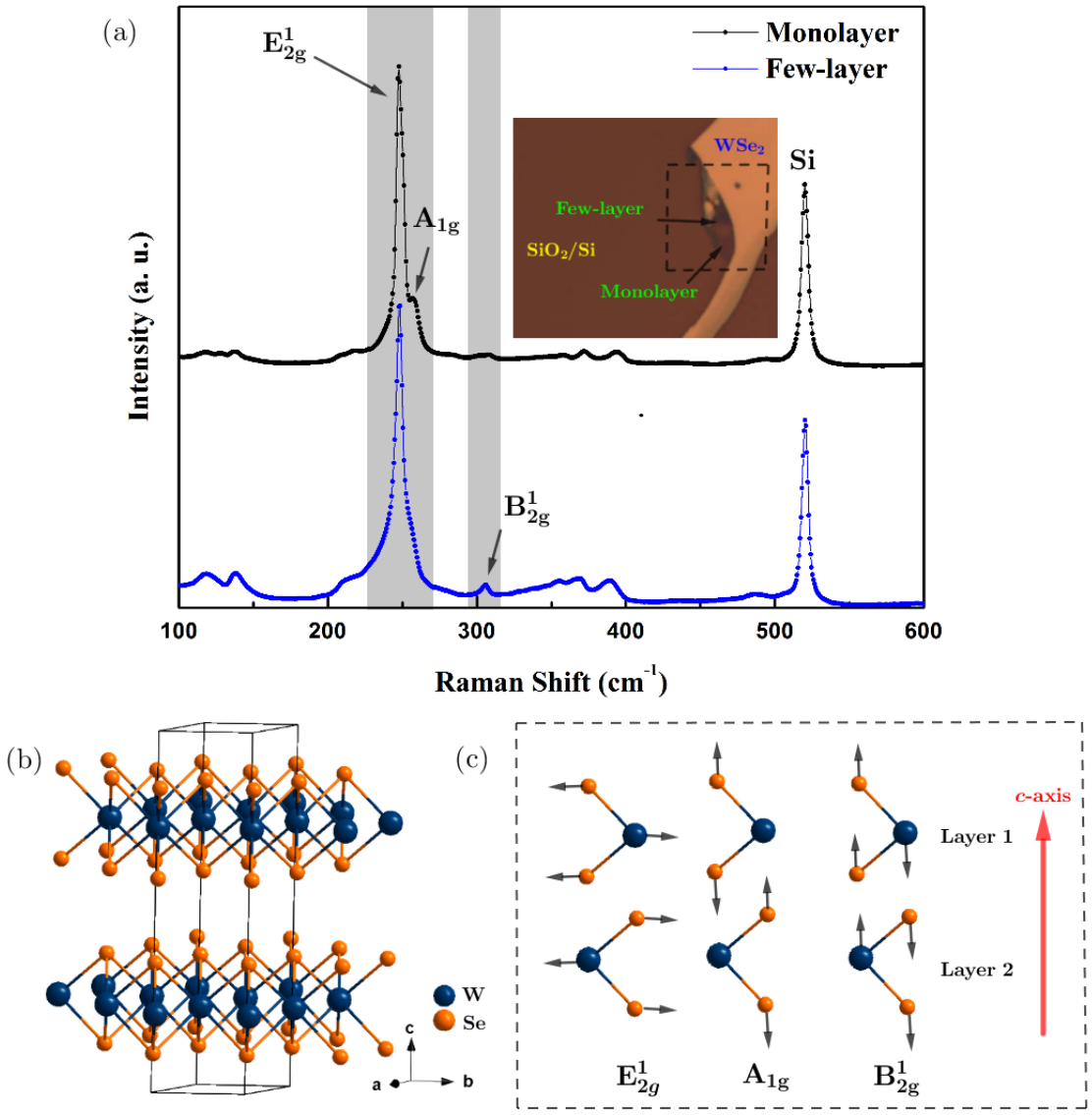

Figure 4.7: (a) Raman spectrum of WSe_2 monolayer and few-layer at room temperature. (b) Unit cell of WSe_2. (c) Active Raman modes.

So far the morphological and structural properties of one WSe_2 flake have been studied by AFM and Raman spectroscopy, confirming that WSe_2 monolayer was obtained. To study and understand the electronic properties of WSe_2, the photoluminescence spectroscopy technique was employed. The XploRA Horiba micro-Raman of LAMULT also was used to measure the PL response of the samples. To use the Raman spectrometer with the purpose of performing PL spectroscopy, the energy of the light illuminating the sample must be high enough to excite the electronic transitions in the material and the photoluminescence to occur. In order to learn and understand how to carried out PL measurements by using a micro-Raman spectrometer, a sample of Ruby (Al_2O_3:Cr^{+3}) was used as example. Figure 4.8 shows a set of Raman and PL spectrum taken a room temperature, using an objective lens of 100x and a 1800 gr/mm grating. The Raman spectrum shown in figure 4.8(a) was taken with the laser wavelength of 532

nm and the peak positions are in agrement with the reported in literature for Al_2O_3 [116]. The use of different excitation wavelengths allow to differentiate Raman scattering from photoluminescence. In figure 4.8(b) it can seen that the Raman peaks appear at the same Raman shift position, independent of the excitation wavelength. However, if the peaks appear at different Raman shift positions, then they are likely cause by photoluminescence. When the spectra are plotted as a function of the wavelength, such as is shown in figure 4.8(c), the PL peak is confirmed because this appear at the same positions independent of the excitation wavelength. The PL peak is resolved better in the inset figure, where two strong emission are observed which are known as the R-lines fluorescence and arises from Cr^{+3} impurities in Al_2O_3.

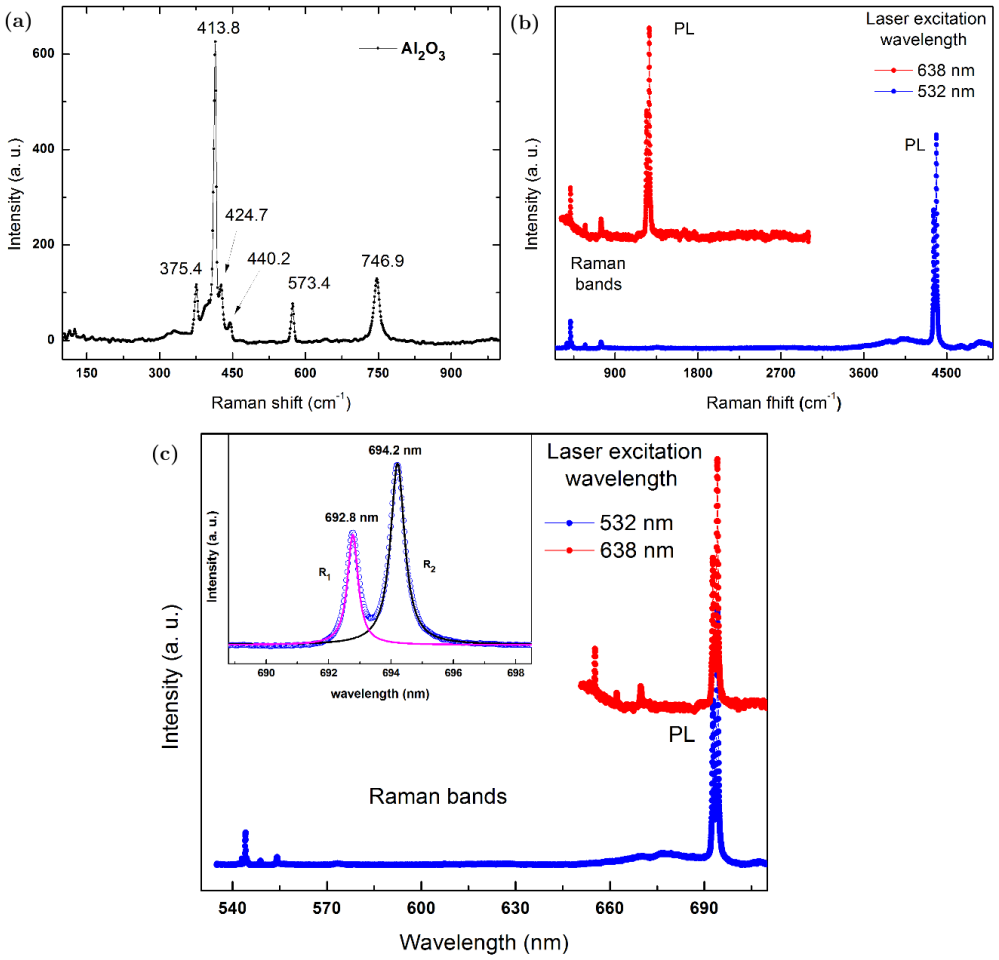

Figure 4.8: (a) Raman spectrum of Al_2O_3:Cr^{+3}. (b) Raman spectra taken at the same position of Al_2O_3:Cr^{+3} sample using excitation wavelength of 532 and 638 nm. (c) PL spectra taken at the same position of Al_2O_3:Cr^{+3} sample using excitation wavelength of 532 and 638 nm. Intet: PL peak well resolved.

The PL spectra of WSe_2 shown in figure 4.9(a) were taken at room temperature, exciting the sample with 532 nm trough an objective lens of 100x. Such as was mentioned above, in this conditions the laser spot-size is about 2 μm. To acquire the spectra a 600 gr/mm grating was used. In figure 4.9(a) the PL spectrum of monolayer is shown, where a

strong emission is observed at 1.63 eV (∼760nm) and it is associated to the A exciton recombination through the direct band-gap at K point of the Brillouin zone. The energy value found for A transitions in monolayer is in perfect agrement with the value reported by Yan, *et al.* [117]. Another emission of lower intensity and higher energy is observed around of 2.0 eV, this emission likely is due to the B exciton recombination. The energy separation between A and B peaks is about 370 meV, which is an indication of the strength of the spin-orbit interaction that produce the spin-splitting in the valence band in tungsten dichalcogenides compounds [39, 118, 119]. Figure 4.9 (b) shows the PL emission of monolayer and few-layer, the spectrum of few-layer shows a broad peak at 1.49 eV with lower intensity than that observed in monolayer due to the fact the luminescence in few-layer and bulk involve indirect transitions between the Γ and Q points. When the number of layers in the sample is reduced to monolayer, the indirect band-gap between the Γ and Q point becomes direct band-gap at K and the PL intensity achieve it maximum value, being twenty times stronger than in few-layer. Figure 4.9(c) shows the electronic band-structure calculated by Roldán, *et al.* using DFT theory considering spin-orbit interaction effects in the direction of the Brillouin zone shown in figure 4.9(d) and [39]. In the band structure, the indirect transition, as well as, the direct exciton A and B transitions are illustrated by red arrows which are originated from ground excitonic states localized very near of the CB minimum.

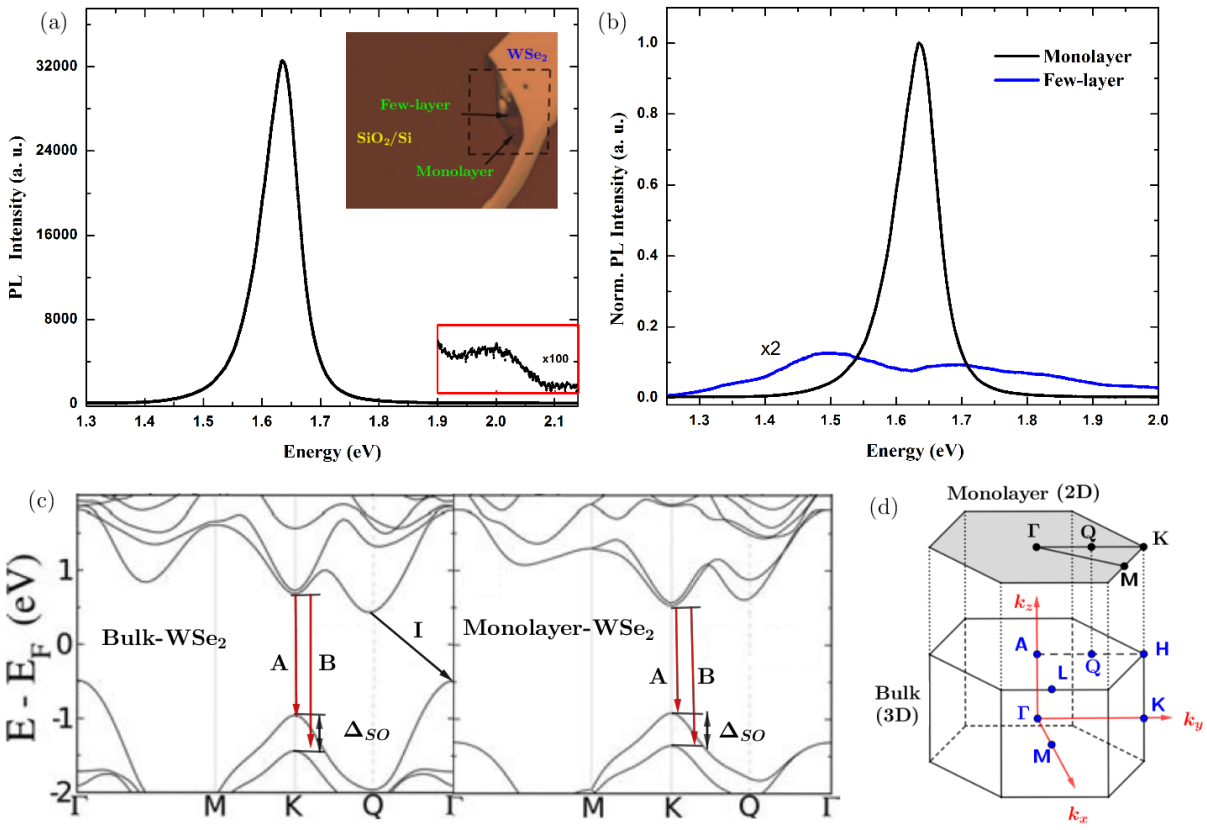

Figure 4.9: (a) PL spectrum of WSe_2 monolayer. (b) PL spectra of monolayer and few-layer. The spectra were taken at room temperature.(c) Electronic band structure of WSe_2 monolayer and bulk, adapted from [39]. (d) First Brillouin zone.

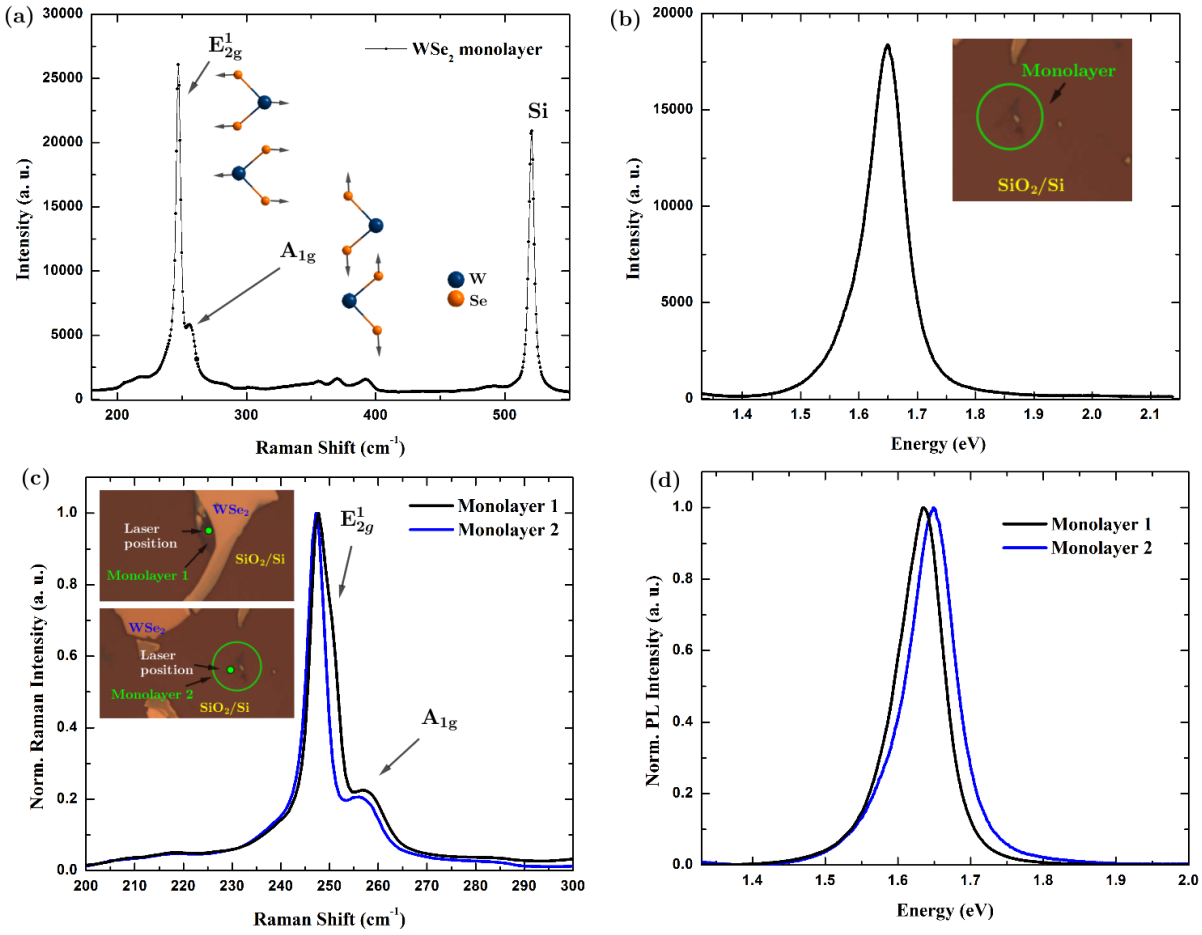

Figure 4.10: Characterization of the WSe_2 monolayer shown in figure 6(b). (a) Raman spectrum and (b) PL spectrum at room temperature. Comparison between (c) Raman and (d) PL spectra of monolayer 1 and 2. The monolayer of figure 4.4(a) and (b) were called now as monolayer 1 and 2, respectively.

In figure 4.10 are shown the results obtained in the structural and optical characterization of the sample shown in figure 4.4(b). The Raman and PL spectra were taken in the same conditions that the monolayer described above. In the Raman spectrum the vibrational modes E^1_{2g} and A_{1g} at 250 cm^{-1} are not degenerate and the B^1_{2g} mode had not been observed, such as is expected in monolayer. The second order Raman peaks are between 350-400 $^{-1}$ and the Si Raman peak at 520 cm^{-1}. The PL spectrum has the typical signature of the emission in monolayer, which consist in a strong peak related to the recombination of A exciton, observed in this sample at 1.65 eV, value that matching with the reported by Tongay, *et al.* [53] and by Tonndorf, *et al* [66]. When the emission of both monolayer in figure 4.4, called as monolayer 1 and 2 in figure 4.10(c) and (d), are compared it is found that there is a difference in energy of 20 meV between the A exciton peaks. Some authors have reported that, in general, the intensity and position of the PL peak in monolayer depend on the region of the sample where the spectrum was acquired. The inset figures show the laser position to indicate the site where the spectrum was measured. In the case of the monolayer 1, the Raman and PL spectra were taken near of the few-layer region, while in the monolayer 2 the spectra were acquired in a random

position on the monolayer. The shift in the position of the PL peak is accompanied by a small shift in the Raman peak position A_{1g} , as well as, in the width of the E^1_{2g} Raman peak, such is shown in figure 4.10(c) and (d). In Raman spectroscopy, the width of the Raman peak is associated with the crystallinity of the sample and shift in the peak position with stress/strain effects. Therefore, figure 4.10(c) tells us that the crystal quality of the monolayer 2 is better than monolayer 1. Since monolayer 2 is an isolated monolayer (free of stress) and monolayer 1 is part of a big flake and the spectra were taken near of the few-layer region, the shift in the peak position in Raman and PL are likely due to stress/strain effects. In an attempt to create defects in monolayer with the intention of study the optical emission related to defects, the monolayer 2 was subjected to a thermal annealing treatment which consisted in place the sample into a quartz tube furnace at 500 ^{0}C for 10 minutes in an atmosphere of 1000 sccm of argon. Figure 4.11 shows optical images of the sample before and after the thermal annealing, where it can be seen that the sample did not resist the treatment and the monolayer disappeared, it was evaporated. To avoid to lose the monolayer 1 too, and continue with the study of the optical properties of pristine monolayer no thermal treatment was applied in this sample.

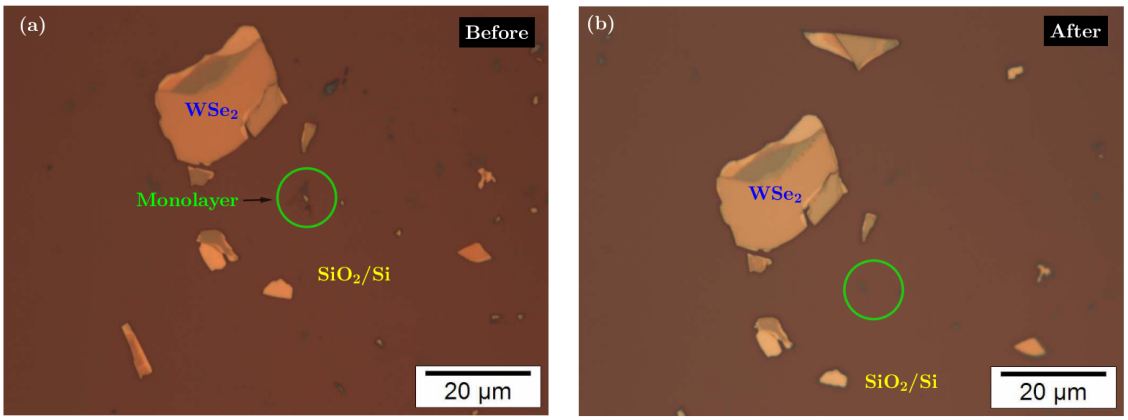

Figure 4.11: Optical images taken (c) before and (d) after a thermal treatment.

The excitonic effects involved in the light emission of monolayer can be better understood looking figure 4.12. This PL spectrum was taken using the micro-Raman/PL setup of GPO. The sample was excited with a laser of 488 nm at room temperature, using a objective lens of 50x (NA=0.55) and a power excitation of 0.8 μW. To acquire the spectrum a 600 gr/mm grating was used. The inset figure shows the flake and the laser position that define the region of the sample that was excited, being the laser spot-size of about 2 μm. The PL spectrum shows the A exciton emission as an asymmetric peak at 1.65 eV. The peak position is the same that the one found in monolayer 2, which implies that the sample was excited in a region of good crystal quality and free of stres/strain. The A exciton emission is a superposition of trions and neutral excitons emissions. The PL experimental data was fitted using two Voigt functions for the trions and excitons contributions.The Voigt profile takes into account the Lorentzian distribution of radiative processes in luminescence and the gaussian distribution associated to experimental factors. The emission is dominated by the neutral exciton recombination at 1.65 eV. The integrated intensities ratio shows that trions contribution at 1.62 eV is about 28%

of the total emission. The energy difference between excitons and trions is 30 meV, and it corresponds to the trions binding energy (see figure 2.5(a)). At room temperature, the thermal energy is about 25 meV, so this energy is enough to dissociate the most of trions. This explain why the PL emission is dominated by the neutral exciton recombination.

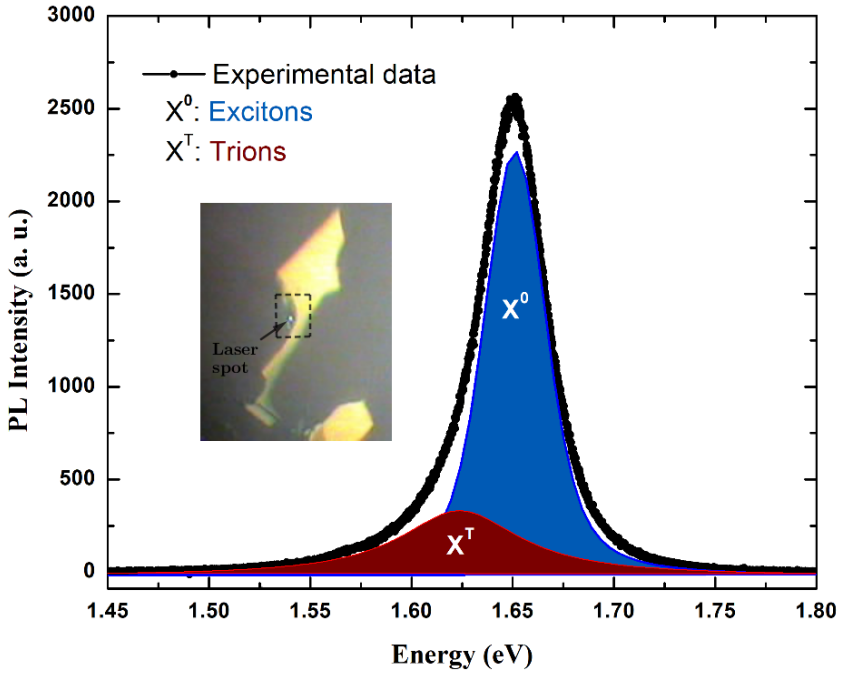

Figure 4.12: PL spectrum of WSe_2 monolayer at room temperature (black curve), the spectrum was fitted (red line) with two Voigt function for the trion (blue line) and exciton (green line) contributions.

In figure 4.13(a), the PL spectrum of WSe_2 monolayer taken at 300 K and 10 K are compared. The spectrum at room temperature was obtained exciting the sample with 488 nm and 0.6 μW of power, while at 10 K it was only possible obtain PL sinal using a excitation power of 1.0 μW. Both spectra were acquired in the same sample region and with the same acquisition time. From the figure it can be seen that A exciton peak is observed around 1.65 eV, and the PL intensity at room temperature is about six times higher than the observed at 10 K. This temperature dependent PL behavior can be explained considering the spin-splitting of the CB and VB in the K valley shown in the inset figure. The radiative (bright) A and B exciton transitions are indicated by orange and blue arrows, respectively. The A exciton recombination involve transitions between the second exciton sub-band and the first VB sub-band, while the B exciton recombination involves transitions between the lowest exciton sub-band and the second VB sub-bands. The non radiative exciton recombinations are indicated as dark excitons. The CB and exciton level splitting in tungsten dichalcogenides monolayer (WX_2) is comparable to the k_BT energy at room temperature. Therefore, at low temperature the exciton population tends to accumulate in the lowest exciton energy which is dark. In contrast, at room temperature the thermal energy is enough to excite electrons to the second exciton sub-band which is bright and the most of recombination are radiative. For these reasons, the optical response at low temperature is weak even exciting the monolayer with higher

excitation power. Figure 4.13(b) and 4.13(c) shows the excitons and trions contribution to the light emission in monolayer at 300 K and 10 K, respectively. At 300 K, such as is expected, the light emission is governed by the optical recombination of neutral A excitons with a contribution of only 17% due to trions. This trions contribution is lower than that observed above where a excitation power of 0.8 μW was used. When lower excitation power is used, the number of electron-hole pairs created by optical transitions decreases, then the number of charge carriers available to form trions is smaller, this together to the fact that the thermal energy dissociate the most of trios leads to the observation of a smaller contribution due to trions. On the other hand, at 10 K the contribution due to trions is more significant (about 43%), which is attributed to the fact that at low temperature the trions are not dissociated and the bright exciton ground state begins to be less populated, then the number of non-radiative recombination increases due to the darkish behavior of WSe_2.

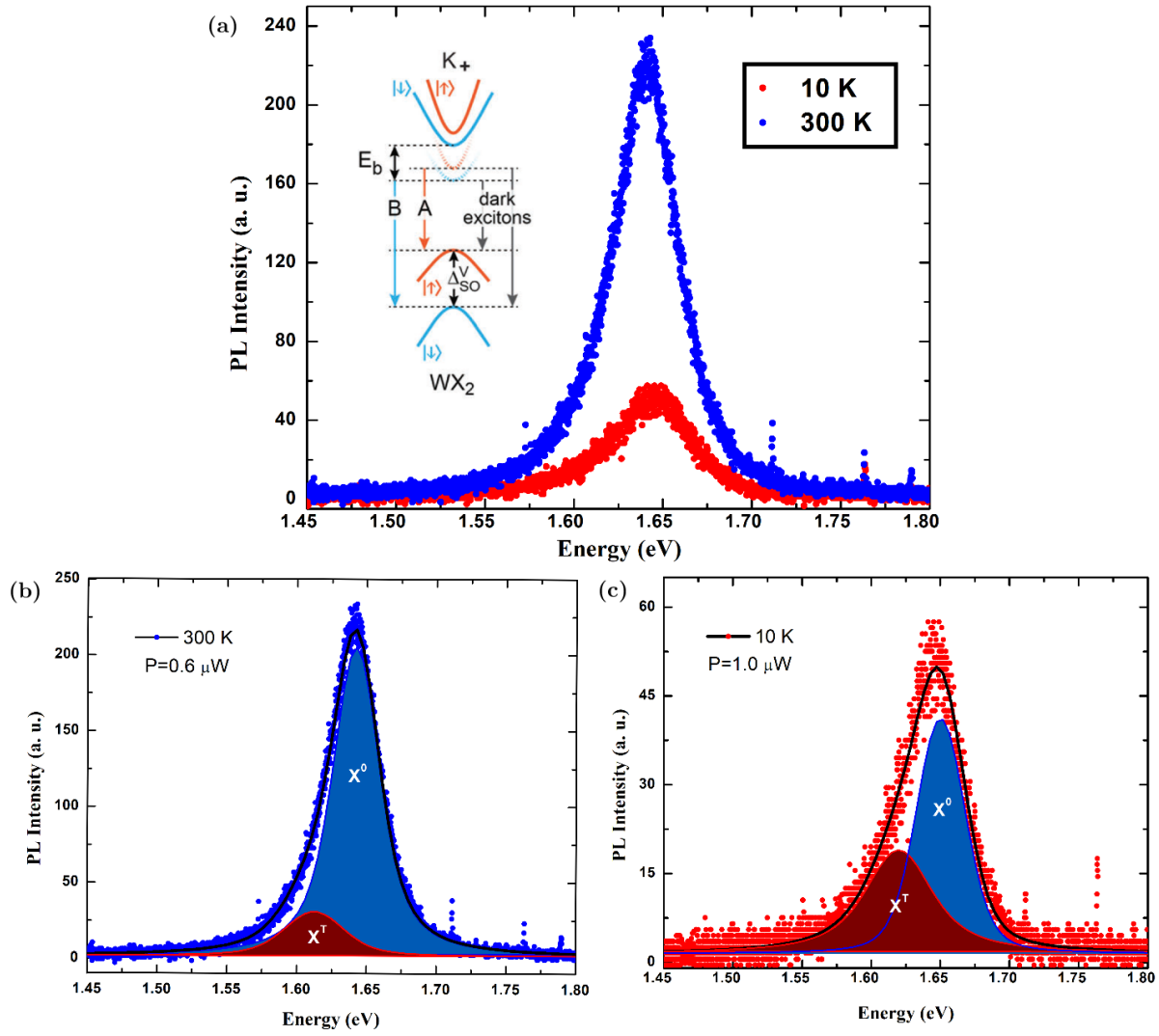

Figure 4.13: (a) Temperature dependent of PL in WSe_2 monolayer. Inset: electronic band-structurer at the K valley (Adapted from [12]). Exciton and trion contributions at (b) 300 K and (c) 10 K.

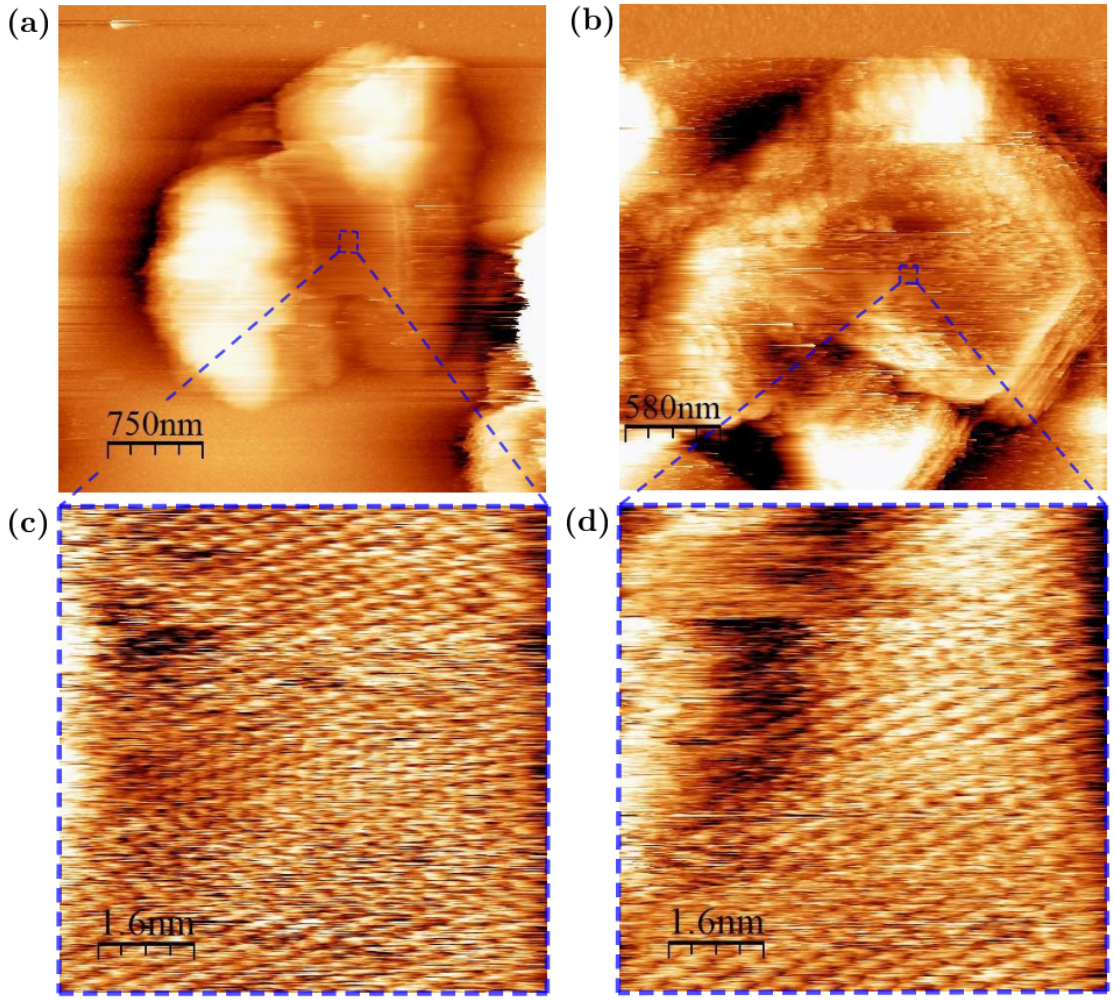

Figure 4.14: Constant-current STM images taken at 80K in mechanically exfoliated flake on Si p-doped substrate . (a) 3.7 μm ×3.7 μm STM image (V_B= -5.2 V , I_T= -1.00 nA). (b) 2.9 μm ×2.9 μm STM image (V_B= -5.4 V , I_t= -0.600 nA). (c) 8.0 nm × 8.0 nm STM image (V_B= -3.8 V , I_T= -500 pA). (d) 8.0 nm × 8.0 nm STM image (V_B= -3.8 V , I_T= -500 pA)

Such as it was mentioned in chapter 3, a low-temperature ultra-high vacuum STM was installed in our laboratory a few months ago. In order to learn how to operate the microscope and obtain the first images with atomic resolution, topographic images in the constant-current mode and using a tungsten tip were taken in typical samples such as high oriented pyrolytic graphite (HOPG) and Si(111). The tip preparation method and the STM images of these samples are shown in appendix C. Once acquired the necessary knowledge about the STM operation, samples of WSe_2 were prepared to carry out STM measurements. To obtain STM images of WSe_2 and study its atomic structure, a suitable conducting substrate must be used. Since SiO_2/Si is an isolating substrate, flakes mechanically exfoliated were deposited on silicon p-doped substrate ($\rho = 0.01 - 0.09\Omega$-cm). In figure 4.14(a) and (b) are shown STM images of two different WSe_2 flakes taken at 80 K in the constant-current mode. All STM images were processed using the *WSxM 5.0* software [120]. It was only possible to obtain STM images in this sample using negative bias with which the tunneling current was kept relatively constant and stable.

This likely is due to the fact that in negative bias electrons tunnels from the sample to the tip, therefore the occupied states of the samples are mapped to obtain the STM images. The samples were not degassed before to measure, however the flake in figure 4.14(a) seems to be cleaner than flake in 4.14(b). In the central part of the flake in 4.14(a) it can be observed a clean and flat region. Figure 4.14(c) shows an image of 8.0 nm×8.0 nm taken in this region in which the atomic arrange of the WSe_2 structure can be observed. The quality of the image is not too good and this may be due to the sample not being clean enough and it should be degassed or that the tunnelling tip is oxidized and its necessary to apply some treatment post tip preparation. Figure 4.14(d) shows an atomic resolution image taken in the flake of 4.14(b) but in this case the image is worse due to the fact that this flake is more dirty than the first one. After measure the last flake the STM tip changed and it was not possible to recover it. It is important to say that some sample cleaning protocols and e-beam treatment in the STM tips are being established to improve the quality of our STM measurements. On the other hand, we tried to measure some STS curves to explore the electronic properties of the samples, however the obtained results were ambiguous, maybe the tunneling parameters used were not the appropriated or the tip was not suitable for STS measurements.

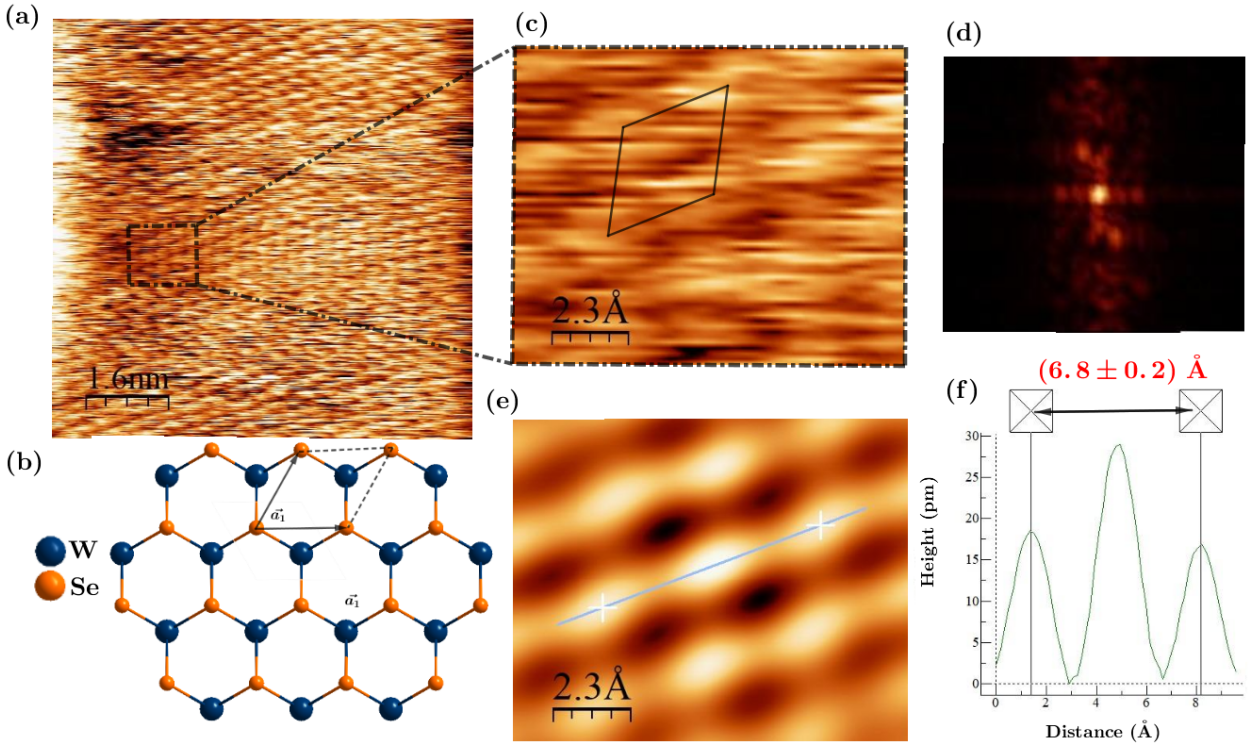

Figure 4.15: Atomic structure of WSe_2. (a) 8.0 nm × 8.0 nm STM image (V_B= -3.8 V , I_T= -500 pA). (b) Top-view of the WSe_2 atomic structure. (c) Zoom image of 1.20 nm × 0.94 nm. (d) Fourier transform image. (e) FFT filtered image. (f) Measurement of the interatomic distance

Although the quality if the STM images with atomic resolution is not good, the lattice parameter of the WSe_2 atomic structure was estimated as shown in figure 4.15. A small region of the figure 4.15(a) with the atomic periodicity of the WSe_2 surface shown in figure 15(b) was chosen. The selected region is shown in figure 4.15(c) where the

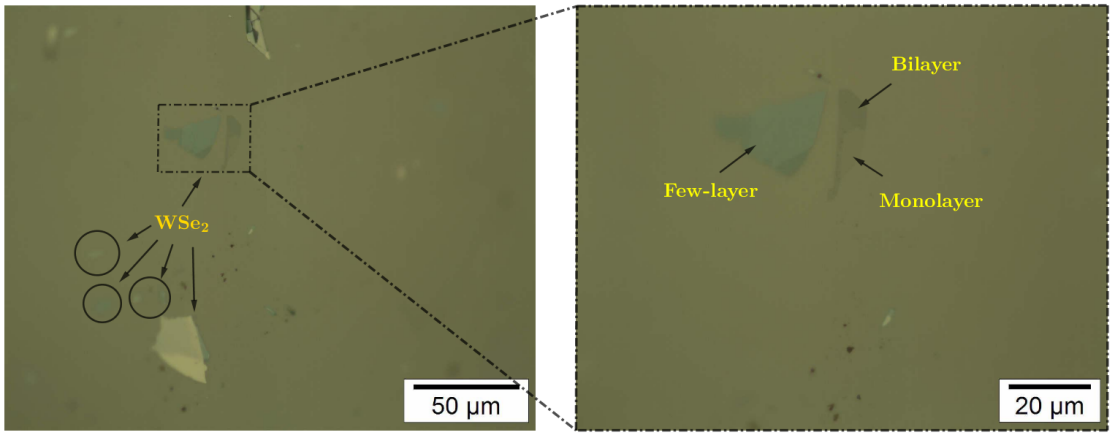

Figure 4.16: Optical microscopy images of WSe_2 flakes mechanically exfoliated on HOPG.

hexagonal arrays of the top layer of Se atoms can be observed. In figure 4.15(d) is shown the corresponding Fourier transform which tells us that there are features in the real image that occur with a specific period (atomic structure), so to extract important structural information from the data, the real image is filtered passing only the signals with the frequencies represented in the Fourier transform, the filtered image is shown in figure 4.15(e), where the white dots represent the atomic positions of the Se atoms. The interatomic distance between Se atoms give us the lattice parameter value. To obtain this information, a line from one white dot center to another white dot center was drawn and the distance for 2 atomic space has been measured such as is shown in figure 4.15(f). The interatomic distance is calculate by dividing this distance by the number of atomic space, this is, $d = 6.8/2$ nm which gives a lattice parameter of $a = (3.4 \pm 0.1)$ Å. The value for the lattice parameter found here is very close to reported values in the literature, e. g.,b Park, *et al.* determined this lattice parameter from STM measurements and reported $a = (3.2 \pm 0.1)$ Å[121].

In order to study point defects in WSe_2 by STM and STS measurements, such as shown in figure 3.13 for MoS_2, some samples of WSe_2 mechanically exfoliated on HOPG have been prepared. Figure 4.16 shows optical microscopy images of one of these samples, where flakes of WSe_2 and even monolayer can be observed.

4.2 Preparation and characterization of WS_2 and h-BN flakes

One of the drawbacks of samples mechanically exfoliated is that it is difficult to find the flakes during the STM measurements. With the purpose of making easier the observation of flakes in STM and ensure that anywhere on the sample where the STM tip is approached flakes will be observed, samples of commercial solvent-exfoliated flakes of WS_2 (Graphene Supermarket) were prepared by the drop-casting and spin-coating methods. The properties of the WS_2 solution given by Graphene Laboratories say that the substance has a concentration of 25 mg/L and consists of nanoflakes with lateral

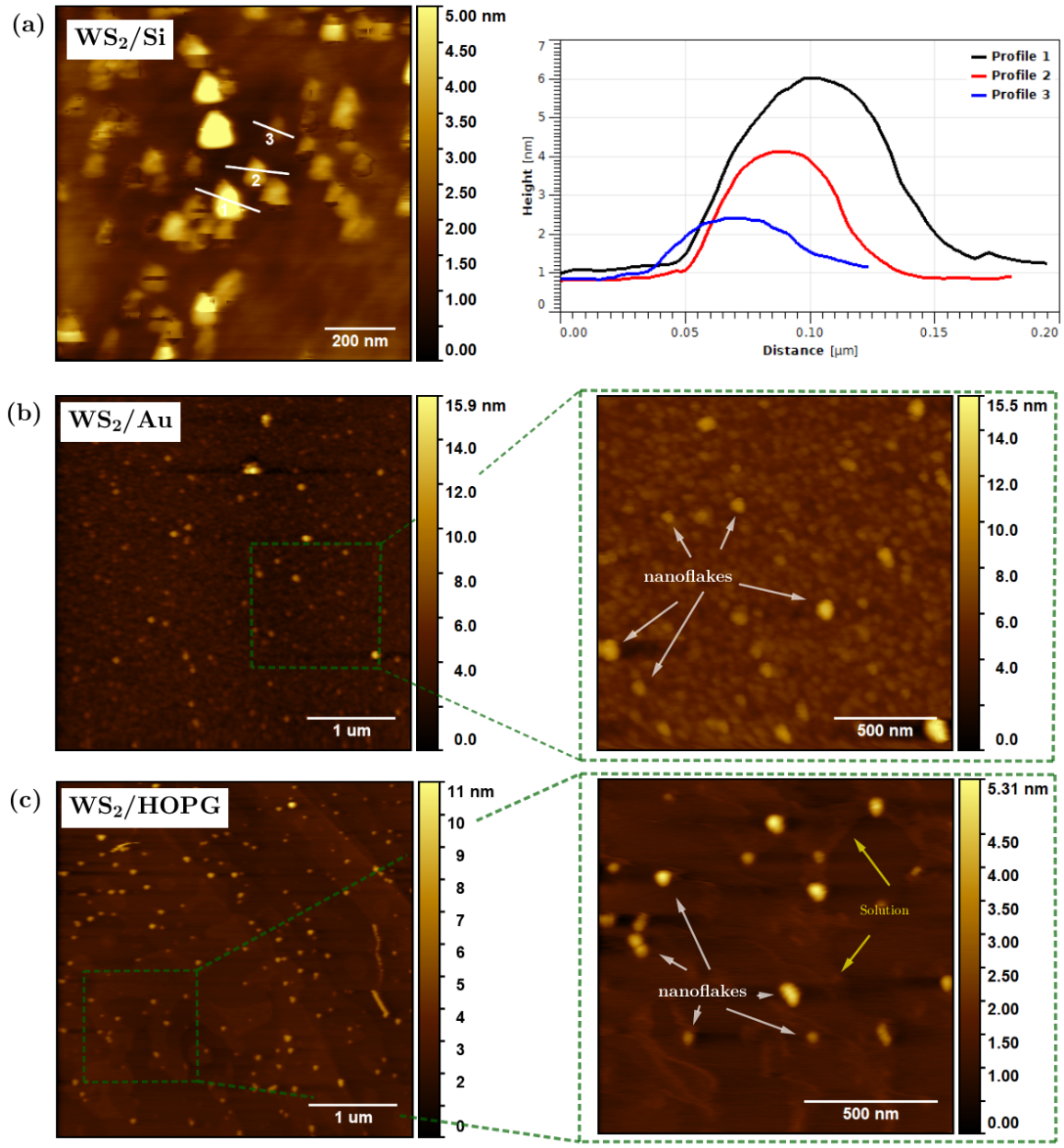

Figure 4.17: AFM image of nanofllakes of WS_2 deposited on (a) silicon p-doped, (b) gold and (c) HOPG substrate.

size of 50-400 nm and thickness of 1-8 monolayer suspense in a mix of water (45%) and ethylic alcohol (55%). Figure 4.17 shows several AFM images of samples prepared drop-casting 50 μL of the nanoflakes solution on different substrate and spin-coating with a speed of 3000 rpm in order to spread the nanoflakes uniformly on the substrate by centrifugal force. Before the deposition of the sample, the solution was sonicated in an ultrasonic cleaner by one hour. The idea of using different substrate is evaluate which one is the best to measure in the STM. The AFM images were taken in a random place on each one of the samples. Figure 4.17(a) shows an AFM image of nanoflakes deposited on silicon p-doped substrate where a high density of flakes is observed. From the height profile it can be seen that the flakes labeled as 1, 2, and 3 have approximately

a thickness of 5, 3, and 1 nm. The flake 3 can be considered as one monolayer of WS_2 with lateral size of $\sim$ 60 nm. Comparing all AFM images in figure 4.17, it can be noted that gold (Au) substrate seems to be rougher than the others which could make difficult the identification of nanoflakes, mainly monolayers. Eventually, Au substrates with more suitable preparation will be used. When the flakes are deposited on HOPG, such is shown in figure 4.17(c), it was found that the solvent of the nanoflakes solution does not evaporated during the spin-coating process. From the figure it can be observed that the sample has a high density of flakes but all of them are inside of a small lake of the solution. If the STM tip touch this solution the tip will be contaminated and it will not be possible to make the measurements. To avoid this contamination, the samples were subjected to different thermal treatments. In the case of the sample shown in figure 4.18, the thermal treatment consisted in annealing the sample at 200 ° C during one hour. After this treatment was very difficult to find flakes by AFM due to the fact that the evaporation of solution lead to the formation of spots on the substrate where most of the nanoflakes were concentrated.

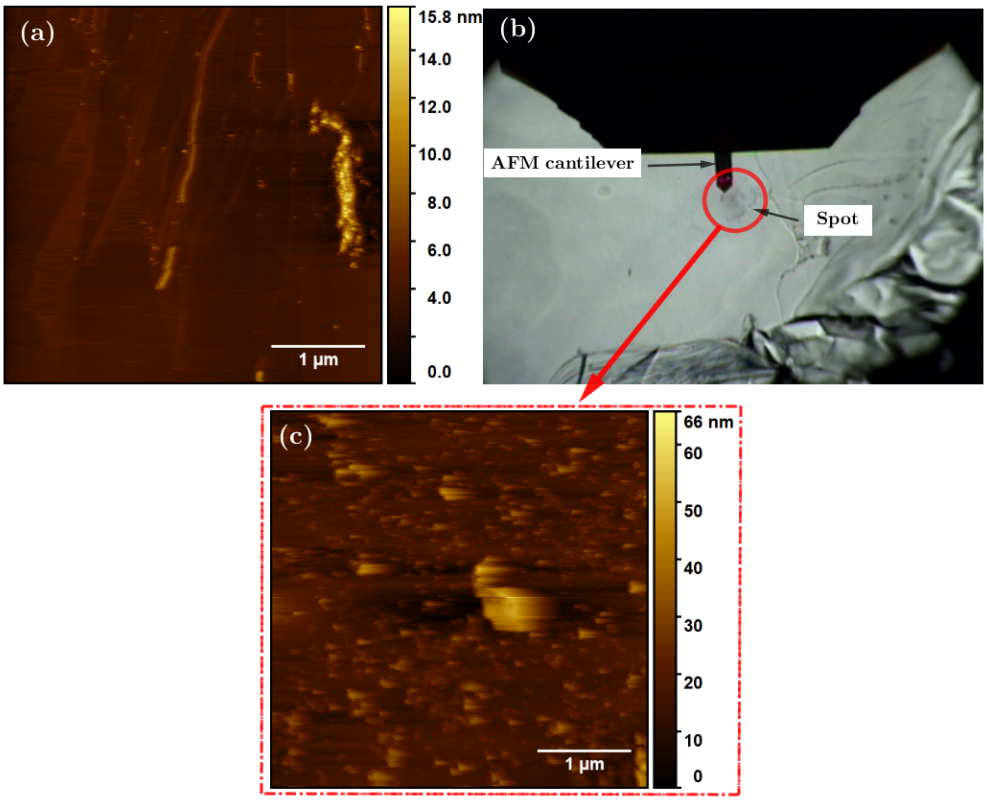

Figure 4.18: (a) AFM image of the WS_2/HOPG sample after being heated at 200 °C during 1h. (b) optical image of the AFM cantilever positioned on a spot of evaporated solution. (c) AFM image taken on the spot.

Based on the AFM results and taking into account the experience with WSe_2, the sample of WS_2/Si was introduced into the STM, but before performing the measurements, the sample was degassed in the load lock chamber at 120 ° overnight (baking). During the STM measurements was found the same behavior observed in the sample deposited on HOPG. Spots of solution were formed as results of the baking process. In figure 4.19(a) is

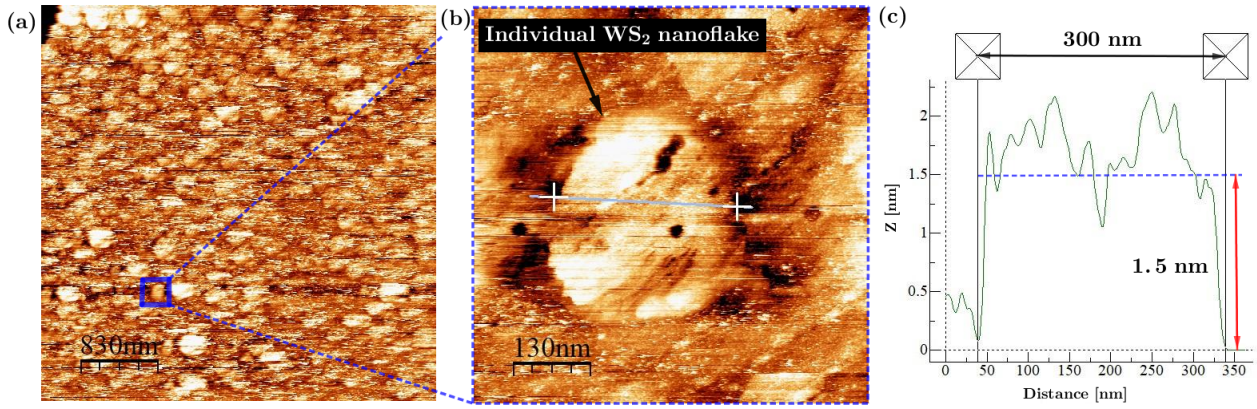

Figure 4.19: Constant-current STM images of WS_2 nanoflakes deposited on Si p-doped substrate taken at 80K. (a) 4.2 μm ×4.2 μm STM image (V_B= -4.9 V , I_T= -0.800 nA). (b) 645 nm ×645 nm STM image (V_B= -5.7 V , I_t= -0.800 nA). (c) Hight profile of the individual nanoflake.

shown the STM image taken in one of these spots, the image looks as if the all the scanned area was covered with nanoflakes, similar to the image in figure 4.18(c). The STM image of an individual nanoflake is shown in figure 4.19(b), the height profile in figure (c) shows that this flake has a lateral size of ∼300 nm and a thickness of ∼1.5 nm which implies that one flake of 1 or 2 monolayer has been imaged. Finally, a UV-Vis spectrometer was used to measure the absorbance spectrum of the nanoflakes solution, which is shown in in figure 4.20 and where the absorption associated with the A and B exciton transitions are observed at 2.0 and 2.4 eV, respectively. The A and B absorptions are separated by 400 meV which corresponds to the splitting of valence band edge [118, 119].

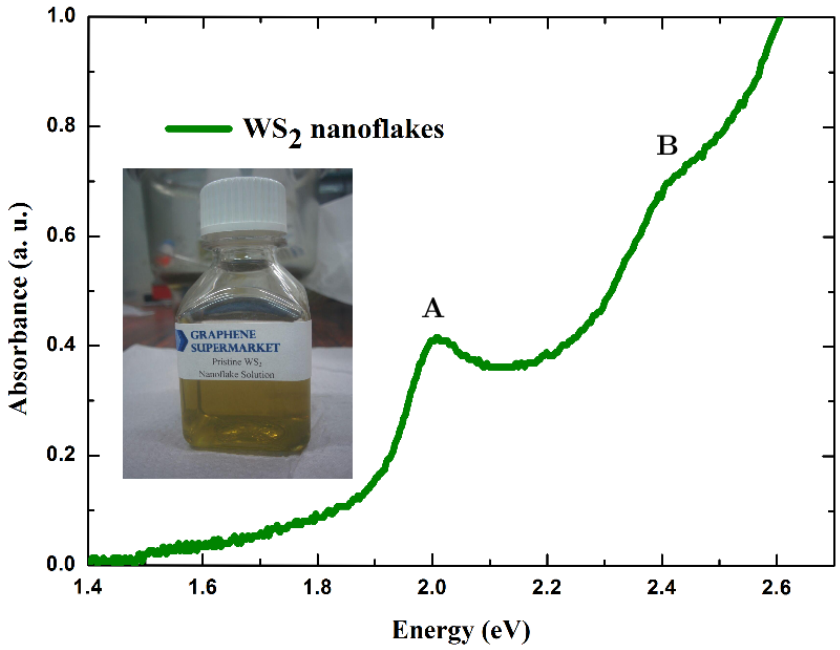

Figure 4.20: Absorbance spectrum of the WS_2 nanoflake solution at room temperature.

To prepare the h-BN samples, 10 mg of h-BN power was dissolved in 10 mL of isopropanol and the solution was sonicated during several hours. After that 100 μL of solution was dropped on silicon substrate, in figure 4.21 it can be seen that most of flakes are microflakes of bulk h-BN. To create defects in the h-BN microflakes, the sample was placed in a quartz tube furnace and annealed first at 500 °C for 10 minutes with the purpose of eliminate impurities and after the thermal cleaning the sample was heated at 850 °C during 30 minutes with a flux of 1000 sccm of argon. These parameters for thermal annealing are based on those reported by Tran , et al., [13, 78]. Figure 4.22 shows the Raman spectrum taken exciting a h-BN microflake with 532 nm at room temperature. The measurements were made using the micro-Raman spectrometer of LAMULT in the same conditions of the WSe_2 sample analysis. The Raman spectrum consist in two peaks, one peak at 520 cm^{-1} corresponding to the silicon Raman peak of the substrate, and another peak at 1365.4 cm^{-1} corresponding to the E_{2g} intralayer vibrational Raman mode of h-BN. The fitting in figure 4.22(b) shows that the E_{2g} peak has the typical Raman signature of h-BN in bulk, this is, a peak position around 1365 cm^{-1} with a FWHM of 9.3 cm^{-1} (see chapter 2 section 2.2). This Raman signature was observed in most of h-BN flakes.

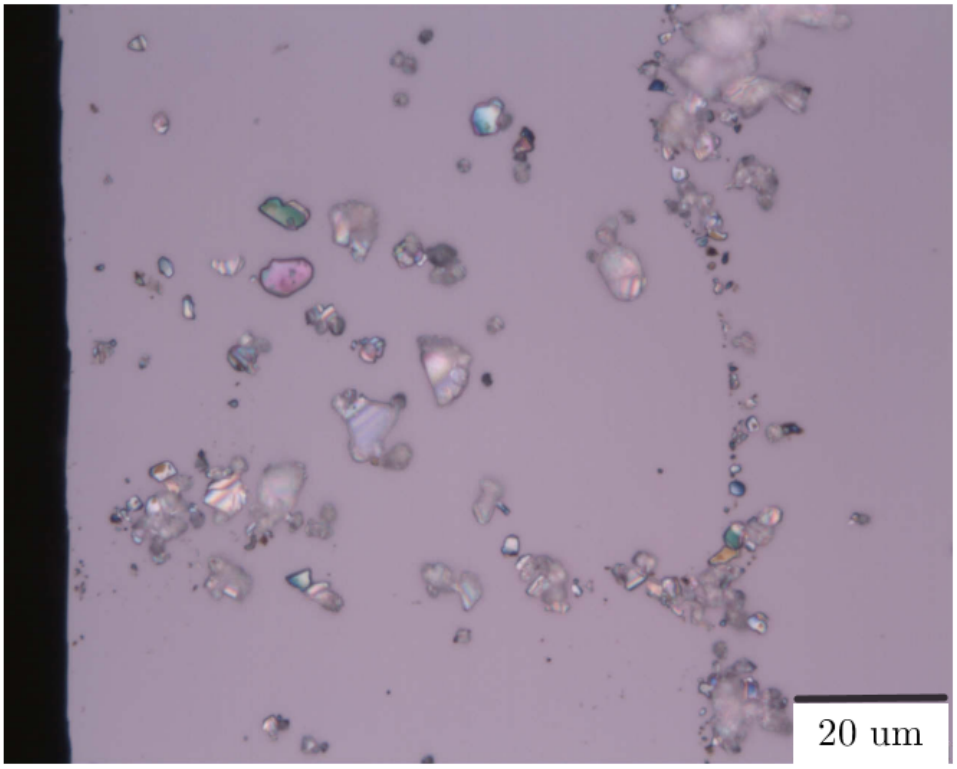

Figure 4.21: Optical microscope image of h-BN microflakes on silicon substrate.

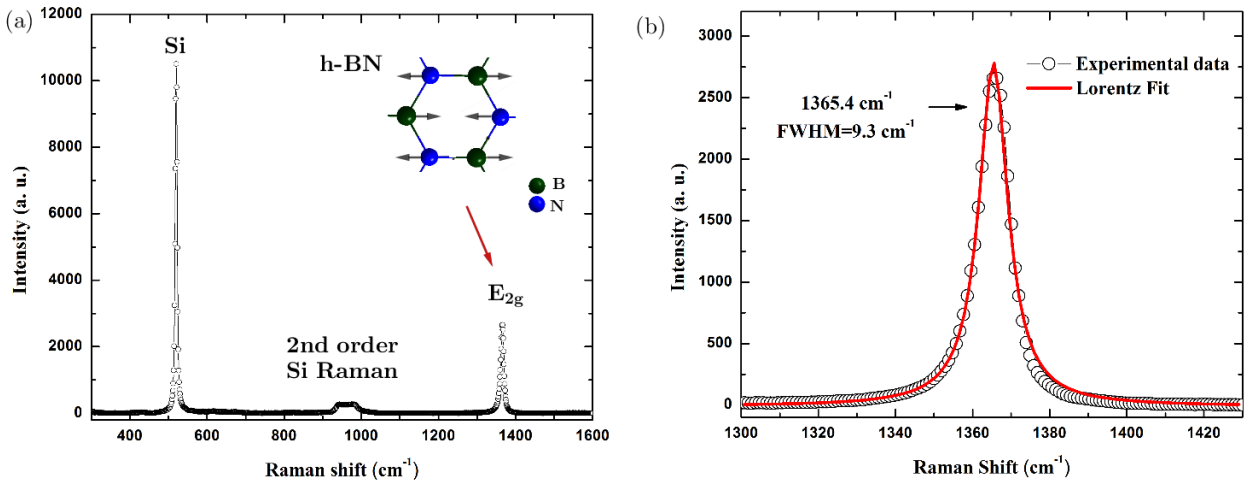

Figure 4.22: (a) Raman spectrum of h-BN at room temperature. (b) Fitting of the E_{2g} Raman peak.

During the Raman measurements using the laser of 532 nm a broad peak was observed in the Raman spectrum above 2000 cm^{-1}. To know the origin of this peak, the sample was excited using different excitation wavelength to differentiate Raman sinal from PL emission. Figure 4.23 shows two Raman spectra taken at the same position on the h-BN microflake shown in the inset figure but using different excitation wavelength. Both spectrum present the Raman peak of the E_{2g} vibrational mode around 1360 cm^{-1} but the peak around 2200 cm^{-1} disappear when the sample is excited with 638 nm. This allow us to associated this peak to PL emission. Plotting this PL emission as a function of the emission energy, the PL spectrum shown in figure 4.24(a) is obtained. The spectrum has the optical signature of the light emission related to point defects in h-BN, which consists in a narrow peak with FWHM=15 meV and strong emission at 2.06 eV (602 nm) associated to ZPL transitions and a phonon replica or phonon side-band transition (PSB) observed at 1.90 eV (652 nm), being the energy difference between the ZPL and PSB transitions of 160 meV. These values are in perfect agreement with values reported by Tran, *et al.*, [13] for the single photon emission in h-BN, where the supposed point defects responsible by the emission are of the type N_BV_N. The ZPL and PSB transitions are shown in the energy diagram of figure 4.24(b). The electronic states of point defects into the crystal are strongly coupled to the vibrational modes though the electron-phonon interaction. From the figure it can be seen that the transitions between the lowest vibrational level of the excited electronic states at $Q_0^{'}$ and the lowest vibrational level of the ground electronic at Q_0 state are called zero-phonon line (ZPL), since there are no vibrational quanta involved. The other possible transitions are called as phonon replicas or PSB transitions.

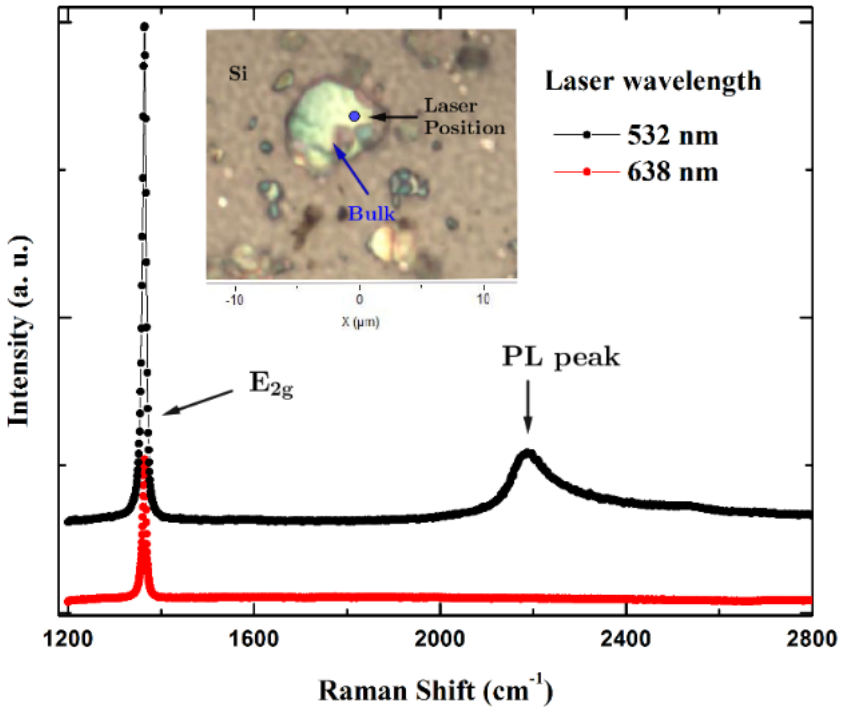

Figure 4.23: Raman spectra acquired from the same location on the h-BN microflake in the inset figure using excitation wavelength of 532 nm and 638 nm at room temperature..

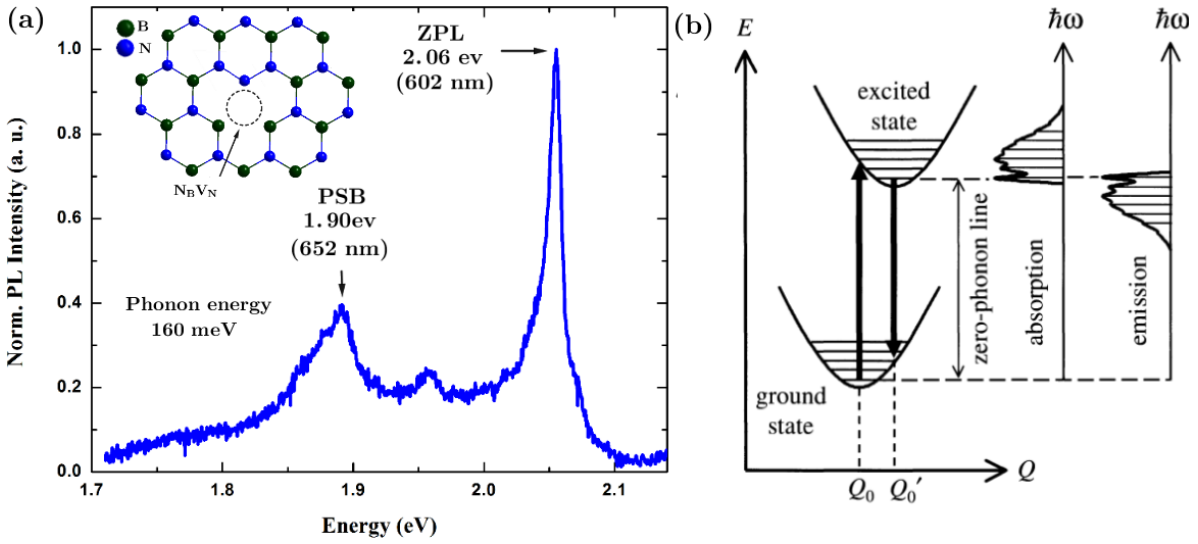

Figure 4.24: (a) PL spectrum of point defects in h-BN microflake. (b) The suppose point defects responsible by the emission. (c) Energy diagram for the ZPL and PSB transitions (Adapted from [45]).

5 Conclusions and perspectives

The samples of WSe_2 prepared by the adhesive tape mechanical exfoliation method present a very low density of monoalyers, being the lateral size of the monolayer obtained of a few of micrometers (<10 μm). The use of SiO_2/Si 300 nm as substrate allows to identify monolayer easily by optical microscopy. A comparison of the AFM and Raman measurements in few-layers and monolayer allow us to confirms the presence of monolayers, obtaining that in few-layer samples the vibrational modes E^1_{2g} and A_{1g} are degenerate and the interlayer B^1_{2g} modes is observed, while in monolayer the degeneracy of the vibrational modes E^1_{2g} and A_{1g} disappear and the Raman peaks corresponding to these modes are separated by 11 cm^{-1}. The optical signature related to A exciton recombination in monolayer was observed at 1.63 and 1.65 eV, these results are in agreement with the reported in the literature. Our PL results showed that light emission in monolayers is twenty times stronger than in few-layer, which is an evidence of the indirect-to-direct band-gap transition from Γ to K point of the Brillouin zone. The B exciton recombination in monolayer also was observed at 2.0 eV. The spin-splitting of the valence band at the K point of the Brillouin zone was determined from the energy difference between A and B excitonic emission as being approximately 370 meV, such is expected in tungsten dichalcogenides compounds. The light emission due to A exciton recombination is a superposition of the emission by trion and neutral exciton recombination. The trion binding energy obtained in this work is $\sim$ 30 meV and the contributions of trions to the total light emission depends on the excitation power and temperature. Therefore, the emission in monolayer at room temperature is dominated by the neutral exciton recombination because the thermal energy, $k_BT \sim 25$ meV, is enough to dissociate the most of trions in excitons. PL measurements at low temperature allow to show the dark exciton character of WSe_2 monolayer, concluding that light emission at room temperature is six times stronger than low temperature. These results make WSe_2 monolayer a great candidate to be used in our first experiments of STML in 2D materials at room temperature. All the optical properties observed here correspond to pristine monolayer. It was not observed any emission related to intrinsic defects in monolayer mechanically exfoliated which means that mechanical exfoliation technique can provide monolayers of high structural quality. It was also found that to create point defects in monolayer by thermal treatment, its recommendable to use a temperature below 500 ^{0}C

to avoid the monolayer evaporation and lost of the sample under investigation. It was possible to obtain images with atomic resolution in some clean and flat region of WSe_2 flakes exfoliated on p-doped silicon substrate, this allowed to obtain the lattice parameter $a = (3.2 \pm 0.1)$AA for the 2D structure of WSe_2. The lattice parameter was obtained determining the interatomic distance between selenium atoms in the top atomic layer of the WSe_2 flake. Some sample cleaning protocols and STM tip treatment are being established to improve our STM measurements and to be able to analyse the structure and electronic properties of pristine monolayer and with point defects to explore the optical properties by STML later.

The morphological and optical properties of WS_2 nanoflakes were investigated by AFM, STM and absorbance spectroscopy. The optical absorption at room temperature associated to the A and B exciton transitions were observed at 2.0 and 2.4 eV, respectively, which gives an spin-splitting of the valence band of about 400 meV. The AFM results showed that the commercial solvent-exfoliated nanoflakes solution of WS_2 is constituted mainly by nanoflakes that are few-layers, and depending on the substrate used it is possible identify monolayers. When the samples were subjected to thermal treatment to clean them and evaporate the solvent of the nanoflakes solution to avoid contaminate the UHV STM chamber or the STM tip, it was observed the formation of some spots as results of the evaporation of the solution where most of the nanoflakes were concentred. This was observed in all the substrate we tried, however it was only possible to perform STM measurements in the sample where p-doped silicon was used as substrate. When topographic STM images were taken in these spots of solution, it was possible to take a STM image of an individual nanoflake whose morphology characteristic are in agreement with sample specifications given by Graphene Laboratory. It was not possible to obtain any STM image with atomic resolution on WS_2 nanoflakes, likely due to contaminations or impurities on the nanoflakes surfaces.

The Raman results obtained in h-BN samples showed that the h-BN flakes in the solution prepared by sonication are bulk microflakes. The light emission related to point defects was observed at room temperature in h-BN microflakes subjected to thermal annealing treatment. The emission spectrum due to point defects in h-BN consist in a narrow emission peak at 2.06 eV associated to zero phonon line transitions and a phonon replica at 1.96 eV, the energy of the phonon involved in the phonon replica transition is approximately 160 meV. Based in results found in the literature, the light emission observed in this work is attributed to point defects of the type N_BN_V.

To continue with the investigation of point defects in 2D materials, the perspectives of this work are to use an alternative exfoliation method to produce pristine monolayers of big size and make possible their study by STM measurements. The idea is to create point defects in a controllable way in these samples and to investigate the structural and electronic properties of point defects by STM images and STS spectroscopy, and additionally acquire the emission spectrum of individual point defects by STML measurements. Based on the results obtained in samples prepared from flakes in solution, we can conclude that these type of samples might not be the appropriated to carry out STM studies due to the low density of monolayer and the formation of spots of solution during the sample cleaning process by thermal treatment in both WS_2 and h-BN samples.

Therefore, such as it was found in this work, the best sample preparation method to produce monolayer of high structural quality is the mechanical exfoliation technique. An alternative is the study of samples grown by chemical vapor deposition but with the inconvenient that these sample typically present a high density of intrinsic defects.

Bibliography

[1] K. S. Novoselov, A. K. Geim, S. V. Morozov, D. Jiang, Y. Zhang, S. V. Dubonos, I. V. Grigorieva, and A. A. Firsov. Electric field effect in atomically thin carbon films. *Science*. **306**, 666-669 (2004).

[2] K. S. Novoselov, and A. K. Geim. The rise of graphene. *Nature*. **6**, 183-191 (2007).

[3] R. R. Nair, P. Blake, A. N. Grigorenko, K. S. Novoselov, T. J. Booth, T. Stauber, N. M. R. Peres, and A. K. Geim. Fine Structure Constant Defines Visual Transparency of Graphene. *Science*. **320**, 1308 (2008).

[4] C. Lee, X. Wei, J. W. Kysar, and J. Hone. Measurement of the Elastic Properties and Intrinsic Strength of Monolayer Graphene. *Science*. **321**, 385-388 (2008).

[5] M. Xu, T. Liang, M. Shi, and H. Chen. Graphene-Like Two-Dimensional Materials. *Chem. Rev.* **113(5)**, 3766-3798 (2013).

[6] M. Chhowalla, H. Suk Shin, G. Eda, L. Jong Li, K. Ping Loh, and H. Zhang. The chemistry of two-dimensional layered transition metal dichalcogenide nanosheets. *Nat. Chem.* **5**, 263-275 (2013).

[7] M. Bernardi, C. Ataca, M. Palummo, and J. C. Grossman. Optical and Electronic Properties of Two-Dimensional Layered Materials. *Nanophotonics*. **2**, 479-493 (2017).

[8] K. F. Mak, C. Lee, J. Hone, J. Shan, and T. F. Heinz. Atomically Thin MoS_2: A New Direct-Gap Semiconductor. *Phys. Rev. Lett.* **105**, 136805-1 (2010).

[9] F. Xia, H. Wang, D. Xiao, M. Dubey, and A. Ramasubramaniam. Two-dimensional material nanophotonics. *Nat. Photonics*. **8**, 899-907 (2014).

[10] W. Choi, N. Choudhary, G. Hee Han, J. Park, D. Akinwande, Y. Hee Lee. Recent development of two-dimensional transition metal dichalcogenides and their applications. *materialstoday.* **20**, 116-130 (2017).

[11] Thesis: Romain Bourrellier. *Luminescence at Defects in h - B N : Excitons at Stacking Faults and Single Photon Emitters*. Université PARIS-SUD (2014).

[12] M. Samadi, N. Sarikhani, M. Zirak, H. Zhang, H. Zhang,and A. Z. Moshfegh. Group 6 transition metal dichalcogenide nanomaterials: synthesis, applications and future perspectives. *Nanoscale Horiz.* **3**, 90-204 (2018).

[13] T. T. Tran, K. Bray, M. J. Ford, M. Toth, and I. Aharonovich. Quantum emission from hexagonal boron nitride monolayers. Nat. Nanotech. **11**, 37-41 (2016).

[14] S. Choi, T. T. Tran, C. Elbadawi, C. Lobo, X.Wang, S. Juodkazis, G. Seniutinas, M. Toth, and I. Aharonovich. Engineering and Localization of Quantum Emitters in Large Hexagonal Boron Nitride Layers. *ACS Appl. Mater. Interfaces.* **8 (43)**, 29642-29648 (2016).

[15] L. Schué, I. Stenger, F. Fossard, A. Loiseau, and J. Barjon. Characterization methods dedicated to nanometer-thick hBN layers. *2D Mater.* **4**, 015028 (2016).

[16] J. Hong, C. Jin, J. Yuan, and Z. Zhang. Atomic Defects in Two-Dimensional Materials: From Single-Atom Spectroscopy to Functionalities in Opto-/Electronics, Nanomagnetism, and Catalysis. *Adv. Mater.* **29**, 1606434 (2017).

[17] P. Vancsó, G. Zsolt Magda, J. Pető, J. Y. Noh, Y. S. Kim, C. Hwang, L. P. Biró, and L. Tapasztó. The intrinsic defect structure of exfoliated MoS_2 single layers revealed by Scanning Tunneling Microscopy. *Sci. Rep.* **6**, 29726 (2016).

[18] M. Kociak, and L.F.Zagonel. Cathodoluminescence in the scanning transmission electron microscope. *Ultramicroscopy.* **176**, 112-131 (2017).

[19] K. Kuhnke, C. Große, P. Merino, and K. Kern. Atomic-Scale Imaging and Spectroscopy of Electroluminescence at Molecular Interfaces. *Chem. Rev.* **117 (7)**, 5174-5222 (2017).

[20] J. A. Wilson, and A. D. Yoffe. The transition metal dichalcogenides discussion and interpretation of the observed optical, electrical and structural properties. *Adv. Phys.* **18**, 193-335 (1969).

[21] H. Katzke, P. Tolédano, and W. Depmeier. Phase transitions between polytypes and intralayer superstructures in transition metal dichalcogenides. *Phys. Rev. B.* **69**, 134111 (2004).

[22] P. A. Young. Lattice parameter measurements on molybdenum disulphide. *J. Phys. D.* **2**, 936-939 (1968).

[23] W. J. Schutte, J. L. De Boer, and F. Jellinek. Crystal structures of tungsten disulfide and diselenide. *J. Solid State Chem.* **70**, 207-209 (1987).

[24] http://www.crystalimpact.com/diamond/ (2017, November 16).

[25] E. K. Sichel, R. E. Miller, M. S. Abrahams, and C. J. Buiocchi. Heat capacity and thermal conductivity of hexagonal pyrolytic boron nitride. *Phys. Rev. B.* **13**, 4607 (1976).

[26] V.L. Solozhenko, A.G. Lazarenko, J.-P. Petitet, and A.V. Kanaev. Bandgap energy of graphite-like hexagonal boron nitride. *J. Phys. Chem. Solids.* **62**, 1331-1334 (2001).

[27] M. Topsakal, E. Aktürk, and S. Ciraci. First-principles study of two- and one-dimensional honeycomb structures of boron nitride. *Phys. Rev. B.* **79**, 115442 (2009).

[28] N. L. McDougall, R. J. Nicholls, J. G. Partridge, and D. G. McCulloch. The near edge structure of hexagonal boron nitride. *Microsc. Microanal.* **20**, 1053-1059 (2014).

[29] K. Kang Kim, A. Hsu, Xiaoting Jia, S. Min Kim, Y. Shi, M. Hofmann, D. Nezich, J. F. Rodriguez-Nieva, M. Dresselhaus, T. Palacios, and J. Kong. Synthesis of Monolayer Hexagonal Boron Nitride on Cu Foil Using Chemical Vapor Deposition. *Nano Lett.* **12**, 161-166 (2012).

[30] G. Kim, A-Rang Jang, H. Young Jeong, Z. Lee, D. Joon Kang, and H. Suk Shin. Growth of High-Crystalline, Single-Layer Hexagonal Boron Nitride on Recyclable Platinum Foil. *Nano. Lett.* **13**, 1834-1839 (2013).

[31] N. W. Ashcroft, and N. Mermin. *Solid State Physics* (Saunders College, Philadelphia, 1976).

[32] J. L. Verble and T. J. Wieting. Lattice Mode Degeneracy in MoS_2 and Other Layer Compounds.*Phys. Rev. Lett.* **25**, 362 (1970).

[33] X. Zhang, X-Fen Qiao, W. Shi, Jiang-Bin Wu, De-Sheng Jiang and Ping-Heng Tan. Phonon and Raman scattering of two-dimensional transition metal dichalcogenides from monolayer, multilayer to bulk material. *Chem. Soc. Rev.* **44**, 2757-2785 (2015).

[34] T. J. Wieting and J. L. Verble. Infrared and Raman Studies of Long-Wavelength Optical Phonons in Hexagonal Mo_2. *Phys. Rev. B.* **3**, 4286 (1971).

[35] W. Zhao, Z. Ghorannevis, K. K. Amara, J. R. Pang, M. Toh, X. Zhang, C. Kloc, P. H. Tane, and G. Eda. Lattice dynamics in mono- and few-layer sheets of WS_2 and WSe_2. *Nanoscale.* **5**, 9677 (2013).

[36] R. Geick, C. H. Perry, and G. Rupprecht. Normal Modes in Hexagonal Boron Nitride. *Phys. Rev.* **146**, 543 (1966).

[37] T. Kuzuba, K. Era, T. Ishii, T.Sato. A low frequency Raman-active vibration of hexagonal boron nitride. *Solid State Commun.* **25**, 863-865 (1978).

[38] I. Stenger, L. Schué, M. Boukhicha, B. Berini, B. Plaçais, A. Loiseau, and J. Barjon. Low frequency Raman spectroscopy of few-atomic-layer thick hBN crystals. *2D Mater.* **4**, 031003 (2017).

[39] R Roldán, J. A. Silva-Guillén, M. P. López-Sancho, F. Guinea, E. Cappelluti, and P. Ordejón. *Ann. Phys. (Berlin).* Electronic properties of single-layer and multilayer transition metal dichalcogenides MX_2 (M = Mo, W and X = S, Se).**9-10**, 347-357 (2014).

[40] G. Liu, W. Shan, Y. Yao, W.Yao, D. Xiao. Three-band tight-binding model for monolayers of group-VIB transition metal dichalcogenides. *Phys. Rev. B.* **88**, 085433 (2013).

[41] W. Zhao, R. Mendes Ribeiro, and G. Eda. Electronic Structure and Optical Signatures of Semiconducting Transition Metal Dichalcogenide Nanosheets. *Acc. Chem. Ress.* **48 (1)**, 91-99 (2015).

[42] G. Wang, A. Chernikov, M. M. Glazov, T. F. Heinz, X. Marie, T. Amand, and B. Urbaszek. Colloquium: Excitons in atomically thin transition metal dichalcogenides. *Rev. Mod. Phys.* **90**, 021001 (2018).

[43] M. Koperski, M. R. Molas, A. Arora, K. Nogajewski, A. O. Slobodeniuk, C. F. and M. Potemski. Optical properties of atomically thin transition metal dichalcogenides: observations and puzzles. *Nanophotonics.* **6(6)**, 1289–1308 (2017).

[44] P. Y. Yu, and M. Cardona. *Fundamentals of Semiconductors. Physics and Materials Properties* (Springer, Berlin, 2010).

[45] M. Fox. *Optical Properties of Solids* (Oxford University Press, Oxford, 2001).

[46] A. Chernikov, T. C. Berkelbach, H. M. Hill, A. Rigosi, Y. Li, O. B. Aslan, D. R. Reichman, M. S. Hybertsen, and T. F. Heinz. Exciton Binding Energy and Nonhydrogenic Rydberg Series in Monolayer WS_2. *Phys. Rev. Lett.* **113**, 076802 (2014).

[47] T. C. Berkelbach, M. S. Hybertsen, and D. R. Reichman. Theory of neutral and charged excitons in monolayer transition metal dichalcogenides. *Phys. Rev. B.* **88**, 045318 (2013).

[48] J. S. Ross, S. Wu, H. Yu, N. J. Ghimire, A. M. Jones, G. Aivazian, J. Yan, D. G. Mandrus, D. Xiao, W. Yao, and X. Xu. Electrical control of neutral and charged excitons in a monolayer semiconductor. *Nat. Commun.* **4**, 1474(2013).

[49] J. W. Christopher, B. B. Goldberg, and A. K. Swan. Long tailed trions in monolayer MoS_2: Temperature dependent asymmetry and resulting red-shift of trion photoluminescence spectra. *Sci. Rep.* **7**, 14062 (2017).

[50] K. P. Dhakal, D. Loc Duong, J. Lee, H. Nam, M. Kim, M. Kan, Y. Hee Lee, and J. Kim. Confocal absorption spectral imaging of MoS_2: optical transitions depending on the atomic thickness of intrinsic and chemically doped MoS_2. *Nanoscale.* **6**, 13028-13035 (2014).

[51] J. Hong, Z. Hu, M. Probert, K. Li, D. Lv, X. Yang, L. Gu, N. Mao, Q. Feng, L. Xie, J. Zhang, D. Wu, Z. Zhang, C. Jin, W. Ji, X. Zhang, J. Yuan, and Z. Zhang. Exploring atomic defects in molybdenum disulphide monolayers. *Nat. Commun.* **6**, 6293 (2015).

[52] W. Zhou, X. Zou, S. Najmaei, Z. Liu, Y. Shi, J. Kong, J. Lou, P. M. Ajayan, B. I. Yakobson, and J. Carlos Idrobo. Intrinsic Structural Defects in Monolayer Molybdenum Disulfide. *Nano Lett.* **13(6)**, 2615–2622 (2013).

[53] S. Tongay, J. Suh, C. Ataca, W. Fan, A. Luce, J. Seuk Kang, J. Liu, C. Ko, R. Raghunathanan, J. Zhou, F. Ogletree, J. Li, J. C. Grossman, and J. Wu. Defects activated photoluminescence in two-dimensional semiconductors: interplay between bound, charged, and free excitons. *Sci. Rep.* **3**, 2657 (2013).

[54] H. Nan, Z. Wang, W. Wang, Z. Liang, Y. Lu, Q. Chen, D. He, P.g Tan, F. Miao, X. Wang, J. Wang, and Z. Ni. Strong Photoluminescence Enhancement of MoS_2 through Defect Engineering and Oxygen Bonding. *ACS Nano.* **8(6)**, 5738-5745 (2014).

[55] P. K. Chow, R. B. Jacobs-Gedrim, J. Gao, T. Ming Lu, B. Yu, H. Terrones, and N. Koratkar. Defect-induced photoluminescence in monolayer semiconducting transition metal dichalcogenides. *ACS Nano.* **9(2)**, 1520-1527 (2015).

[56] H. Pekka Komsa, J. Kotakoski, S. Kurasch, O. Lehtinen, U. Kaiser, and A. V. Krasheninnikov. Two-Dimensional Transition Metal Dichalcogenides under Electron Irradiation: Defect Production and Doping. *Phys. Rev. Lett.* **109**, 035503 (2012).

[57] Z. Lin, B. R. Carvalho, E. Kahn, R. Lv, R. Rao, H. Terrones, and M. A. Pimenta, and M. Terrones. Defect engineering of two-dimensional transition metal dichalcogenides. *2D Mater.* **3**, 022002 (2016).

[58] K. Fai Mak, K. He, C. Lee, G. Hyoung Lee, J. Hone, T. F. Heinz, and J. Shan. Tightly bound trions in monolayer MoS_2. *Nat. Mater.* **12**, 207-–211 (2013).

[59] X. Wei, Z. Yu, F. Hu, Y. Cheng, L. Yu, X. Wang, M. Xiao, J. Wang, X. Wang, and Y. Shi. Mo-O bond doping and related-defect assisted enhancement of photoluminescence in monolayer MoS_2. *AIP Adv.* **4**, 123004 (2014).

[60] A. T. Neal, R. Pachter, and S. Mou. P-type conduction in two-dimensional MoS_2 via oxygen incorporation. *Appl. Phys. Lett.* **110**, 193103 (2017).

[61] R. Jye Shiue, D. K. Efetov, G. Grosso, C. Peng, K. Chung Fong, and D. Englund. Active 2D materials for on-chip nanophotonics and quantum optics. *Nanophotonics.* **6**, 1329-1342 (2017).

[62] Z. Wu, and Z. Ni. Spectroscopic investigation of defects in two-dimensional materials. *Nanophotonics.* **6**, 1219–1237 (2017).

[63] A. Srivastava, M. Sidler, A. V. Allain, D. S. Lembke, A. Kis, and A. Imamoğlu. Optically active quantum dots in monolayer WSe_2. *Nat Nanotechnol.* **10**, 491–496 (2015).

[64] Y. Ming He, G. Clark, J. R. Schaibley, Y. He, M. Cheng Chen, Y. Jia Wei, X. Ding, Q. Zhang, W. Yao, X. Xu, C. Yang Lu, and J. Wei Pan. Single quantum emitters in monolayer semiconductors. *Nat Nanotechnol.* **10**, 497-502 (2015).

[65] I. Aharonovich, D. Englund, and M. Toth. Solid-state single-photon emitters. *Nat. Photonics.* **10**, 631–641 (2016).

[66] P. Tonndorf, R. Schmidt, R. Schneider, J. Kern, M. Buscema, G. A. Steele, A. Castellanos-Gomez, H. S. J. van der Zant, S. Michaelis de Vasconcellos, and R. Bratschitsch. Single-photon emission from localized excitons in an atomically thin semiconductor. *Optica.* **2**, 347-352 (2015).

[67] H Henck, D. Pierucci, G. Fugallo, J. Avila, G. Cassabois, Y. J. Dappe, M. G. Silly, C. Chen, B. Gil, M. Gatti, F. Sottile, F. Sirotti, M. C. Asensio, and A. Ouerghi.

Direct observation of the band structure in bulk hexagonal boron nitride. *Phys. Rev. B.* **95**, 085410 (2017).

[68] G. Cassabois, P. Valvin, and B. Gil. Hexagonal boron nitride is an indirect bandgap semiconductor. *Nat. Photonics.* **10**, 262–266 (2016).

[69] K. Watanabe, T. Taniguchi, and H. Kanda. Direct-bandgap properties and evidence for ultraviolet lasing of hexagonal boron nitride single crystal. *Nat. Mater.* **3**, 404–409 (2004).

[70] J. Zupan. Energy Bands in Boron Nitride and Graphite. *Phys. Rev. B.* **6**, 2477 (1972).

[71] A. Catellani, M. Posternak, A. Baldereschi, H. J. F. Jansen, and A. J. Freeman. Electronic interlayer states in hexagonal boron nitride. *Phys. Rev. B.* **32**, 6997 (1985).

[72] B. Arnaud, S. Lebe, P. Rabiller, and M. Alouani. Huge Excitonic Effects in Layered Hexagonal Boron Nitride. *Phys. Rev. Lett.* **96**, 026402 (2006).

[73] L.Wirtz, A. Marini, M. Gruning, and A. Rubio. Excitonic effects in optical absorption and electron-energy loss spectra of hexagonal boron nitride. arXiv:cond-mat/0508421 (2005), arXiv: cond-mat/0508421.

[74] R. Roldán, L. Chirolli, E. Prada, J. Angel Silva-Guillén, P. San- Jose, and F. Guinea. Theory of 2D crystals: graphene and beyond. *Chem. Soc. Rev.* **46**, 4387-4399 (2017).

[75] R.Bourrellier, M. Amato, L. Henrique Galvão Tizei, C. Giorgetti, A.Gloter, M. I. Heggie, K. March, O. Stéphan, L. Reining, M. Kociak, and A. Zobelli. Nanometric Resolved Luminescence in h-BN Flakes: Excitons and Stacking Order. *ACS Photonics.* **1(9)**, 857–862 (2017).

[76] R. Bourrellier, M. Amato, L. Henrique Galvão Tizei, C. Giorgetti, A.Gloter, M. I. Heggie, K. March, O. Stéphan, L. Reining, M. Kociak, A. Zobelli. Excitons and stacking order in h-BN. arXiv:cond-mat/1401.1948 (2014), arXiv: cond-mat/1401.1948.

[77] Jörg Wrachtrup. Single photons at room temperature. *Nat. Nanotech.* **11**, 7–8 (2016).

[78] T. T. Tran, C. Zachreson, A. M. Berhane, K. Bray, R. G. Sandstrom, L. H. Li, T. Taniguchi, K. Watanabe, I. Aharonovich, and M. Toth. Quantum Emission from Defects in Single-Crystalline Hexagonal Boron Nitride. *Phys. Rev. Appliedl.* **5**, 034005 (2016).

[79] T. T. Tran, C. Elbadawi, D. Totonjian, C. J. Lobo, G. Grosso, H. Moon, D. R. Englund, M. J. Ford, I. Aharonovich, and M. Toth. Robust Multicolor Single Photon Emission from Point Defects in Hexagonal Boron Nitride *ACS Nano.* 10**(8)**, 7331–7338 (2016).

[80] Z. Q. Xu, C. Elbadawi, T. T. Tran, M. Kianinia, X. Li, D. Liu, T. B. Hoffman, M. Nguyen, S. Kim, J. H. Edgar, X. Wu, L. Song, S. Ali, M. Ford, M. Toth, and I. Aharonovich. Single photon emission from plasma treated 2D hexagonal boron nitride. *Nanoscale.* **10**, 7957-7965 (2018).

[81] G. Binnig, and H. Rohrer. Scanning tunneling microscopy. *Helv. Phys. Acta.* **55**, 726-735 (1982).

[82] B. Voigtländer. *Scanning Probe Microscopy: Atomic Force Microscopy and Scanning Tunneling Microscopy* (Springer, Berlin, 2015).

[83] O. Fischer, M. Kugler, I. Maggio-Aprile, and C. Berthod. Scanning tunneling spectroscopy of high-temperature superconductors. *Rev. Mod. Phys.* **79**, 353 (2007).

[84] J. Bardeen. Tunnelling from a Many-Particle Point of View. *Phys. Rev. Lett.* **6**, 57 (1960).

[85] C. J. Chen. *Introduction to Scanning Tunneling Microscopy* (Oxford University Press, Oxford, 2008).

[86] J. Tersoff, and D. R. Hamann. Theory of the scanning tunneling microscope. *Phys. Rev. B.* **31**, 805 (1985).

[87] H. Prüser. *Scanning Tunneling Spectroscopy of Magnetic Bulk Impurities* (Springer, Switzerland, 2015).

[88] R. J. Harners. Atomic-resolution surface spectroscopy with the scanning tunneling microscope.*Annu. Rev. Phys. Chern.* **40**, 531-559 (1989).

[89] C. Chen. Effects of m≠0 tip states in scanning tunneling microscopy: The explanations of corrugation reversa. *Phys. Rev. Lett.* **69**, 1656 (1992).

[90] A. Della Pia, and G. Costantini. *Encyclopedia of Nanotechnology, B. Bharat ed., Springer, New York.* 2301 (2012).

[91] A. L. Vázquez de Parga, and R. Miranda. *Encyclopedia of Nanotechnology, B. Bharat ed., Springer, New York.* 2313 (2012).

[92] H. Amick, M. Gendreau, and C. G. Gordon. *Facility Vibration Issues for Nanotechnology Research.* Presented at Symposium on Nano Device Technology, (2002).

[93] G. Binnig, C. F. Quate, and Ch. Gerber. Atomic Force Microscope.*Phys. Rev. Lett.* **56**, 930 (1986).

[94] Atomic force microscopy: https://pharm.virginia.edu/facilities/atomic-force-microscope-afm/ (2017, December 21).

[95] JPK instruments. NanoWizard AFM Handbook, 2012.

[96] Thesis: Theresa Lutz. *Scanning Tunneling Microscopy and Luminescence of Individual Nanostructure*, École Polytechnique Fédérale De Lausanne, (2011).

[97] A. Jorio, R. Saito, G. Dresselhaus, and M. S. Dresselhaus. *Raman Spectroscopy in Graphene Related Systems* (WILEY-VCHVerlag GmbH & Co. KGaA, Weinheim, 2011).

[98] D. A. Longn. *The Raman Effect. A Unified Treatment of the Theory of Raman Scattering by Molecules* (John Wiley & Sons Ltd, England, 2002).

[99] Dissertation: Vladimir R. Miranda La Hera. *Optical properties of wurtzite phase InAsP/InP heterostructure nanowires*. University of Campinas (2015).

[100] A. Patanè, and N. Balkan. *Semiconductor Research. Experimental Techniques* (Springer, Berlin, 2012).

[101] J.K. Gimzewski, B. Reihl, J.H. Coombs, and R.R. Schlittler. Photon emission with the scanning tunneling microscope. *Z. Phys. B - Condensed Matte.* **72**, 497–501 (1988).

[102] A. Gustafsson, M. E. Pistol, L. Montelius, and L. Samuelson. Local probe techniques for luminescence studies of low-dimensional semiconductor structures. *J. Appl. Phys.* **84**, 1715-1775 (1998).

[103] T. Tsuruoka, Y. Ohizumi, R. Tanimoto, and S. Ushioda. Light emission spectra of individual GaAs quantum wells induced by scanning tunneling microscope. *Appl. Phys. Lett.* **75**, 2289-2291 (1999).

[104] X. H. Qiu, G. V. Nazin, and W. Ho. Vibrationally Resolved Fluorescence Excited with Submolecular Precision. *Science.* **299**, 542-546 (2003).

[105] R. Berndt, J. K. Gimzewski, and P. Johansson. Inelastic tunneling excitation of tip-induced plasmon modes on noble-metal surfaces. *Phys. Rev. Lett.* **67**, 3796 (1991).

[106] N. Nilius, N. Ernst, and H.-J. Freund. Photon Emission Spectroscopy of Individual Oxide-Supported Silver Clusters in a Scanning Tunneling Microscope. *Phys. Rev. Lett.* **84**, 3994 (2000).

[107] M. Sakurai, C. Thirstrup, and M. Aono. New aspects of light emission from STM. *Appl. Phys. A.* **80**, 1153–1160 (2005).

[108] F. Rossel, M. Pivetta, and W. D. Schneider. Luminescence experiments on supported molecules with the scanning tunneling microscope. *Appl. Surf. Rep.* **65**, 129-144 (2010).

[109] M. Kociak, L. F. Zagonel, M. Tencé, and S. Mazzucco. WIPO Patent 2011/148072, (2011).

[110] M. Kociak, L. F. Zagonel, M. Tencé, and S. Mazzucco. WIPO Patent 2011/148073, (2011).

[111] Thesis: L. R. Sheng. *2D TMDs Materials: Atomic structures and Electronic Properties*, National University of Singapore (2014).

[112] D. Necas, and P. Klapetek. Gwyddion: an open-source software for SPM data analysi.*Cent. Eur. J. Phys.* **10(1)**, 181-188 (2012).

[113] B. Liu, M. Fathi, L. Chen, A. Abbas, Y. Ma, and C. Zhou. Chemical Vapor Deposition Growth of Monolayer WSe_2 with Tunable Device Characteristics and Growth Mechanism Study.*ACS Nano.* **9(6)**, 6119–6127 (2015).

[114] Y. Lu, Xiao-Li Li, X. Zhang, Jiang-Bin Wu, Ping-Heng Tan. Optical contrast determination of the thickness of SiO2 film on Si substrate partially covered by two-dimensional crystal flakes.*Sci. Bull.* **60(8)**, 806–811 (2015).

[115] E. del Corro, H. Terrones, A. Elias, C. Fantini, S. Feng, M. An Nguyen, T. E. Mallouk, M. Terrones, and M. A. Pimenta. Excited Excitonic States in 1L, 2L, 3L, and Bulk WSe_2 Observed by Resonant Raman Spectroscopy. *ACS Nano.* **8(9)**, 9629–9635 (2014).

[116] M. Kadleiíková, J. Breza, and M. Veselý. Raman spectra of synthetic sapphire. *Microelectron. J.* **32**, 955-958 (2001).

[117] T. Yan, X. Qiao, X. Liu, P. Tan, and X. Zhang. Photoluminescence properties and exciton dynamics in monolayer WSe_2. *Appl. Phys. Lett.* **105**, 101901 (2014).

[118] W. Zhao, Z. Ghorannevis, L. Chu, M. Toh, C. Kloc, Ping-Heng Tan, and G. Eda. Evolution of electronic structure in atomically thin sheets of WS_2 and WSe_2.. *ACS Nano.* **7(1)**, 791-797 (2013).

[119] H. Zeng, G. B. Liu, J. Dai, Y. Yan, B. Zhu, R. He, L. Xie, S. Xu, X. Chen, W. Yao, and X. Cui. Optical signature of symmetry variations and spin-valley coupling in atomically thin tungsten dichalcogenides.. *Sci. Rep.* **3**, 1608 (2013)

[120] I. Horcas, R. Fernández, J. M. Gómez-Rodríguez, J. Colchero, J. Gómez-Herrerom, A. M. Baro. WSXM: A software for scanning probe microscopy and a tool for nanotechnology.*Rev. Sci. Instrum.* **68**, 013705 (2007).

[121] J. H. Park, S. Vishwanath, X. Liu, H. Zhou, S. M. Eichfeld, S. K. Fullerton-Shirey, J. A. Robinson, R. M. Feenstra, J. Furdyna, D. Jena, H. G. Xing, and A. C. Kummel. Scanning Tunneling Microscopy and Spectroscopy of Air Exposure Effects on Molecular Beam Epitaxy Grown WSe_2 Monolayers and Bilayers.*ACS Nano.* **10(4)**, 4258–426 (2016).

[122] Measuring Vibration: https://www.bksv.com/media/doc/br0094.pdf. (2017, July 18).

[123] H. Amick. *Appl. Phys. Journal of the Inst. of Environmental Sciences.* **5**, 35 (1997)

[124] Vibration criteria for facilities with sensitive equipment: https://www.crystalinstruments.com/vibration-criteria-for-facilities-with-sensitive-equipment/ (2017, July 18).

[125] Fabrication of oxide layers: https://www.halbleiter.org/en/oxidation/oxidation/ (2017, December 12).

[126] S. K. Ghandhi. *VLSI Fabrications Principles. Silicona and Galium Arsenide* (John Wiley & Sons, New York, 1994).

[127] Thesis: Stefan Ernst. *Optimisation of the preparation process for tips used in scanning tunneling microscopy.* Technische Universität Dresden (2006).

Appendices

A

STM room specifications

It is known that the high spatial resolution in STM allows to obtain images with atomic resolution. For this, the tip-sample distance must be maintained as rigid as possible to do not crash the tip on the sample and do not introduce mechanical noise in the measurements. Although the STM junction is mechanically isolated by a system of spring with high frequency of resonance, the mechanical vibration of the floor in the STM room can affect the STM measurements. Hence, the mechanical vibration in our laboratory (laboratory number 21 of the applied physics department, DFA) was analyzed and compared with the standard vibration criteria for laboratory for nanotechnology to know if our laboratory meets with the appropriated vibration requirements to host the scanning tunneling microscope.

The severity of the mechanical vibrations is described by their amplitude. The value of the RMS (room-mean square) velocity amplitude is the best parameter that can be used to measured the amplitude of a vibration because it takes into account the time history of the wave and gives an amplitude that is related with the energy content [122]. In all the vibration standard criteria, the RMS velocity amplitude are processed in one-third-octave bands of frequency [123]. In this way, rather than specifying the vibration levels in fixed bands, proportional bands are used because they provide a more meaningful measure of how a structure reacts to broadband excitation at its resonant frequencies [123, 124]. In table A.1 and figureA.1 are listed and plotted the generic vibration criteria which are divided in four group, according with applications [92]:

- Spaces in which human sensitivity is the only concern—Design the space to meet the "Office" criterion of the International Standards Organization (ISO).
- General laboratories in which low to medium power optical bench microscopes are used—Use vibration criterion VC-A; occasionally VC-B is used to accommodate higher-power bench microscopes.
- Highly-sensitive spaces in which sub-micron processes are carried out—Use criterion VC-D or VC-E (both routinely used worldwide for semiconductor facilities). An alternative is NIST-A (used for "metrology" laboratory space at the Advanced Measurement Laboratory (AML) at the USA's National Institute of Standards and

Technology (NIST) in Gaithersburg, Maryland). NIST-A is more stringent than VC-E at frequencies below 20 Hz.

- Spaces requiring a better environment than can be provided even by a quiet site may have a "better than NIST-A" environment defined by NIST-A1.

Table A.1: Common generic floor vibration criteria (the RMS velocity amplitude as processed in one-third-octave bands of frequency). Adapted from [92].

Category	Criterion	Definition	Space type
Human Sensitivity	ISO Office	400 to 800 μm/s	Research Offices, Computer Modeling
Generic General Lab	VC-A VC-B	50 μm/s, relaxed below 8 Hz 25 μm/s, relaxed below 8 Hz	Optical Microscopes, Epitaxy, CVD
Highly Sensitive	VC-D VC-E NIST-A	6 μm/s 3 μm/s 3 μm/s for $20 \leq f \leq 100$ Hz and below of 3 μm/s for $f < 20$	Nanofabrication Metrology, Surface Characterization, SEM, SPM, AFM
Ultra-Sensitive	NIST-A1	0.75 μm/s for $5 < f \leq 100$ Hz and 0.6 μm/s for $f \leq 5$	Instrument Development

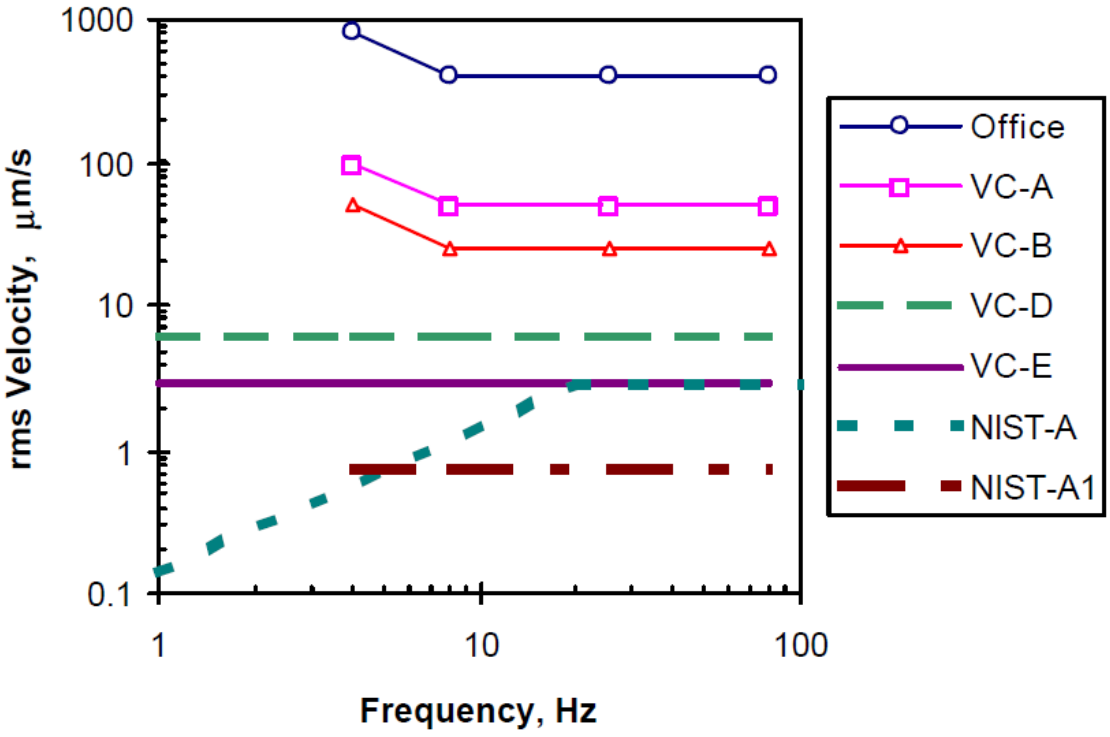

Figure A.1: Generic floor vibration criteria [92].

The mechanical vibrations were measured in several points on the floor of our lab using a piezoelectric accelerometer, which is a sensor that generates an electric output when a force is applied on a piezoelectric element [122]. When the measurements were carried out, all the pumping systems, funs and electrical motors in the neighboring laboratories were turned on. The results are summarise in figure A.2, where the average behavior of

the vibrations is plotted. From this plot, two peaks with frequency at 30 and 60 Hz are observed and these likely come from pumps or fans that are driven by electrical motors with these frequencies. However, it can be seen that the VC-D/E and NIST-A criteria are met, which are the required criteria for laboratories destined to surface characterization and scanning probe microscopy techniques such as is shown in table A.1. Additionally, the acoustic noise of the laboratory was measured using a decibel meter as being of 42 db and the thermal stability is about 1 ^{0}C/h. Based on these results, it was concluded that our laboratory is fully within of the environmental requirement of the RHK company which are shown in figure A.3.

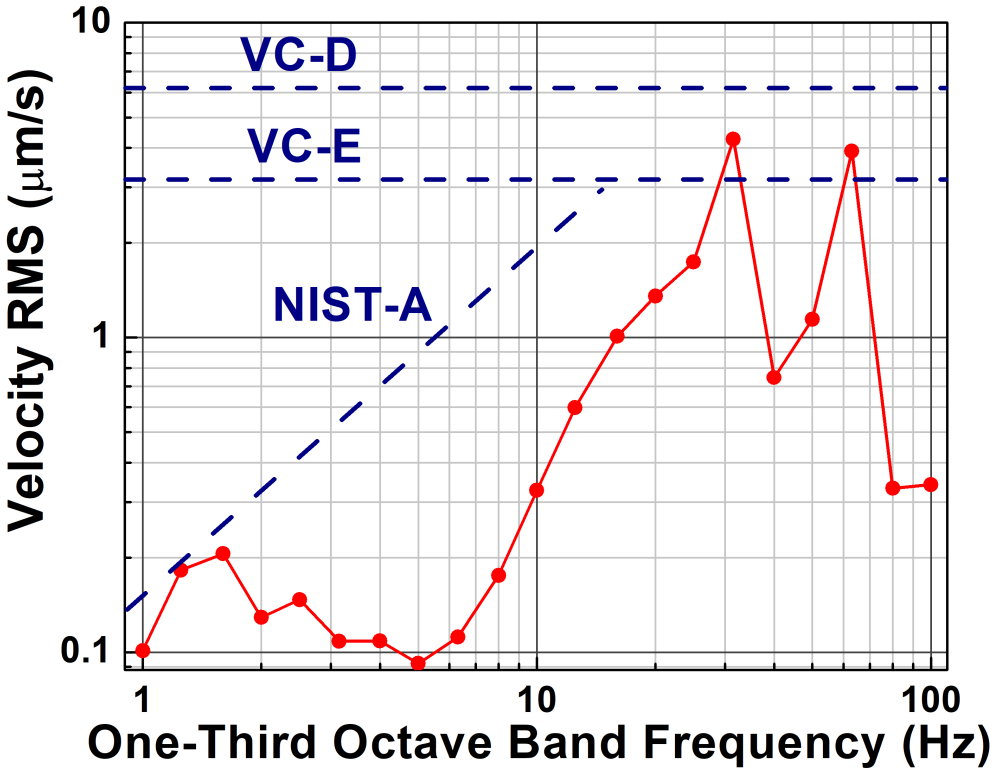

Figure A.2: Floor vibration spectrum of our STM laboratory.

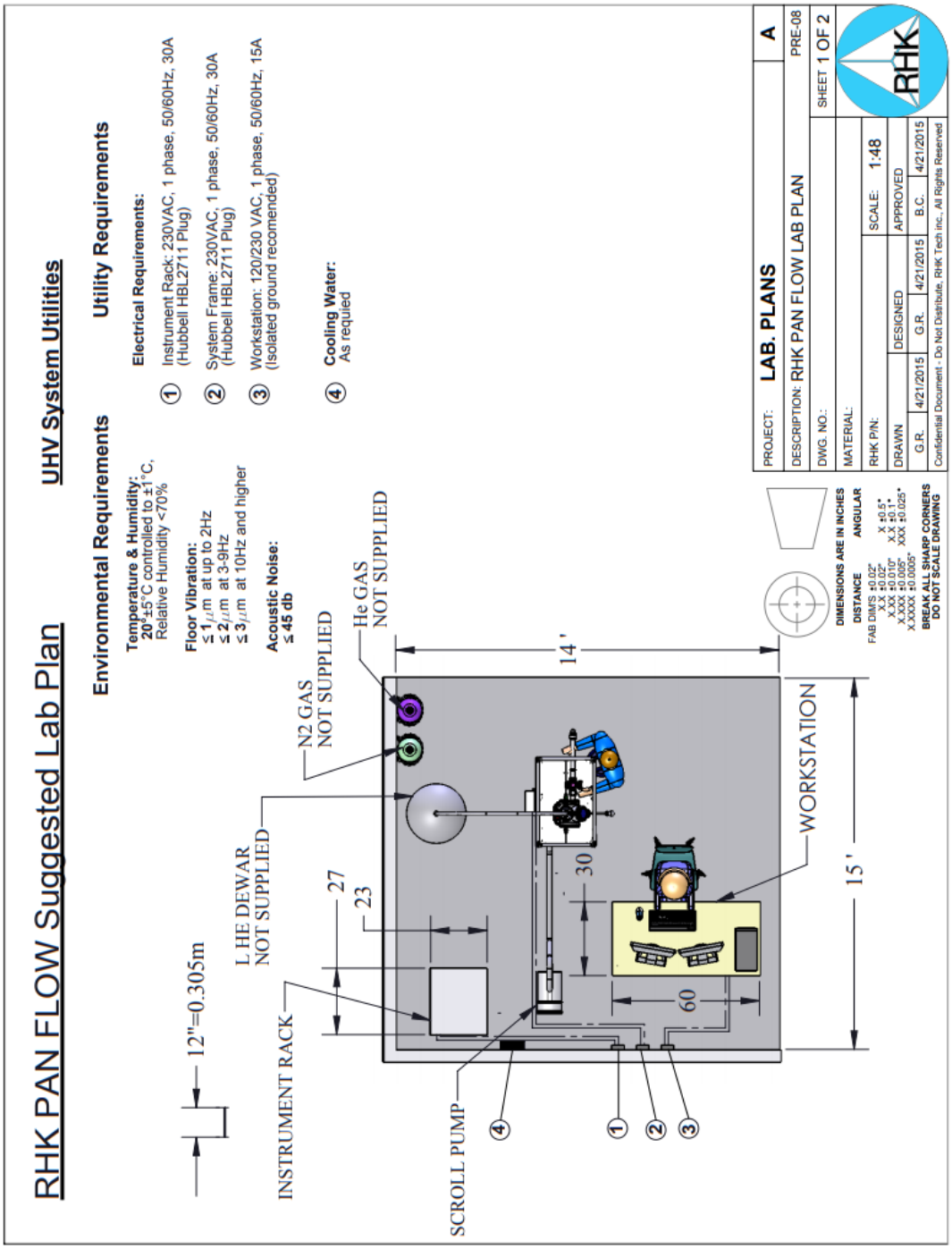

Figure A.3: RHK requirements.

B

Wet oxidation of Silicon

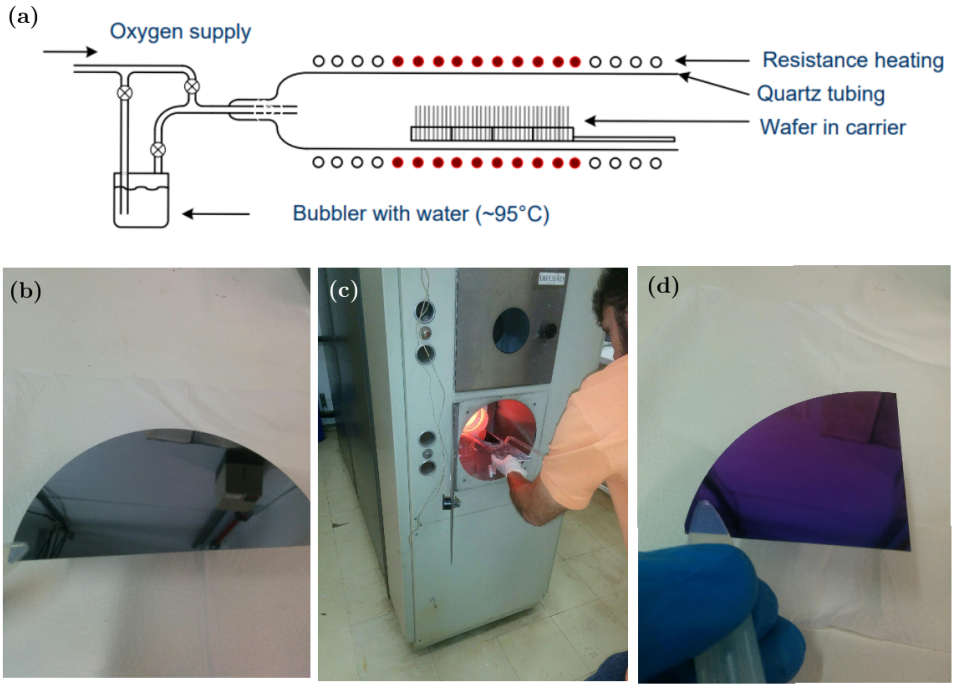

Figure B.1: Wet oxidation of silicon: (a) illustration of the furnace used to carry out the oxidation [125], (b) silicon waver before oxidation, (c) introducing the silicon wafer into the furnace, and (d) silicon wafer after the oxidation process.

In thermal oxidation, silicon wafers are oxidized in a furnace at temperature above 1000 °C. The furnace consists of a quartz tube in which the wafers are placed using a carrier made of guartz glass. The furnace has several heating zones and pipes for chemical gas supply such is shown in figure B.1(a). In the wet oxidation method, the oxygen in gaseous state and as vapor water react with the silicon wafer surface to form silicon dioxide [125]. To obtain silicon dioxide (SiO_2/Si) of 300 nm of thickness, a silicon (100) wafer was placed in the central part of the furnace at 1120 °C for 30 minutes, with 1000 sccm of O_2 and vapor of water, these parameters were chosen based on the plot in figure B.2. From figure B.1(b)-(d) can be seen that once the silicon is oxidized this changeas of color from

black to violet. To determine the thickness of the SiO_2/Si prepared, a height profile was measured using a profilometer. The result is shown in figure B.3 which confirms that SiO_2/Si of about 300 nm has been obtained.

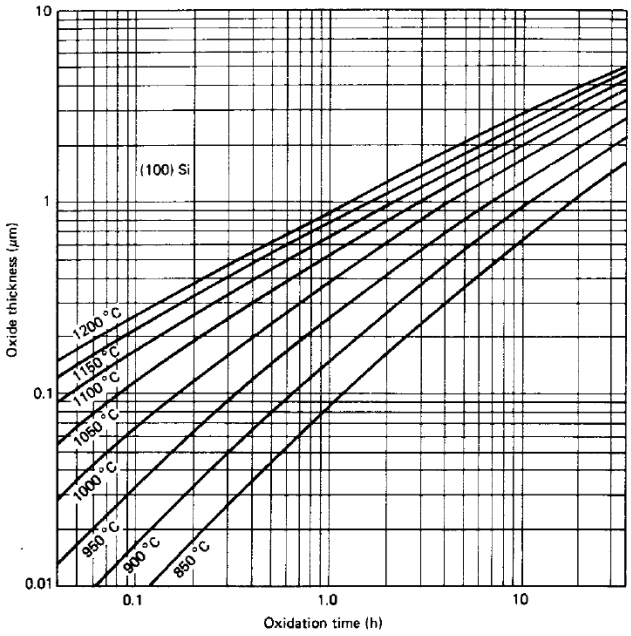

Figure B.2: Oxide growth rate for wet oxidation of silicon (100) [126].

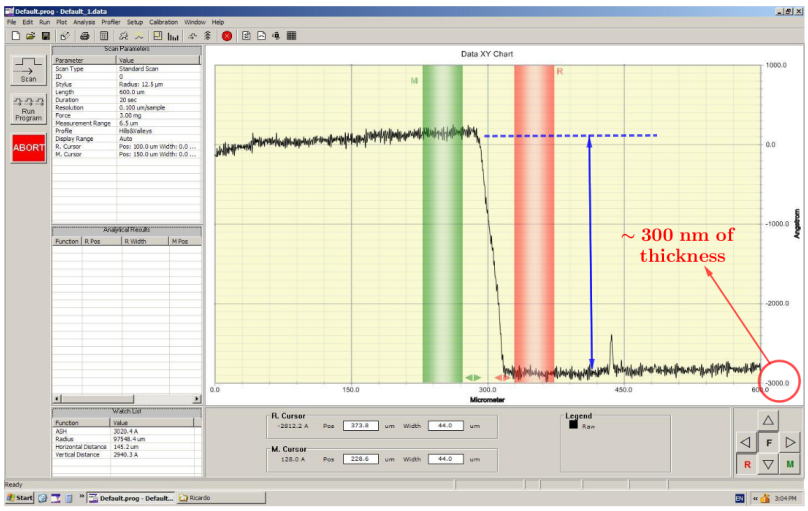

Figure B.3: Hight profile for the SiO_2/Si thickness.

C

STM tips preparation

The STM tip preparation is very important in STM, it's the tip that define the STM resolution and the quality of the STM images. A good STM tip must be sharp enough to achieve the spatial resolution required, mechanically stable and free of contaminations. In this work tungsten tips were prepared by the electrochemical etching method using the preparation system shown in figure C.1. The electrochemical etching method consists in introduce a tungsten wire in NaOH solution (sodium hydroxide). When a bias voltage is applied between the tungsten wire (anode) and a copper cylinder (cathode), the following electrochemical reaction starts [127]:

$$\mathrm{W} + 8\mathrm{OH}^- \rightarrow \mathrm{WO}_4^{2-} + 4\mathrm{H_2O} + 6e^- \ \text{(anode)} \tag{C.1}$$

$$\frac{6\mathrm{H_2O} + 6e^- \rightarrow 3\mathrm{H_2(g)} + 6\mathrm{OH}^- \ \text{(cathode)}}{W + 2\mathrm{OH}^- + 2\mathrm{H_2O} \rightarrow \mathrm{WO}_4^{2-} + 3\mathrm{H_2(g)}} \tag{C.2}$$

The etching process occurs at the wire/soution/air interface, where the wire is oxidized to tungstate anions (WOt_4^{2-}). At the cathode, molecules of water are reduced to hydroxide ions (OH^{2-}) and hydrogen gas ($\mathrm{H_2}$) which is visible during the etching process as gas bubbles. The dissolution of tungsten give rise to the formation of a neck in the wire. When the neck is etched thin enough the wire fractures due to its weight and the tip its ready [82, 127].

Our STM tip preparation process consisted in: i) prepare the NaOH solution dissolving 4 g in 40 ml of deionized water, ii) introduce the copper electrode into the solution until the middle of its height, iii) apply 3 V of bias between the tip and the cooper electrode, and iv) introduce a tungsten wire with 0.25 mm of diameter into the NaOH solution until to measure a current of about 20 mA. When the current drops drastically to zero, the voltage supply is turned off. With these parameter the electrochemical etching process takes around 8 minutes. Following this preparation protocol, STM tungsten tips were prepared systematically.

In figure C.1(a) the etching process is illustrated and a tungsten tip fabricated using our STM tip preparation system is shown in figure C.1(b). The experimental setup is

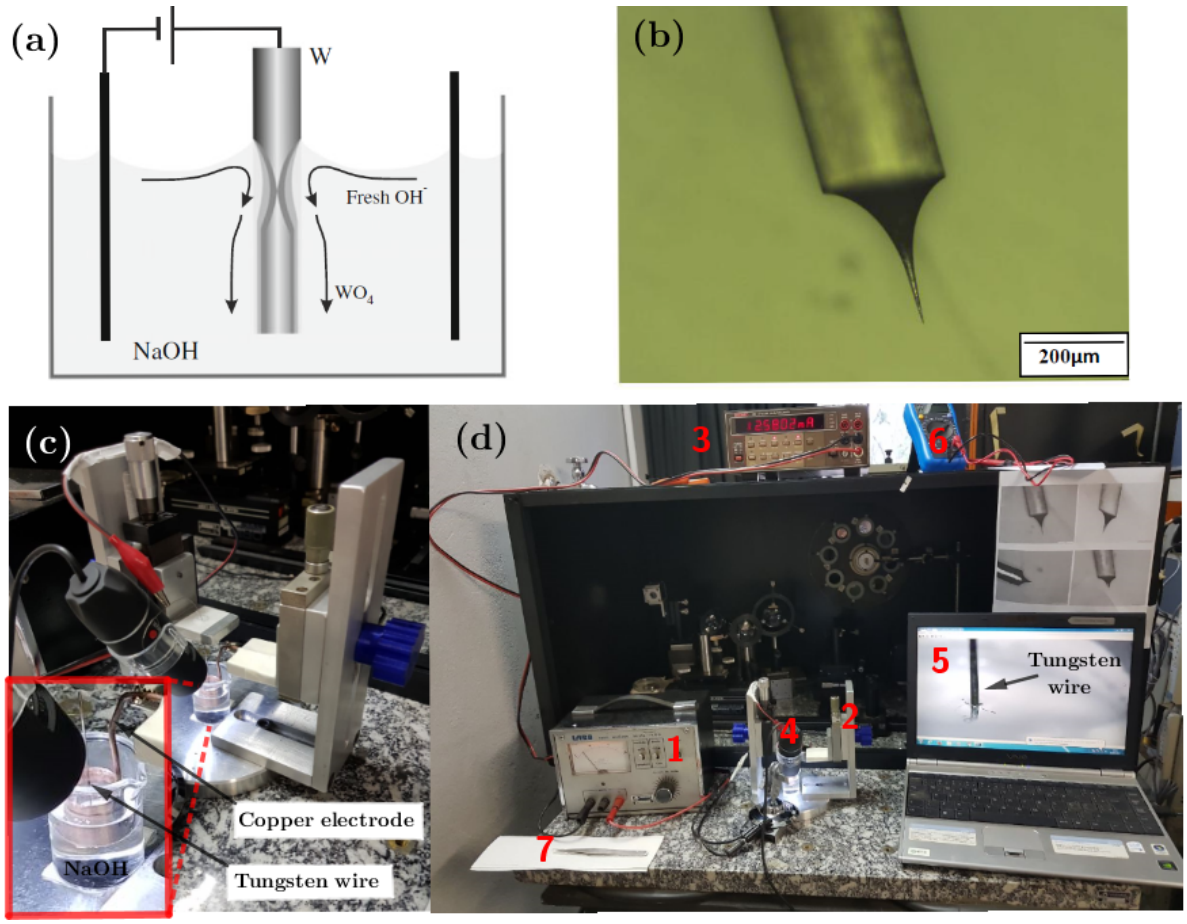

Figure C.1: (a) Etching process. (b) Optical microscope image of tungsten tip. (c) and (d) STM tip preparation setup: (1) voltage supply, (2) etching station, (3) keithley multimeter (4) Webcam (5) notebook (6) multimeter, and (7) tweezers.

described in figure C.1(c) and (d). A DC voltage supply is used to apply a bias between the tungsten wire and the cooper electrode. All the etching process is visualized in the notebook with the help of a webcam. A keithley multimeter is used to measure the electrochemical current and to know when the bias supply must be turned off. At the beginning, the bias supply was turned off manually, but now an electrical circuit has been couple to the STM tip preparation system to do this task automatically. The STM tips were tested in samples as as HOPG and Si(111) and it was possible to obtain images with atomic resolution such as shown in figure C.2. The STM image in HOPG was taken in air and at room temperature, while the image of the Si(111)-7×7 reconstruction was taken in UHV (10^{-10}) torr at 80 K.

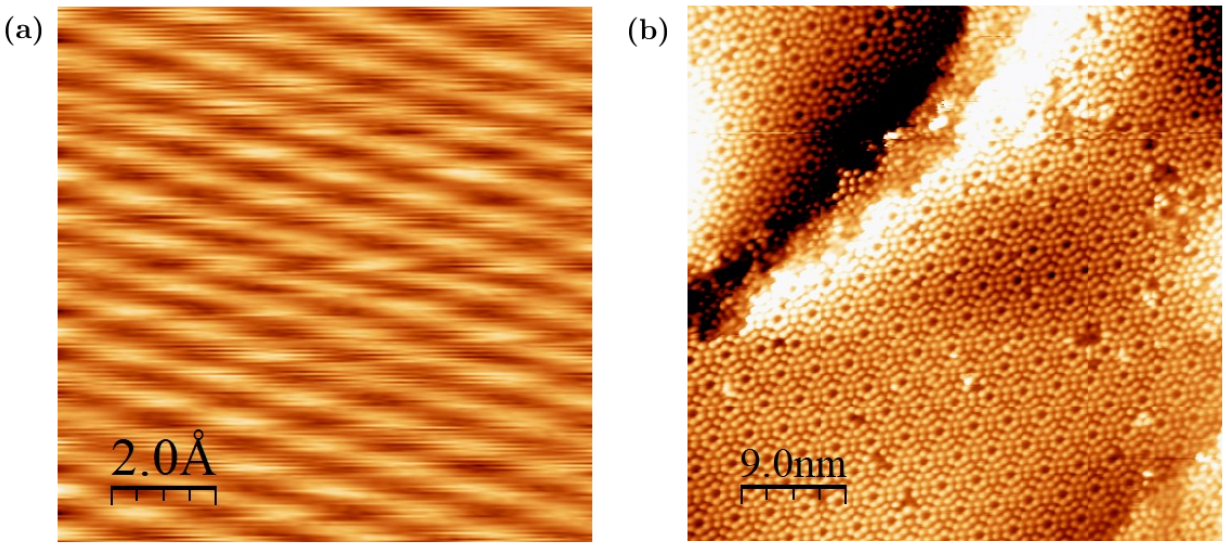

Figure C.2: STM image with atomic resolution. (a) 1.0 nm × 1.0 nm STM image of HOPG (V_B= 100 mV, I_T= 1.0 nA) taken in air at room temperature. (b) 45.0 nm × 45.0 nm STM image in of the Si(111)-7×7 reconstruction (V_B= 1.5 V, I_T= 0.500 nA) taken in UHV at 80 K.